Georg Brunnhofer, MSc

Time and Space Resolved Characterization of Nanoparticles

Dissertation

to achieve the university degree of

Doctor in Technical Science

Doctoral programme: Information and Communications Engineering ICE

submitted to

Graz University of Technology

Supervisor

Univ.-Prof. Mag.rer.nat. Dr.rer.nat. Alexander Bergmann

Institude of Electrical Measurement & Sensor Systems
Head: Univ.-Prof. Mag.rer.nat. Dr.rer.nat. Alexander Bergmann

Graz, September 2020

Für meine Eltern,
die auf ihrem landwirtschaftlichen Betrieb hart arbeiten,
die in mir den Erben des Hofes hofften,
und mich dennoch in meiner akademischen Laufbahn
vollends unterstützten.

Erst diese Doktorarbeit gewährte mir den Einblick,
dass auch mein Vater selbiges vor hatte,
dies jedoch nicht verwirklichen konnte.

Affidavit

I declare that I have authored this thesis independently, that I have not used other than the declared sources/resources, and that I have explicitly indicated all material which has been quoted either literally or by content from the sources used. The text document uploaded to TUGRAZonline is identical to the present doctoral thesis.

_____   _____

Date   Signature

Acknowledgment

My greatest thanks go to Alexander Bergmann, who was a great mentor to me not only during my thesis, but even before that as my supervisor at AVL. Both as my boss and colleague at the time and as a professor, I appreciate his professional competence, leadership and personality. His career change to the university was my initial spark and the decisive factor in starting a PhD thesis. I would also like to thank him for the project and fundraising and all the administrative efforts involved, which enabled me to have a smooth and worry-free research start.

In the course of this my further thanks go to Martin Kraft and Andreas Klug who supervised and guided me at CTR/SAL and AVL. Martin and his team made helpful contributions in CFD- simulations, thermodynamics and optics, and realized various mechanical engineering tasks. I would particularly like to highlight the contribution of Isabella Hinterleitner who developed a machine learning based counting algorithm. Andreas and my colleagues at AVL have been very supportive in mechanical designs and in the selection and implementation of optical components, and have always helped me with physical issues.

I very much appreciated the spirit of research and cheerful atmosphere at the Institute of Electronic Sensor Systems where I had a great time with great PhD fellows and students. All of them are great researchers and will be (in my opinion they already are) highly respected scientists. I had many fruitful, profound and yet amusing discussions. In particular I would like to mention Philip Bergmann and thank him for the collaboration in form of a bachelor thesis.

And last but not least, I am thankful for the good preliminary work of Martin Cresnoverh and Patrick Falk who built the basis of the research topic. Patrick played a special role as he ultimately made me take the opportunity to do the doctorate. And finally, I am thankful for Chris' proofreading.

Abstract

Digital Inline Holography (DIH) is used in many fields of 3-dimensional (3D) imaging to locate micro or nano-particles in a volume, and determine their size, shape or trajectories. For Condensation Particle Counters (CPCs), a holographic based particle counting concept is a novel and valuable approach since multiple micrometer sized particles are detected in a three dimensional sampling volume, all at once. This implies a direct determination of particle number concentrations (number of particles / unit volume $[\#/cm^3]$) and enables additional opportunities for paticle sizing, particle characterization and finally provides quality indicators of the condensation process.

This work describes the realization of a Holographic Particle Counter (HPC). A functional demonstrator of an in-line holographic based counting unit, hereinafter referred to as Particle Imaging Unit (PIU), was developed and implemented in a standard Condensation Particle Counter (CPC). The proposed imaging unit is capable of detecting holograms of particles which sizes are in the lower μm- range. Particles are recognized as interference patterns - so called fringe patterns - and are counted directly at the hologram plane. Therefore, various pattern recognition algorithms based on 2D image processing means were designed and compared in terms of detection performance and processing speed.
A Holographic Aerosol Particle Model (HAPM) was elaborated to establish a common understanding of DIH and support the design of the developed imaging unit and pattern recognition algorithms. The impact of coincidence at higher particle densities is shown and two coincidence correction approaches are presented where, at last, its analogy to the coincidence correction methods used in state-of-the-art CPCs is identified. In conclusion, a ready-to-use demonstrator of a Holographic Particle Counter is presented and benchmarked against a commercial TSI-3775 CPC.

Kurzfassung

Digitale Inline-Holografie (DIH) wird in vielen Bereichen der 3D Bildgebung eingesetzt, um Mikro- oder Nanopartikel in einem Volumen zu lokalisieren und ihre Größe, Form oder Trajektoren zu bestimmen. Für Kondensationspartikelzähler (CPCs) ist ein holografisch basiertes Partikelzählkonzept ein neuartiger und nützlicher Ansatz, da mehrere mikrometergroße Partikel in einem 3D Probenahmevolumen auf einmal detektiert werden. Dies impliziert eine direkte Bestimmung der Partikelanzahlkonzentrationen (Anzahl der Partikel / Einheitsvolumen [$\#/cm^3$]) und ermöglicht zusätzliche Möglichkeiten der Partikelgrößenbestimmung, der Partikelcharakterisierung und liefert letztendlich Qualitätsindikatoren des Kondensationsprozesses.

Diese Arbeit beschreibt die Realisierung eines holografischen Partikelzählers (HPC). Ein Funktionsdemonstrator einer holographisch basierte Zähleinheit, im Folgenden Particle Imaging Unit genannt, wurde entwickelt und in einem Standard CPC implementiert. Die hier vorgeschlagene Bildgebungseinheit ist in der Lage, Hologramme von Partikeln, deren Größe im unteren μm- Bereich liegen, zu erkennen. Partikel werden als Interferenzmuster erkannt - so genannte Fringe Pattern - und werden direkt auf Hologrammebene gezählt. Dafür wurden verschiedene Mustererkennungsalgorithmen auf Basis von 2D-Bildbearbeitung entworfen und bezüglich ihrer Detektionsperformance und Prozessierungszeiten verglichen.

Zur Schaffung eines allgemeinen Verständnisses der DIH und zur Unterstützung des Entwurfs der entwickelten Bildgebungseinheit und der Mustererkennungsalgorithmen wurde ein holografisches Aerosolpartikelmodell (HAPM) ausgearbeitet. Der Einfluss von Koinzidenz bei höheren Teilchendichten wird gezeigt und zwei Koinzidenzkorrekturansätze vorgestellt, wobei ihre Analogie zu den in modernen CPCs verwendeten Koinzidenzkorrekturmethoden schließlich identifiziert wird.

Zusammenfassend wird ein einsatzfähiger Demonstrator eines holografischen Partikelzählers präsentiert und mit einem kommerziellen TSI-3775 CPC verglichen.

Contents

Contents

Contents

List of Acronyms

2D   2-dimensional

3D   3-dimensional

AI   Artificial Intelligence

AoV   Angle of View

APC   AVL Particle Counter

APCs   AVL Particle Counters

APM   Aerosol Particle Model

ASM   Angular Spectrum Method

AWGN   Additive White Gaussian Noise

BMDW   Austrian Federal Ministry of Digital and Economic Affairs

BMK   Austrian Federal Ministry of Climate Action, Environment, Energy, Mobility, Innovation and Technology

CAD   Computer Aided Design

CCD   Charge Coupled Device

CCDs   Charge Coupled Devices

CFD   Computational Fluid Dynamics

CHT   Circular Hough Transform

CMOS   Complementary Metal-Oxide-Semiconductor

CNM   Condensation Nucleus Magnifier

List of Acronyms

CNMs Condensation Nucleus Magnifiers

CPC Condensation Particle Counter

CPCs Condensation Particle Counters

DAQ Data Acquisition

DIH Digital Inline Holography

DCNN Deep Convolutional Neural Networks

DFT Discrete Fourier Transform

DoF Depth of Field

DoF′ Degree of Freedom

DSP Digital Signal Processing

FFG Austrian Research Promotion Agency

FoV Field of View

FZP Fresnel Zone Plate

FZPs Fresnel Zone Plates

GPIO General Purpose Input/Output

GPU Graphics Processing Unit

GUI Graphical User Interface

HAPM Holographic Aerosol Particle Model

HD High Definition

HDR High Dynamic Range

HeNe Helium-Neon

HEPA High Efficiency Particulate Air

HOE Holographic Optical Element

HOEs Holographic Optical Elements

HPC Holographic Particle Counter

HPIV Holographic Particle Image Velocimetry

HT Hough Transform

HT-CPC High Temperature Condensation Particle Counter

Laser Light Amplification by Stimulated Emission of Radiation

LEDs Light Emitting Diodes

LoD Limit of Detection

NaCl Sodium Chloride

MFM Mass Flow Meter

PM2.5 Particulate Matter 2.5

PM10 Particulate Matter 10

PM Particulate Matter

PN Particle Number

OE Optical Element

OEs Optical Elements

OPC Optical Particle Counter

OPCs Optical Particle Counters

PA Pressurized Air

PCB Printed Circuit Board

PCBs Printed Circuit Boards

PIU Particle Imaging Unit

PIUs Particle Imaging Units

PIV Particle Image Velocimetry

R83 Regulation 83

ReLu Rectified Linear Unit

PSF Point Spread Function

List of Acronyms

RoI   Region of Interest

RT   Real Time

SLM   Selective Laser Melting

SMPS   Scanning Mobility Particle Sizer

SNR   Signal to Noise Ratio

SLS   Static Light Scattering

UNECE United Nations Economic Commission for Europe

Nomenclature

Physics Constants

μ	Permeability of a medium	H/m
ε	Permittivity of a medium	F/m
c	Speed of light in vacuum	$299.792.458$ m/s

Wave Optics

$\delta(x,y)$	Delta function
λ	Wavelength of the reference wave
$\mathbf{k_0}; k_0$	Propagation vector ; wave number in free space
$\mathbf{r}; \mathbf{o}$	Complex amplitude of the reference wave ; and the object wave
$\mathbf{R}, \mathbf{a_x}, \mathbf{a_y}, \mathbf{a_z}$	Position vector with components in x, y & z
$\mathbf{r}; \mathbf{v}$	Position vector ; motion vector
$\mathbf{u_0}; \mathbf{u_{+1}}; \mathbf{u_{-1}}$	zeroth-order diffraction ; virtual image ; conjungate image
$\mathcal{H}(k_x, k_y; z)$	Spatial frequency transfer function of propagation through a distance z
ϕ	Phase term of a sine- function
ψ	Electric field distribution, solution to the three dimensional scalar wave equation
$\Psi(x,y)$	Intensity distribution on a recording medium
$\Psi_r; \Psi_{prt}$	Field distribution of the reference ; and the object wave
$\Psi_{prt0}(k_x, k_y)$	Angular plane wave spectrum of the initial field distribution $\psi_{prt0}(x,y)$
$\psi_{prt}; \psi_{prt0}$	Diffracted field distribution after aperture ; and its initial condition
$\Psi_{prt}(k_x, k_y; z)$	Angular plane wave spectrum in a distance z

τ	Recording time or exposure time
θ	Reference beam offset angle
A	Amplitude
d_{prt}	Diameter of particle
f	Focus length of a lense or the FZP
f_{local}	Local fringe frequency
$H(k_x, k_y; z)$	Paraxial approximation of the spatial frequency transfer function $\mathcal{H}(k_x, k_y; z)$
$h(x, y; z)$	Spatial impulse response
$I(\mathbf{r}, t), I(x, y)$	Intensity distribution
$I; I_\tau$	Intensity ; intensity after recording
k_x, k_y	Spatial radian frequencies
k_{0z}	z- component of the propagation vector
$t(x, y)$	Transparency function
$t; t'$	Time ; time when performing superposition
v	Velocity of a wave in a medium
z_{prt}	Distance of particle away from the recording medium

Digital Signal Processing & Pattern Recognition

$\bar{v}_Q$	Average aersosol flow speed
$\bar{x}, \bar{y}$	Circle center
Δd_τ	Elongation of fringe patterns or fringes
Δdr	Interzone distance in a Fresnel Zone Plate
Δr_{res}	Resolution of a Fresnel Zone Plate
Δz_τ	Traveled distance in z- direction during exposure
$\Delta_\tau R$	Displacement due to exposure τ
Δ_x, Δ_y	Sampling period
Δ_{kx}, Δ_{ky}	Discretized sampling period
$\mathcal{R}$	Region
ϕ	Motion direction of a particle
σ_n	Variance of Noise
σ_{lp}	Filter size of a low pass filter
ε	Eccentricity of a region or fringe pattern

φ_{xy}	Phase term of the complex filter operator O_{PCA}
A	Area of a region
$a;b$	Semi-major axis ; and semi-minor axis of an ellipse
D, D_x	Size or extend of a Fresnel Zone Plate or a fringe pattern
d_{pxl}	Pixel size
dr_n	Zone width of the nth zone in a FZP
$F(\cdot); G(\cdot)$	Image to be convolved ; motion-blurred image
f_s	Sampling frequency
f_{sig}	Signal frequency
$g(x,y)$	Transfer function of motion blurring
$g^{TM}(x,y)$	Filter operator based on Template Matching for Blob Detection
$H(\cdot)$	Transfer function of motion-blurring
$H_{drk}, H_{br}; H_{max}$	Entropy of dark and bright pixels in an image ; maximum sum entropy
k,l	Pixel indices in global thresholding
k_{opt}	Index of optimum threshold in global thresholding
L	Number of gray levels
L_1, L_2	Lower and upper limit to confine the optimum threshold in global thresholding
L_x, L_y	Record lenght in spatial directions (x,y)
m	Index or step of the current scanning radius in Blob Detection
M, N	Number of samples
m, n	Indices in spatial domain
$m_{0,0}$	Moment of zeroth order
$m_{1,0}, m_{0,1}$	Moments of first order
$m_{2,0}, m_{1,1}, m_{0,2}$	Moments of second order
M_{min}, N_{min}	Minimum required number of samples
$m_{p,q}$	Mathematical moment with indices of the moment
$n; N$	Actual zone of a Fresnel Zone Plate ; total number of zones
O_{PCA}	Complex filter operator based on Phase Coded Annulus for Hough Transform

p, q	Indices in Fourier domain or mathematical moments
$P_\odot$	Perimeter of a region
P_{drk}, P_{br}	Probability of dark and bright pixels being assigned to its respective class
R_n, R_N	Radius of the nth zone in a FZP or fringe & radius of outer-most zone or fringe
R_{min}, R_{max}	Minimum and maximum radius to search with the Hough Transform (HT)
S_{HT}	Sensitivity parameter of the HT
u	Ratio between the semi-major axis and the semi-minor axis of an ellipse
$u_\odot$	Scaling factor between the fringe pattern's size and any inner fringe
$v_{prt}; v_0$	Instantaneous speed ; relative speed of a particle

Aerosol Physics

δ_d	Diameter of dead area
Ω	Fraction of detector area occupied by coincidence
τ_s	Sampling time interval
$A_d; A_{cam}$	Dead area ; camera area
b	Slope of particle number concentration curve
$C, C_N; C_a$	Particle number concentration ; dead area corrected particle number concentration
d	Particle diameter
d_g	Geometric mean diameter of particle size distribution
d_{50}	50% cutpoint of particle size distribution
f_D	Dead area correction factor
$N; N_\tau$	Particle count ; particle count in a certain interval τ
p_{out}	Output pressure
Q	Flow rate
t_d	Dead time
$V; V_s$	Volume ; sample volume

Dimensions & Parameters related to the Particle Imaging Unit

α	Weight for dynamic background correction
λ	Wavelength of the light source
$\tau; \tau_{cam}; \tau_{on}$	System exposure time ; exposure time of the imager/camera ; flash duration of the light source
f_{mod}	Modulation frequency of the light source
$I; I_0$	Image/frame of actual measurement ; background corrected image/frame
Q_{smpl}	Sampling flow rate
x_{cam}, y_{cam}	(x, y)- dimensions of the imager/camera
x_{ch}, z_{ch}	Width and depth of the sampling channel
z_0	Distance between imager/camera and the inner sampling channel wall

1. Introduction

1.1. Particle Number Detection in Automotive Exhaust

A major topic in aerosol measurement is the detection of aerosol Particle Number (PN). Where Aerosol Electrometers are gaining more and more relevance for measuring high particle number concentrations, Optical Particle Counters (OPCs) still represent the most universal instruments to cope with low particle numbers. OPCs are single-particle detectors and make use of the light scattering properties of particles to optically detect and count them individually. Particles are illuminated by a light source of a certain wavelength and partially absorb and scatter light energy, whereas the scattered fraction of the light is detected by photoelectrical sensors. This process of elastic light scattering depends on the wavelength λ of the incident light and the size d_{prt} of the scattering particle. Scattering is divided into three domains:

Scale	Domain
$d_{prt} \ll \lambda$	Rayleigh scattering
$d_{prt} \approx \lambda$	Mie scattering
$d_{prt} \gg \lambda$	Geometric scattering (classic optics)

The Rayleigh model describes the elastic scattering process when particles are much smaller than the wavelength of the incident light and is valid

to around 10% of the wavelength. In this size regime the exact shape of scattering objects is not significant and can be treated as spherical volumes. Lorenz-Mie theory (Mie, 1908) applies for particles with diameters of the same order as the incident light (roughly $100\,nm$ up to a few μm). The interaction of particles and the incident beam is very strong and more complex. This size domain is described by Mie scattering.
Particles larger than the wavelength of the incident light are subject to the laws of classic geometric optics with reflection, refraction and diffraction. Diffraction arises from rays passing particles and, in the scale of $d_{prt} > 4 - 5\lambda$, Lorenz-Mie theory reduces to Fraunhofer diffraction. "The scattered intensity in this regime is proportional to the particle cross-sectional area and not strongly dependent on shape or composition" (Baron and Willeke, 2005).

OPCs are operated with either broadband (white light) or, most commonly, with monochromatic light sources (typically Lasers). The wavelength of the light is typically in the visible spectrum with $380 - 740\,nm$. The scattered light of sensed particles is in the Mie regime and has a complex dependence on the light source, range of detection angles, particle size, shape and refractive index. As a consequence, it provides a direct measure of PN, particle size distribution and particle shape (Hinds, 2012; Giechaskiel et al., 2014; Kerker, 1997; Baron and Willeke, 2005). "However, the sizing and shape determination capabilities of OPCs are usually only approximate." As the detection sensitivity of light scattered by smaller particles is limited to about $100\,nm$ (Heim et al., 2008), a condensational growth of particles (typically below $d_{prt} = 1\,\mu m$) aids the optical detection. Particles are counted after they are grown to micron size using instruments known as CPCs. These determine particle counting rates as particle number concentration C_N in *number of particles / unit volume = $[\#/cm^3]$*.

1.2. Condensation Particle Counter

As previously mentioned, CPCs comprise two main components: a magnification stage, also referred to as Condensation Nucleus Magnifier (CNM),

and an optical counting unit. Figure 1.1 illustrates the schematic of a typical CPC which will be described in more detail.
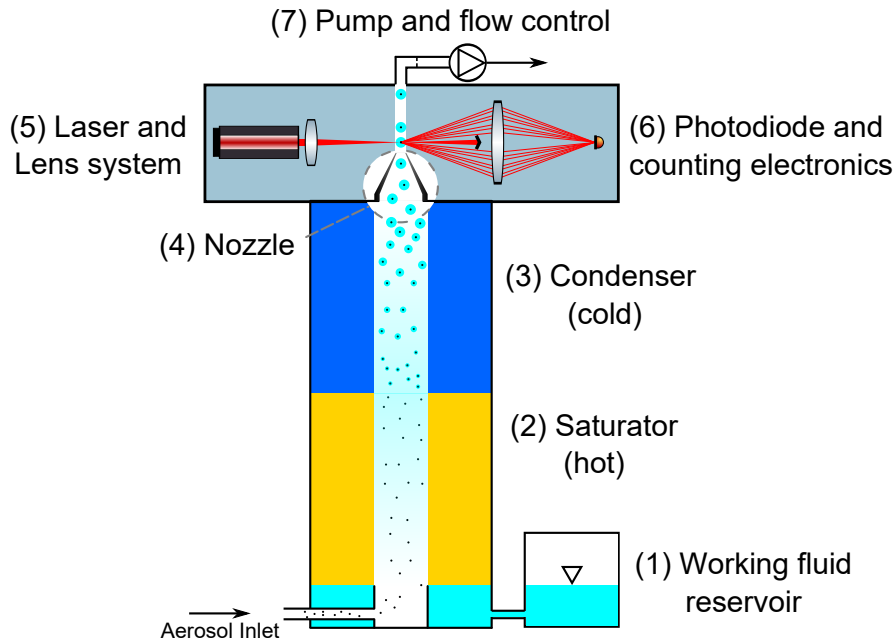
Figure 1.1.: Schematic of a Condensation Particle Counter (Cresnoverh, 2015)

1.2.1. Particle Growth

Particle growth is achieved by passing the aerosol through a saturated vapor of a working fluid (e.g. alcohol, hydrocarbons or water), followed by cooling in a condensing section[1]. The preconditioned aerosol[2] is led into the CNM which consists of a saturator section (2) and a condenser (3). The working fluid from the reservoir (1) is vaporized in the saturation region and mixed with the aerosol through a porous material called wick. The saturator is tempered significantly above the temperature of the condensing region in

---

[1]Water based CPCs follow an inverse principle.

[2]Standard CPCs work approximately at room temperature and hence require similarly conditioned aerosol. Also, gaseous and volatile components are vaporized in advance.

order to allow the obtained supersaturated vapour to condense on the particles in the cooler area of the condenser. Each particle acts as a condensation nucleus and activates the growth of a droplet around it - often referred to as *particle activation*. The minimum size of particles that can be "activated" is defined by the *Kelvin diameter* and is set by the saturation ratio (cf. Baron and Willeke, 2005). The saturation ratio is controlled by the temperature difference between the hot saturator and the cold condenser. A constant temperature difference means that droplet growth starts at a constant particle size. In this way, nanoparticles as small as $1\,nm$ have been reported to be activated and detected with CPCs (Kuang et al., 2012). The duration of particles being exposed to supersaturation conditions determines the end size of the droplet. It depends on the length of the condensing region and the flow speed of the aerosol through it.

> In conclusion, the process of condensation enables reliable magnification of single particles, being "activated" at a well defined minimum particle size and grown to single droplets of constant and controllable size of spherical shape.

1.2.2. Optical Counting Unit

A subsequent optical counting unit is commonly based on nozzle designs (4) to separate the grown droplets. These are sequentually passing a focused light beam (5) where only one particle/droplet is illuminated at a time. A beam stop terminates the direct beam of the light source, including a foreward scattered fraction of light. As indicated in Figure 1.1, the remaining fraction of the scattered light (a limited range of the scattering angle) is collected by a lens and focused onto a photo diode (6). The consecutive scattered light sequence is detected as an ensemble of electrical pulses (as sketched in Figure 1.2) and each pulse is considered a single counting event.

Voltage [V]

Time [ns]
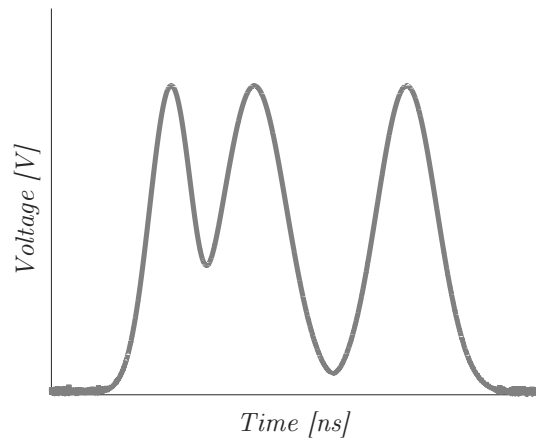
Figure 1.2.: Photodiode response as counting events of particles. Every electrical pulse originates from a single particle/droplet that scatters light onto the detector.

1.2.3. Relevant Details

Aim of a Nozzle

A nozzle is not only responsible to separate the grown particles for counting but also serves additional purposes:

- droplets exit the nozzle and pass the light beam in the focal point of the lens system where the scattered light of each single droplet is collected.
- accelerated droplets are better separated in flow direction, which is why the probability of spatially coinciding occurences decreases. In time domain, electrical pulses are shorter and better separable in time. Droplets cannot be accelerated infinitely though due to hardware limitations.
- adiabatic cooling, as a consequence of the pressure drop downstream the nozzle, reinforces droplet growth and stabilizes its size

A counting approach based on nozzle designs requires maintaining a constant flow rate Q through the nozzle while measuring over a certain time

interval τ to derive particle number concentration C_N:

$$C_N = \frac{N}{Q \cdot \tau} \qquad (1.1)$$

Detector Response and its Information Content

Figure 1.2 illustrates the ideal case where every pulse response is well separated in time and corresponds to a single particle/droplet occurence. All pulses are of the same amplitude. The amplitude however is not only a function of the scattered light intensity and with it a function of the droplet size, but also of the optical hardware (wavelength, dimensions and intensity profile of the light beam) and the electronics hardware (photodiode, signal amplification and filtering). A real signal response is thus not perfectly uniform.
Smaller pulses imply smaller droplets since less light intensity is scattered. In CPCs therefore, a drop of signal amplitude is given rather as an indication of a deteriorating condensation process, and ultimately as a maintenance indicator (TSI Incorporated, 2007; Georg Brunnhofer, 2017).

The duration of the pulses depends mainly on the speed of movement of the droplets, their size and the path length through the light beam. The following applies: the faster droplets are passing the light beam, or the smaller they are, the shorter the scattered light pulses (provided that the path length through the light beam is unchanged). Typically, these counting events are of the order of some $100\,ns$ and therefore require fast counting electronics.

Sizing Capabilities

The size of the droplets is in the regime of Mie scattering, which is why the intensity of the scattered light changes in strong dependence of size and the scattering angle. The diameter can be evaluated by means of a Static Light Scattering (SLS) aparatus (Kupper, 2019; Cresnoverh, 2015; Buchberger, 2015). It scans the angular intensity distribution of the scattered light and calculates the droplet size on basis of the Lorenz-Mie model (Axmann,

2014; Øgendal, 2016). The examination requires a certain angular range which has to be covered by either detector arrays or rotational scanners. An implementation in standard CPCs is therefore not reasonable.

Theoretically, the droplet size is also determinable by the amplitude of the electrical pulses of the optical counting unit. However, the aforementioned dependences make an accurate droplet sizing impractical.

Coincidence of Particles

Particles are spatially separated by the nozzle and its acceleration. However, because of the small 3D viewing / measurement volume which is optically mapped onto the photo detector, there is a finite probability of multiple particles coinciding in that particular volume. In such scenarios, at least two particles are passing the light beam at the same time and create super-imposed electrical pulses which cannot be distinguished any more. Such occurences are called *Particle Coincidence* and limit the counting rates of CPCs as with increasing particle concentrations the probability of coincidence rises as well.

Coincidence corrections methods have been developed (Susanne V Hering et al., 2007; Collins, Dick, and Romay, 2013) but the automotive legislation for PN measurements (Official Journal of the European Union, 2011) regulates correction measures to a maximum of 10% of the measured concentration. Standard CPCs can measure particle concentrations up to $20.000 - 30.000 \frac{\#}{ccm}$ before reaching this coincidence limit.

1.2.4. Research Questions

Section 1.2 Condensation Particle Counter revealed various restrictions and boundary conditions of state-of-the-art counting units. Therein, a nozzle evidently represents the greatest constraint.

The following research questions may be derived:

1. **What is an alternative solution to nozzle-based counting designs?**
   A nozzle is the bottle neck in multiple senses. All particles must pass through it, which is why high particle densities inevitably lead to coincidence of particles/droplets.

2. **How could the probability of coincidence be reduced to measure higher particle concentrations?**
   The occurence of multiple particles being sampled at the same time results in detector responses that cannot be distinguished as single counting events any more. As a consequence, the measured particle count deviates from the real particle count (it is smaller) and is a function of particle density. The higher the concentration, the higher the probability of coincidence and the larger the deviation. Hence, coinciding particles require to be monitored from different viewing angles or by alternative methods to examine their mutual occlusion.

3. **How could a real volume-based determination of particle number concentrations be achieved?**
   Nozzle-based systems require a constant and known aerosol flow rate through the counting unit in order to obtain particle number concentrations. Since the sample volume is unknown, it must be determined with $V_s = Q_s \cdot \tau$, the sampling flow times a sampling interval. A known sampling volume allows an inherent determination of particle number concentrations with $C_N = N/V_s$ instead.

4. **Could the velocity of particles be minimized for the sake of a slower counting mechanism?**
   Faster particles aid in minimizing the probability of coincidence but add effort and complexity to the detection hardware and its counting

capabilities. While hardware and processing speed are nowadays no big challenge, more particles but at a reduced particle velocity may be screened at the same time scale instead.

5. **Is it possible to detect lowest particle number concentrations while extending the measurement range to higher rates?**
At very low concentrations the accuracy is limited by statistical errors (Maierhofer et al., 2019). A true single-particle detection is therefore only achievable when all particles in a sample volume are screened at once. Also, a detection of multiple particles at the same time may allow for higher counting rates.

6. **Could the quality of the condensation process be assessed by alternative and more accurate means?**
The final size of condensed particles is a function of the saturation ratio in the Condensation Nucleus Magnifier. Insufficient saturation results in insufficient particle growth or even failed particle activation. Although the influence of decreasing droplet sizes on detected scattered light pulses can be justified, the traceability to a qualitatively deteriorated condensation process is unreliable.

7. **Could particles/droplets be characterized in size, shape or morphology?**
The size of grown droplets is not only important as a quality indicator for CPCs. Micron sized droplets, particles, solids or cells are of general interest in terms of sizing and characterization. A novel optical counting unit may therefore be utilized in various fields of aerosol- or fluid measurements and characterization.

8. **Is particle/droplet sizing possible without static light scattering procedures and independent from the scattering angle?**
Static Light Scattering instruments are sophisticated sizing tools but bulky and not Real Time (RT)- capable. Furthermore, single-particle sizing is most often not possible.

9. **Are applications such as a Dual-Cutoff CPC or a Sizing CPC feasible?**
   Dual-Cutoff CPCs are subject to research and intend to magnify particles at two different Kelvin diameters and estimate the size distribution of activated particles. This means that one cutoff point defines the first minimum particle diameter for particle activation and the second aims another predefined size. A unified counting unit should be capable of discriminating grown particles from either magnification chamber in order to classify between the two size regimes and predict their size distribution.
   Sizing-CPCs pose an ultimate sizing solution which discriminate between multiple particles sizes and at finer increments. They may be understood as Multi-Cutoff CPCs but will be based on more sophisticated design variants of a Condensation Nucleus Magnifier.

10. **Could a counting unit be operated under harsh conditions, e.g. at hot temperatures?**
    Standard CPCs work at room temperature because their working fluids are only operable under fairly low temperature conditions. Novel working fluids enable CPC applications under harsh conditions and at hot temperatures (e.g.: $> 200^\circ$ C).

1.3. Motivation

In addition to the detailed research questions listed above, the basic motivation is reasoned in direct exhaust gas measurements at the tailpipe. State-of-the-art instrumentations require extensive preconditioning efforts to measure the very hot and humid exhaust gases which "additionally contain residual fuel and lubricating oil, but also aggressive compounds like sulphuric acid. This preconditioning comprises the removal of coarse particles, a hot dilution, the removal of volatile compounds and finally a cold dilution. By this process the sample is influenced to an unknown degree since a measurement directly in the exhaust gas is impossible" (Kupper, 2019).
Kupper covers different approaches of particle sensing in harsh environments and focuses in particular on a so called High Temperature Con-

densation Particle Counter (HT-CPC). The idea is to operate a CPC at hot temperatures to omit most of said preconditioning steps. This entails higher particle numbers since a dilution of the aerosol stream is also eliminated. In addition, a counting unit is now exposed to harsh conditions with temperatures above $180 - 200°C$.

> The herein presented PhD thesis was initiated as a work package for the development of a CPC working at high temperatures. This work addresses the research of an imaging-based counting approach which ideally should achieve counting rates $> 30.000 \#/cm^3$ and provide characterization capabilities for micron-sized particles.

1.4. Related Work

Experiments are reported back to Junge, 1935, where a camera photographed the number of suspended droplets in a known volume. Later, Kassner Jr et al., 1968 and Jaenicke and Kanter, 1976 developed automated instruments to determine the number of activated droplets and the aerosol concentration. However, due to the lack of continuous flow capability, these instruments primarily served for calibrations of newer types of CPCs, in which the particles are detected by photoelectrical means.

More recently, Falk (2014) started research activities on that topic and investigated approaches to provide a visual-based particle detection and counting. His master thesis focuses on the simulation and design of different optical setups in the bright and dark-field mode using linear or 2-dimensional detector arrays. Falk concluded that bright-field setups, with a theoretical gain of the counting limit of up to $100.000 \#/cm^3$, are most promising and feasible. His simulations and optical designs disregard light diffraction at particles though and address shadow imaging applications in the first place. In his experiments, however, he recorded particles as diffraction patterns

and thus established that his bright-field arrangement actually corresponds to an in-line holographic alignment.

The master thesis of Cresnoverh (2015) builts on Falk's findings and elaborates DIH for the application of particle counting. He recorded holograms with an open-space in-line holographic setup directly positioned above the outlet of a CNM (see Figure 1.3). He observed that the count of diffraction patterns in the hologram indeed correlates to the number of captured particles and thus showed that the DIH is suitable for reliable particle counting.
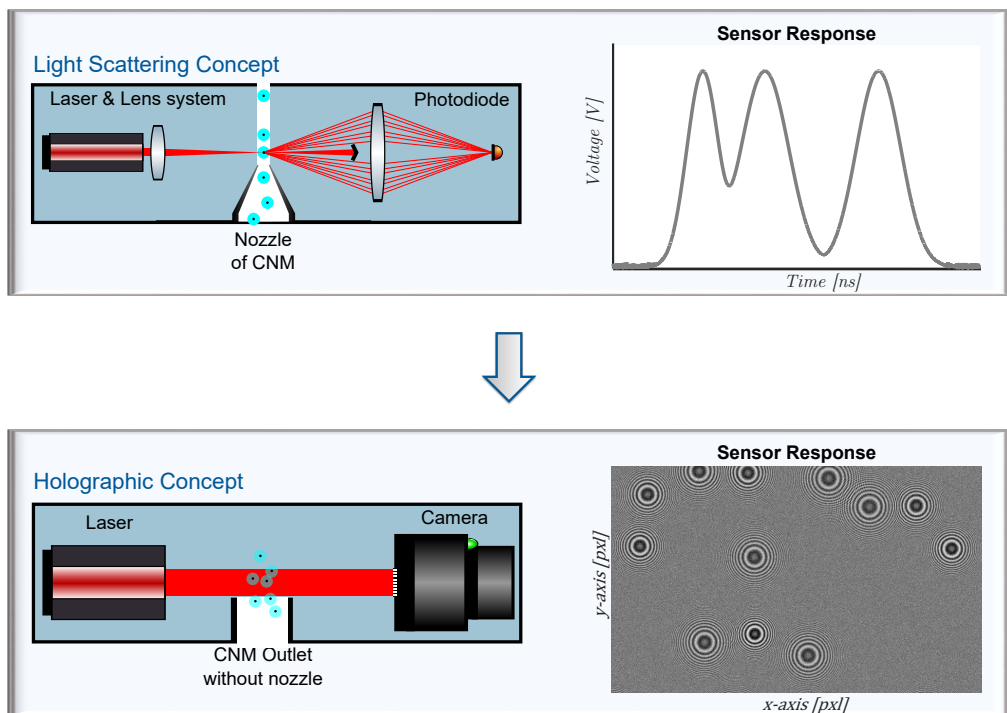
Figure 1.3.: Technology transfer from a light scattering based counting approach (top) to a holographic concept (bottom) for CPCs. The sensor response changes from a time-domain signal to an area-based signal. Counting events are no longer time signal pulses but 2-dimensional diffraction patterns.

He also manually reconstructed the wavefront of selected particles to proof the sizing capabilities and experimented with particle velocities to estimate the aerosol flow rate and flow profile. Cresnoverh's findings gave reasons for further studies and constituded the advent of this PhD thesis.

Although the holographic approach is already established in Holographic Particle Image Velocimetry (HPIV) (Hinsch, 2002) and is used to investigate aerosol particle morphology (David et al., 2018; Berg et al., 2017), to the knowledge of the author it is the first implementation as a counting method, in particular for CPCs.

1.5. Scope of the Thesis

While Cresnoverh provided a rather empirical proof of concept for holographic particle counting the scope of this thesis is to:

1. simulate digital holography and design a comprehensive model of holographically imaged particles to create a basic understanding of particle holograms. The model should further aid the development of a holographic sensor system.
2. identify pattern recognition algorithms that automatically detect and evaluate diffraction patterns
3. implement these algorithms into e.g.: MatLab or a Real Time platform for the detection of particle density, particle size, particle velocity and wettability
4. develop a sensor system as closed sampling cell to establish a holographic based Condensation Particle Counter.
5. validate the sensor system using model aerosols such as soot or Sodium Chloride (NaCl), and referencing equipment like a Condensation Particle Counters, Scanning Mobility Particle Sizer (SMPS) or Static Light Scattering.

2. Digital Holography

2.1. Introduction to Holography

2.1.1. History

In 1948, the Hungarian-British physicist Dennis Gabor published a method of wavefront reconstruction as *A new Microscopic Principle* to improve the resolution in images obtained with an electron microscope. With reference to resolving limits of microscopes, set by the spherical aberration of lenses, he invented the "new principle that provides a complete record of amplitude and phase in one diagram, and is applicable to a very general class of objects" (Gabor, 1948). The mentioned diagram is later known as a *hologram* which, when illuminated with an optical imitation of the original wave, reconstructs the wavefront of the imaged object at its initial position. He was able to prove his method in principle, but his reconstructions suffered from vast imperfections due to the lack of coherent light sources at that time.

Nevertheless, Gabors so called *Wavefront Reconstruction* was the enabler to analyze dynamic volumes rather than just a plane. "The study of very small objects in a dynamic volume is of significant importance in modern science and technology. Particles, bubbles, aerosols, droplets, etc. play key roles in processes dealing with nozzles, jets, combustion, turbines, rocket engines, cavitation, fog, raindrops, pollution and so on" (Vikram, 2005).
Conventional microscopic techniques may be the logical thought to resolve small objects but resolution is not the problem. Ordinary imaging systems that can resolve objects of a diameter of d have a Degree of Freedom (DoF') of only about d^2/λ (with λ being the wavelength of illumination) which is

not satisfactorily and thus disqualifies conventional microscopic approaches from volume studies.
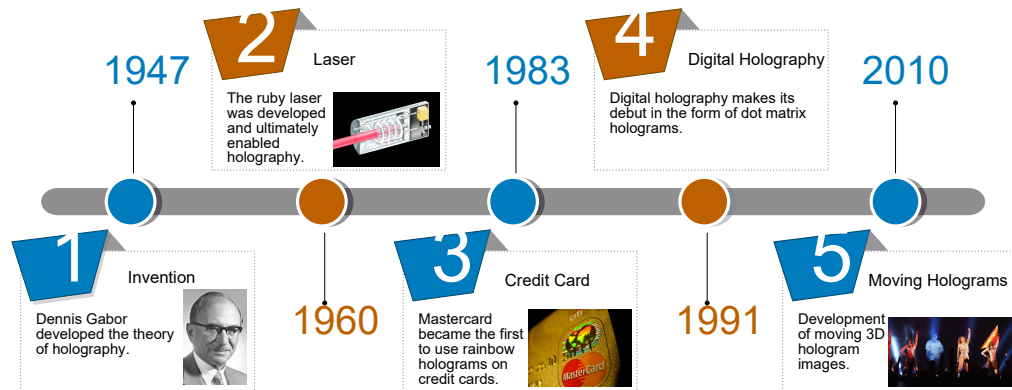

Figure 2.1.: Timeline of holography with some of the most relevant and perceived milestones (Teja, 2015; IHMA, 2019)

The breakthrough was only achieved with the development of the first Laser - Light Amplification by Stimulated Emission of Radiation - in 1960. The operation of a first functioning laser - a solid state laser made of a ruby cristal - but also the invention of the first Helium-Neon (HeNe) laser as a gas laser boosted the advancement in holography.

With the first commercially installed hologram, Mastercard and VISA equipped their credit cards with rainbow holograms in 1983, thereby revealing the potential of holography to the general public. Holograms of such type were the first to be viewed under white light illumination and change their spectral colors when moving up and down. Because perspective effects are reproduced along one axis only, its intention and common usage then, as today, is for security and authentication purposes.

2.1.2. Principle of Holography

Originally referred to as *Wavefront Reconstruction* by Gabor, it is now called holography (from the greek words *holos* = whole or complete, and *graphy* = writing). A recording medium being used in an holographic progress

therefore contains the "complete" information of an imaged scene or object. The result of the recorded information is called a hologram and is "the interference pattern, formed when a point source of light of fixed wavelength encounters light of the same fixed wavelength arriving from an object" (Jeong, 2008).

In other words: when an object is illuminated by a light source of fixed wavelength λ, it diffracts the incident wavefront. At the recording medium, the diffracted object wave and the reference wave of the light source superimpose and create a diffraction pattern.
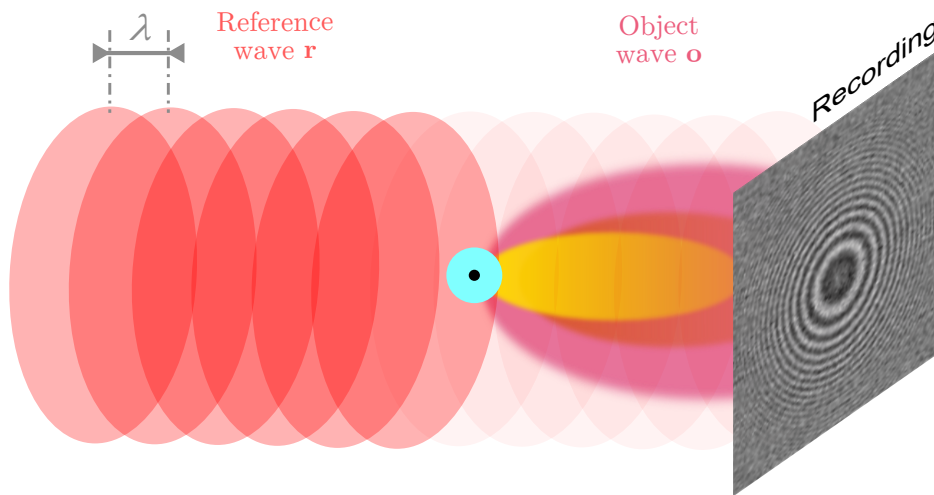
Figure 2.2.: Holographic principle by means of a point-like object

The superposition at the recording medium gives an intensity distribution I of:

$$I = |\mathbf{r} + \mathbf{o}|^2 \qquad (2.1)$$

$\mathbf{r}$ ... Complex amplitude of the reference wave
$\mathbf{o}$ ... Complex amplitude of the object wave

A wave front is generally characterized by the quantities *amplitude* and *phase*. In case of an object wave, the amplitude corresponds to the brightness or

intensity of recorded objects and the phase to the objects' shapes. Both, the amplitude and the phase are conveniently denoted by the so-called complex amplitude (**o** as the complex amplitude of the object wave and **r** as the complex amplitude of the reference wave). The complex amplitude contains the complete information of the object.

In order to illustrate the information content of a hologram in more detail, Equation (2.1) is solved to get the intensity distribution as follows:

$$
\begin{aligned}
I &= |\mathbf{r} + \mathbf{o}|^2 \\
&= (\mathbf{r} + \mathbf{o})(\mathbf{r} + \mathbf{o})^* \\
&= |\mathbf{r}|^2 + |\mathbf{o}|^2 + \mathbf{ro}^* + \mathbf{r}^*\mathbf{o}
\end{aligned}
\tag{2.2}
$$

Note:

When squaring complex values the complex conjungate must be borne in mind with the rule:

$$\mathbf{z} \cdot \mathbf{z}^* = |\mathbf{z}|^2 = z^2$$

It shows that the "intensity at any point in the interference pattern is the sum of the intensities r^2 and o^2 of the individual waves plus an interference term"(Collier, Burckhardt, and Lin, 1971). The interference term $\mathbf{ro}^* + \mathbf{r}^*\mathbf{o}$ contains the relative phase information.

2.1.3. Photography versus Holography

In the case of photography, the illumination is a polychromatic, diffuse and undirected light source - typically daylight. Because of diffuse daylight, in fact only the object wave is recorded when taking a photo. Since recording media respond to light intensities only, what is recorded is the variation

of the light intensity at the plane of the recording medium. Mathematically speaking, the intensity $I(x,y)$ is proportional to the squared complex amplitude:

$$I(x,y) \propto |\mathbf{o}(x,y)|^2 = o^2 \tag{2.3}$$

"In photography, as a result of intensity recording, all information about the relative phases of the light waves from the original 3-dimensional scene is lost" (Poon and Liu, 2014).

2.1.4. Types of Holograms

Although there are many ways of classifying holograms, a categorization into three general types can be summarized (Jeong, 2008):
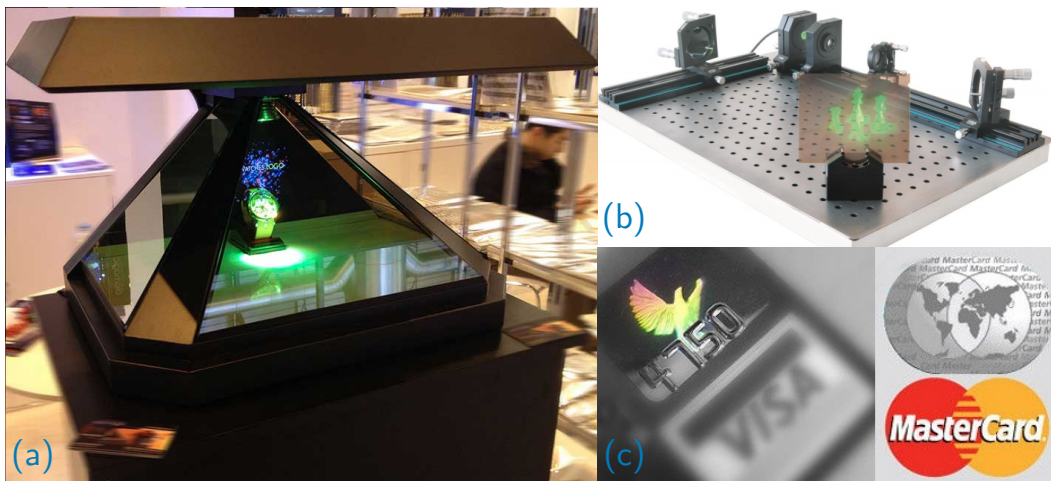

Figure 2.3.: Examples of hologram types:
(a) Holographic Displays from Olomagic (Olomagic, 2017) based on reflection holograms.
(b) Demonstrator to create transmission holograms from (ELas, 2018).
(c) Rainbow hologram as security feature on credit cards.
(Source: https://www.quora.com/Why-do-credit-and-debit-cards-all-have-holograms)

- **Reflection Holograms** are made with the reference beam on the opposite side of the object. The hologram is illuminated from the viewers side to recreate the object. In this manner, the recreated image consists of light *reflected* by the hologram. It is the most common type in arts and is shown in galleries where the illumination source is mostly a "light spot" of white incandescent light. Reflection holograms require the simplest optical setup (see Figure 2.3).

- **Transmission Holograms** are made with both reference and object beam on the same side. The recreated image is transmitted to the viewers side as the reference light is directed from behind the hologram. Typical applications are projection screens to visualize advertisement objects or films.

- **Hybrid Holograms** are variants between transmission and reflection holograms and are very diverse.
    - *Embossed Hologram* are pressed holograms on a foil that are well known from credit cards such as the eagle on VISA cards (strictly speaking the eagle is a "rainbow" hologram). Holograms of this type show a change in color in a certain direction.
    - *Integral Holograms* are made of a series of photographs where the object is usually recorded in many views. A stereoscopic image is observed when the object is recreated.
    - *Holographic Interferometry* is used to reveal microscopic changes on objects such as heat waves or shock waves. The object is exposed at least twice in order to let two images interfere with each other. In real-time holographic interferometry, the displacement vector can be revealed by directly comparing the virtual image with the real object.
    - *Computer-generated Holograms* are mathematical models which are very well understood. If any two of the three essential elements - light source, object and hologram - are known, the third can be computed.

Based on the alignment of the optical setup, another distinction of types is important:

- *in-axis* or *in-line* holography was the very first assembly from Gabor. It comprises the three basic elements - a light source, an object and a recording medium - that are aligned in-line (see also in Figure 2.2 on page 17). All elements are on the same optical axis. Due to its simplicity in alignment, savings in optical elements and further advantageous (discussed later) it is still very widespread.
- *off-axis* holography is more complex. The reference beam and the object beam are impinging from different angles onto the recording medium. This requires additional Holographic Optical Elements (HOEs). Off-axis setups are common in the recording of holograms and will be shown later in this section to illustrate the recording and reconstruction process.

This thesis is based on the mathematical understanding of holography where a large emphasis is on focusing on the development of a digital twin of aerosol particles. An in-line alignment is favored over off-axis setups, not only due to its simplicity in Holographic Optical Elements but also because of its practicability.

2.1.5. Illustration of Hologram Recording & Reconstruction

As previously mentioned, the hologram recording process is typically carried out in an *off-axis* or off-beam configuration. Figure 2.4 illustrates such a process where an object is illuminated from the left. One part of the illumination beam is decoupled by a beamsplitter to be "reused" over a mirror as the reference wave $\mathbf{r}$. In an offset angle of θ it is directed onto the holophic plate where it finally interfers with the object wave $\mathbf{o}$, diffracted by the object.
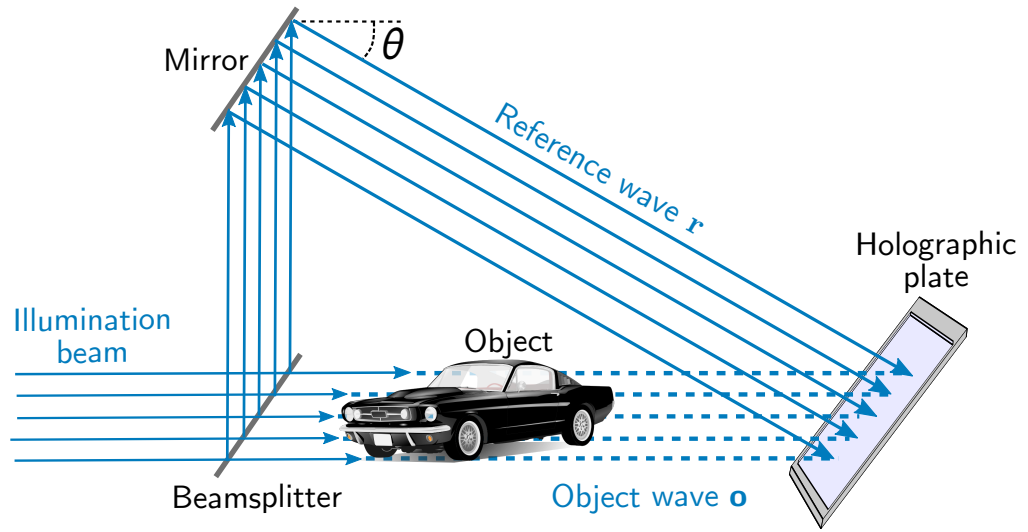
Figure 2.4.: Hologram creation using an off-beam setup

Because the hologram now comprises the phase information of the object as noticed in Equation (2.2), the wavefront originally coming from the object can be reconstructed. The reconstruction is achieved when illuminating the recording medium by its original light source (Wieland, 2015; Vikram, 2005):

$$
\begin{aligned}
\mathbf{u} &= \mathbf{r} \cdot I \\
&= \mathbf{r}\left(|\mathbf{r}|^2 + |\mathbf{o}|^2\right) + \mathbf{r}^2\mathbf{o} + \mathbf{r}\mathbf{r}\mathbf{o}^* \\
&= \mathbf{u_0} + \mathbf{u_{+1}} + \mathbf{u_{-1}}
\end{aligned}
\tag{2.4}
$$

The wavefront reconstruction in Equation (2.4) gives three terms. The first term $\mathbf{u_0}$ is the zeroth-order diffraction and represents the reference wave $\mathbf{r}$ attenuated by a factor of $\left(|\mathbf{r}|^2 + |\mathbf{o}|^2\right)$. The second term $\mathbf{u_{+1}}$ is proportional to the object wave $\mathbf{o}$ and is the exact replica of the original object field. It represents the reconstructed object and is termed a virtual image (also primary or orthoscopic image). The third term $\mathbf{u_{-1}}$ denotes the complex conjugate object wave $\mathbf{o}^*$ and yields an inverted wavefront that is formed on the opposite side of the hologram from the illumination source. It is also referred to as the conjugate image to the original.
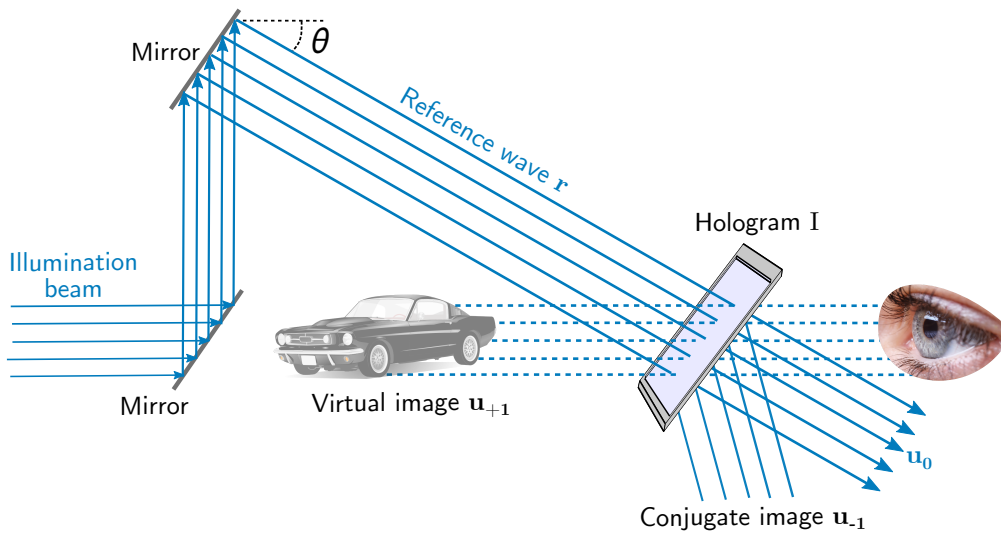
Figure 2.5.: Reconstruction of the original object using the same off-beam setup as when creating it in Figure 2.4

The wave reconstruction process in Figure 2.5 is conducted in the identical off-beam setup as before but now the previously recorded medium and, ultimately, the hologram I is illuminated. An observer watching behind the holographic plate will recognize a virtual image $\mathbf{u_{+1}}$ of the object, situated at its original location. Because of the off-axis setup with a reference beam offset θ, the zeroth-order diffraction $\mathbf{u_0}$ from Equation (2.4) is moved outside the observers view which reveals the major advantage of that type of holography. The conjugate image $\mathbf{u_{-1}}$ (not illustrated as object) is formed on the opposite side of the hologram and is inverted to the original. Instead of a beamsplitter and for the sake of a simplified illustration[1], a mirrow is used to redirect the illumination beam and prevent the reconstruction location from disturbances.

Assuming the described process in an *in-line* arrangement with the axis offset $\theta = 0$, the conjugate image and the reference beam are in the same line of sight of the observer. The virtual image and its inverted conjugate overlay in the view of the observer and wouldn't be identifiable.

---

[1] The beamsplitter would remain in the setup. Instead, a beamtstop would be used to keep the illumination beam off from the reconstructed image.

For point-like objects the superposition of the virtual and the conjugate image does not matter due to its radial symmetry. Thus, an in-line alignment is indeed practicable for aerosol measurements.

2.2. Fundamentals of Holography

Starting over with the basic mathematical formulation of creating holograms in Equation (2.1) on page 17 and denoting now the complex amplitudes of the reference wave as Ψ_r and the object wave as Ψ_{prt}, the intensity distribution on a recording medium is follows:

$$I = \Psi(x, y) = |\Psi_r + \Psi_{prt}|^2 \tag{2.5}$$

Both, Ψ_r & Ψ_{prt} are field distributions along the xy-plane in the subsequent sections. The recording medium - a camera as in Figure 2.6 - records the interference[2] $\Psi(x, y)$ of the reference wave Ψ_r and the object wave Ψ_{prt}, provided that both waves are mutually coherent over the recording plane. The coherence of the illumination wave is guaranteed by the use of a laser source which emits plane waves with a wavelength λ.

It is important to note that the droplet in Figure 2.6 and in particular, its geometry, is the determinant source of diffraction. However, for the sake of simplicity, droplets, particles or particles as nuclei in droplets are hereafter referred to as *particles*.

---

[2]This intensity distribution in analog holography is often also denoted as an amplitude transmittance $t(x, y)$ or $T(x, y)$ since holograms on holographic emulsions or plates are important in their transparency.

[3]Note: the object here is illustrated as a droplet (bright blue) of diameter d_{prt} with a particle as nucleus (dark spot). That is the given case in the application of CPCs. The determinant dimension for holographic imaging is the diameter of the droplet.
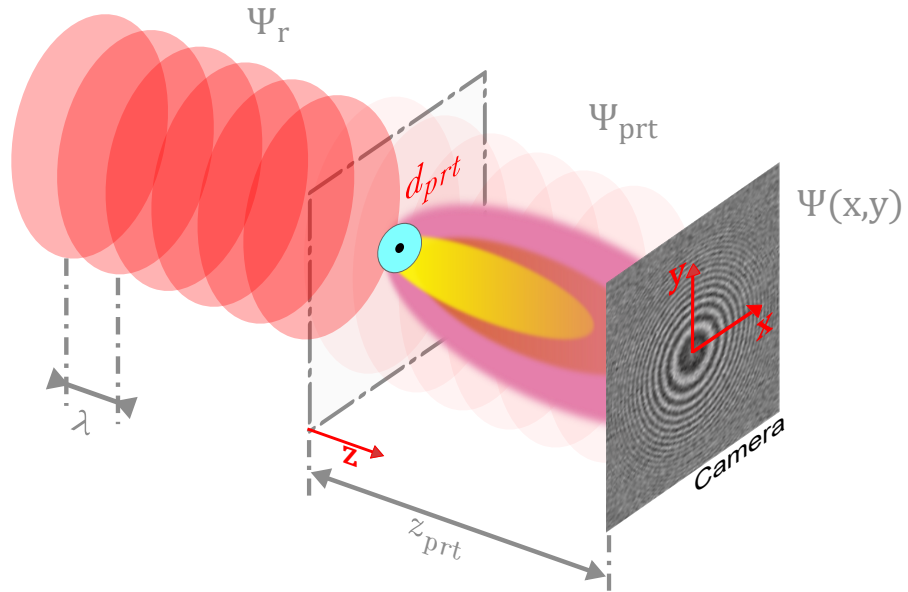
Figure 2.6.: In-line holographic principle where a point-like object with diameter d_{prt} generates a spherical wave Ψ_{prt} upon a plane wave Ψ_r of wavelenght λ, incident onto the object[3]. A camera records the field distribution $\Psi(x, y)$ of the interference of both waves in a distance of z_{prt}.

Point-like objects, such as particles, diffract the incident light wave and generate a diverging spherical wave towards the recording medium. Equation (2.5) describes the field distribution as a result of the interference of a plane wave and a spherical wave in a given distance z_{prt} away from the object. A particle can be modelled as an aperture of diameter d_{prt} for which an object plane is introduced.

2.2.1. Plane Waves & Spherical Waves

Originating from Maxwell's equations the three- dimensional scalar wave equation is yielded by:

$$\nabla^2 \psi = \frac{1}{v^2} \frac{\partial^2 \psi}{\partial t^2} \tag{2.6}$$

where ψ can represent a component, $E_x, E_y,$ or E_z of the electric field E and $v = 1/\sqrt{\mu\varepsilon}$ is the velocity of the wave in a medium. From that, the two simplest solutions, the *plane wave* and the *spherical wave* solution can be derived.

The *plane wave* solution in Cartesian coordinates is:

$$\psi(x,y,z,t) = A\, e^{j(\omega_0 t - \mathbf{k_0} \cdot \mathbf{R})} \tag{2.7}$$

$\mathbf{k_0} = k_{0x}\mathbf{a_x} + k_{0y}\mathbf{a_y} + k_{0z}\mathbf{a_z}$ ... propagation vector
$\mathbf{R} = x\mathbf{a_x} + y\mathbf{a_y} + z\mathbf{a_z}$ ... position vector
$|\mathbf{k_0}| = k_0 = \sqrt{k_{0x}^2 + k_{0y}^2 + k_{0z}^2} = \frac{\omega_0}{v}$ ... wave number
                                                   $(v = c$ in free space)

It represents a plane wave of amplitude A, propagating along the $\mathbf{k_0}$ direction. For in-line holographic arrangements, a plane wave may be defined as traveling in z- direction for instance and Equation (2.7) simplifies to:

$$\psi(z,t) = A\, e^{j(\omega_0 t - k_0 z)} \tag{2.8}$$

The spherical wave solution has spherical symmetry and is, thus, represented in spherical coordinates. A *spherical wave* of amplitude A in spherical coordinates is:

$$\psi(R,t) = \frac{A}{R}\, e^{j(\omega_0 t - k_0 R)} \tag{2.9}$$

2.2.2. Diffraction by a Particle

As already mentioned, a particle is considered a point-like source that may be modelled as an aperture of the same cross-section with a diameter d_{prt} as the particle. An aperture is represented by a transparency function[4] $t(x,y)$ situated at the initial propagation location at $z = 0$.

---

[4]"In general, $t(x,y)$ is a complex function that modifies the field distribution incident on the aperture, and the transparency has been assumed to be infinitely thin."

As the aperture gives rise to the object wave it is a crucial plane for modelling. Later, in chapter 3 The Holographic Aerosol Particle Model it will be referred to as object plane.
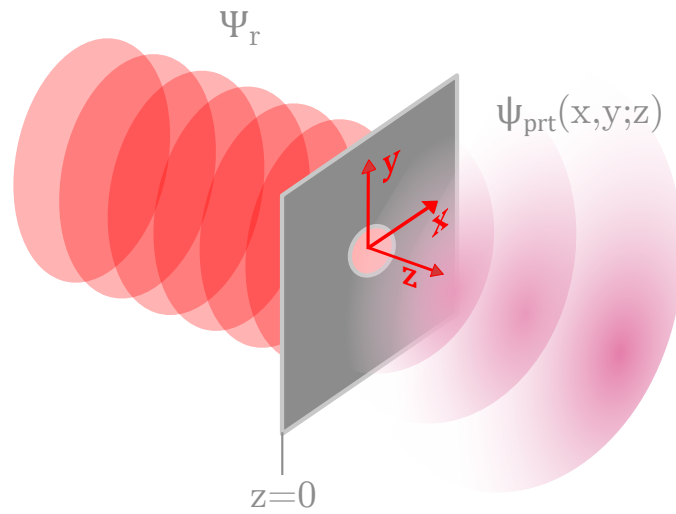
Figure 2.7.: Diffraction geometry: $t(x,y)$ is a diffracting screen

Diffraction by a particle is mathematically described as a plane wave Ψ_r of Equation (2.9) being incident on the aperture with a transparency function of $t(x,y)$. The diffracted field after the aperture - the field distribution $\psi_{prt}(x,y;z)$ as illustrated in Figure 2.7 - is obtained by first finding the initial condition immediately after the aperture at $z = 0$:

$$\psi(x,y,z=0,t) = t(x,y) \cdot A\, e^{i(\omega_0 t)}$$
$$= \psi_{prt0}(x,y)e^{i\omega_0 t} \tag{2.10}$$

The term $\psi_{prt0}(x,y) = A \cdot t(x,y)$ is called the *complex amplitude* and is the initial condition to obtain the unknown field distribution $\psi_{prt}(x,y;z)$ at z away

from the particle. It is obtained by substituting the above Equation (2.10) into the three-dimensional scalar wave equation Equation (2.6) and solving its resulting *Helmholtz equation*. The solution to the Helmholtz equation is found by making use of the Fourier Transform (here without proof - cf. Appendix A.1 or Poon and Liu, 2014).

In Fourier space, the solution to Equation (2.10) is straightforward and yields a simple multiplication of the initial condition $\Psi_{prt0}(k_x, k_y)$ with a term $\mathcal{H}(k_x, k_y; z)$ called the *spatial frequency transfer function* of propagation:

$$\Psi_{prt}(k_x, k_y; z) = \Psi_{prt0}(k_x, k_y) \cdot e^{-jk_0 z \sqrt{\left(1 - k_x^2/k_0^2 - k_y^2/k_0^2\right)}}$$

$$= \Psi_{prt0}(k_x, k_y) \cdot \mathcal{H}(k_x, k_y; z) \qquad (2.11)$$

k_x, k_y ... *spatial radian frequencies* with units of radian per unit length

$\Psi_{prt0}(k_x, k_y)$ ... *angular plane wave sprectrum* of the field distribution $\psi_{prt0}(x, y)$

$\mathcal{H}(k_x, k_y; z)$ ... *spatial frequency transfer function* of propagation through a distance z

$\Psi_{prt}(k_x, k_y; z)$ ... *angular plane wave spectrum* in a distance z

Note:

> Field distributions Ψ are annotated with capital greek letters to describe spatial wave fronts. On the contrary, small greek letters ψ originate from time domain representation of the wave equation. A Fourier transform links both domains by $\mathcal{F}\{\psi(x, y)\} = \Psi(k_x, k_y) = \iint_{-\infty}^{\infty} \psi(x, y) e^{j(k_x x + k_y y)} dx dy$.

Eventually, the field distribution in a distance z away from the object plane is found with the inverse Fourier Transform and leads to a solution with crucial physical meaning:

$$
\begin{aligned}
\psi_{prt}(x,y;z) &= \mathcal{F}^{-1}\{\Psi_{prt0}(k_x,k_y) \cdot \mathcal{H}(k_x,k_y;z)\} \\
&= \frac{1}{4\pi^2} \int\int_{\infty}^{-\infty} \Psi_{prt0}(k_x,k_y) \cdot \underbrace{e^{-jk_0z\sqrt{\left(1-\frac{k_x^2}{k_0^2}-\frac{k_y^2}{k_0^2}\right)}}}_{\substack{\text{propagation in z-direction}\\ \text{by } e^{-jk_{0z}z}}} \cdot e^{-j(k_xx+k_yy)} dk_x dk_y \\
&= \mathcal{F}^{-1}\{\Psi_{prt0}(k_x,k_y) \cdot e^{-jk_{0z}z}\}
\end{aligned}
\tag{2.12}
$$

When knowing the field distribution $\psi_{prt}(x,y,z)$ at the object plane at $z=0$ the field distribution at a plane parallel to it in a distance z can be calculated. The initial field distribution $\psi_{prt0}(x,y)$ at the particle is a plane wave propagating with the propagation vector $\mathbf{k}_0$, reprensented in Cartesian coordinates with $k_0 = \sqrt{k_{0x}^2 + k_{0y}^2 + k_{0z}^2}$. As in in-line holography, a propagation along the z- coordinate is typically defined, the propagation component k_{0z} is of interest which takes the form $k_{0z} = k_0\sqrt{\left(1 - k_x^2/k_0^2 - k_y^2/k_0^2\right)}$.

In Fourier space, the initial plane wave is called the *angular plane wave spectrum* and is represented by $\Psi_{prt0}(k_x,k_y) \cdot e^{-j(k_xx+k_yy)}$ with the amplitude $\Psi_{prt0}(k_x,k_y)$ and k_x, k_y the *spatial radian frequency* variables corresponding to the (x,y) plane at the particle. It is multiplied with the *spatial frequency transfer function* of propagation $\mathcal{H}(k_x,k_y;z)$ which describes the spatial propagation along the z- direction. This simply means a phase shift of $e^{-jk_{0z}z}$ to the initial field distribution $\Psi_{prt0}(k_x,k_y)$ in frequency domain.

The transform itself reveals the essence of diffraction at an aperture in Fourier optics. Thus, a recorded image in a distance z away from the aperture depicts the spatial field distribution diffracted by the particle.

2.2.3. Fresnel Diffraction

The previously obtained propagation term in Equation (2.12) may be simplified under the terms of Fresnel diffraction.

A wave propagating in z- direction means $k_{0z} \geqslant 0$ and therefore requires the condition $1 - k_x^2/k_0^2 - k_y^2/k_0^2 \geqslant 0$ or $k_x^2 + k_y^2 \leqslant k_0^2$ to satisfy. When propagating waves make small angles to its propagation axis (here in z- direction), the above condition turns to $k_x^2 + k_y^2 \ll k_0^2$ and a so called *paraxial approximation* may be applied. Fresnel diffraction makes use of that and approximates the phase of the spatial frequency transfer function $\mathcal{H}(k_x, k_y; z)$ as follows:

$$\sqrt{\left(1 - k_x^2/k_0^2 - k_y^2/k_0^2\right)} \approx 1 - \frac{k_x^2}{2k_0^2} - \frac{k_y^2}{2k_0^2} \tag{2.13}$$

and gives a notation of[5]:

$$H(k_x, k_y; z) = e^{-jk_0 z} \cdot e^{j\frac{k_x^2 + k_y^2}{2k_0}z} \tag{2.14}$$

This resulting propagation term is also called *spatial frequency transfer function* but is the paraxial approximation of $\mathcal{H}(k_x, k_y; z)$. The inverse Fourier Transform of $H(k_x, k_y; z)$ is known as the *spatial impulse response* and is:

$$h(x, y; z) = \mathcal{F}^{-1}\left\{H(k_x, k_y; z)\right\}$$
$$= e^{-jk_0 z} \frac{jk_0}{2\pi z} e^{-j\frac{k_0}{2z}\left(x^2 + y^2\right)} \tag{2.15}$$

---

[5]note the ordinary letter H($\cdot$)

2.3. Fringe Pattern - The Hologram of a Particle

Now that a plane reference wave Ψ_r and the diffracted object wave Ψ_{prt} of a particle are described, the hologram on a recording medium may be calculated according to Equation (2.5). A recap for clarity:

$$I = \Psi(x,y) = |\Psi_r + \Psi_{prt}|^2 \tag{2.16}$$

The complex amplitude Ψ_{prt} may now be expressed by means of a delta function $\delta(x,y)$ that models the particle giving rise to an object wave according to Fresnel diffraction:

$$\Psi_{prt}(x,y;z_{prt}) = \delta(x,y) * h(x,y;z_{prt})$$
$$= e^{-jk_0 z_{prt}} \frac{jk_0}{2\pi z_{prt}} e^{-j\frac{k_0}{2\cdot z_{prt}}(x^2+y^2)} \tag{2.17}$$

The above solution is the field distribution in a distance z_{prt} away from the particle. Particles in this thesis are considered ideal with no phase determining properties such as the refractive index[6]. Therefore, the delta function in Fourier space is 1 and the convolution shortens to the impulse response term, known from Equation (2.15).

The reference wave Ψ_r is assumed to have the same initial phase as the particle. Its mathematical expression is thereby found in Equation (2.14), where the solution of the plane wave in a distance z_{prt} is straightforward with $\Psi_r = A e^{-jk_0 z_{prt}}$ and an amplitude A. It is clear that ideal plane waves have the same field distribution along its entire propagation path z. In practice, this assumption is also valid in distances much smaller than the coherence length of the light source.

---

[6]A model based on Lorenz-Mie theory (Bohren and Huffman, 2008) was deliberatly omitted in this thesis. It should solely support in the understanding and development of a holographic Particle Counter.

A substitution into Equation (2.16) now gives the final solution of a hologram recorded in a distance z_{prt} away from the particle:

$$
\Psi(x,y) = |\Psi_r + \Psi_{prt}|^2 = \left| A \cdot e^{-jk_0 z_{prt}} + e^{-jk_0 z_{prt}} \frac{jk_0}{2\pi z_{prt}} e^{-j\frac{k_0}{2 \cdot z_{prt}}(x^2+y^2)} \right|^2
$$

$$
= A^2 + \left(\frac{k_0}{2\pi z_{prt}} \right)^2 + A\frac{k_0}{2\pi z_{prt}} \left[\frac{1}{j} e^{j\frac{k_0}{2 \cdot z_{prt}}(x^2+y^2)} - \frac{1}{j} e^{-j\frac{k_0}{2 \cdot z_{prt}}(x^2+y^2)} \right]
$$

$$
= C_1 + C_2 \cdot sin\left(\frac{k_0}{2 \cdot z_{prt}}(x^2 + y^2) \right) \qquad (2.18)
$$

The above result now complies with the already sketched derivation of page 18: a bias resulting from the reference wave $|\mathbf{r}|^2$ and from the object wave $|\mathbf{o}|^2$. Both are summarized as $C_1 = A^2 + \left(\frac{k_0}{2\pi z_{prt}} \right)^2$. The phase information of the hologram is given as a sine-function of amplitude $C_2 = A\frac{k_0}{\pi z_{prt}}$.

2.3.1. Fresnel Zone Plate (FZP)

The solution in Equation (2.18) is called the sinusoidal Fresnel Zone Plate and is an interference pattern of a set of radially symmetric rings. The rings carry the information of the distance z and are also referred to as fringes, which give the pattern also the name *fringe pattern*.

Note:

> The name *fringe pattern* will mainly be used throughout this thesis when talking about particles' holograms. Its analogy to Fresnel Zone Plates (FZPs) is crucial though and referred to also.
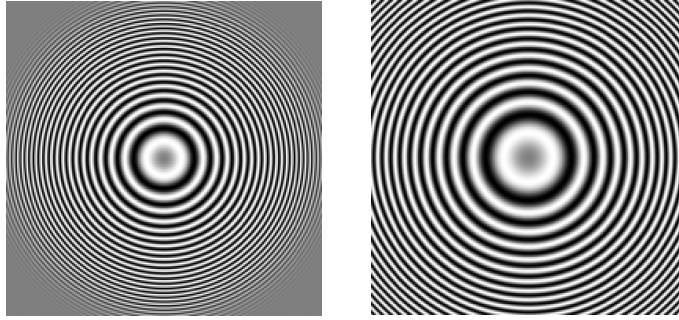
Figure 2.8.: Fringe pattern of particles in an arbitrary distance $z = z_{prt}$ and $z = 2z_{prt}$

Figure 2.8 compares two fringe patterns[7] schematically, the left with an arbitrary distance of $z = z_{prt}$ and the right with double the distance $z = 2z_{prt}$. It is now evident that the radii of fringes and thus the extent of a fringe pattern depends on z_{prt}, where particles in a larger distance yield large fringe patterns and closely located particles smaller patterns.

The *local fringe frequency* increases linearly with the x and y coordinate. This spatial rate of change of the phase is given by (Poon and Liu, 2014):

$$f_{local} = \frac{1}{2\pi} \frac{d}{dx} \left(\frac{k_0}{2z_{prt}} x^2 \right) = \frac{k_0 x}{2\pi z_{prt}} \tag{2.19}$$

Note:

$$2\pi f = \omega = \frac{d\varphi}{dt} \xrightarrow{here} \frac{d\varphi}{dx} \tag{2.20}$$

Fresnel Zone Plates are well known in the field of x-ray microscopy to be utilized as diffractive image forming lenses (Attwood and Sakdinawat, 2017) or in Digital Signal Processing (DSP) to test filter approaches (Gonzalez and Woods, 2001). For the latter, the linear increase of fringe frequency in

---

[7]If symmetric effects appear at all four borders of the image, this comes from Aliasing caused by low resolution displaying or printing (explained later in 3.2.2 Criteria for Sampling).

Equation (2.19) is used to check the characteristic of low-, high- or bandpass filters[8].

In optics, the focusing properties of FZPs are essential and helpful for the later development of detection & analyses algorithms.

2.3.2. Fringe Pattern vs. Fresnel Zone Plate

A zone plate resembles the fringe pattern where each zone may be interpreted as a fringe. The only important difference is sharp edges in the zone plate distribution, as opposed to the smooth transparency of fringe patterns. The spacing of the plate's zones is such, that light transmitted by the transparent zones constructively interferes at a desired focus. Fringe patterns follow the same principle, its interference rings are caused by a common focus point - the particle.

The **Radius** R_n of each zone n in FZPs is dependent on the focal length f in Figure 2.9. The focal length corresponds to the distance z_{prt} from the particle to the detection plane.

$$R_n \simeq \sqrt{n \cdot \lambda_0 \cdot z_{prt}} \qquad (2.21)$$

with λ_0 the wavelength of the illumination light (Attwood and Sakdinawat, 2017). At the detection plane, constructive interferences appear as bright fringes and correlate to zones of even multiples of n on the illustrated zone plate above.

---

[8]Later in this thesis, an application is shown to determine the cutoff frequency of a lowpass filter.
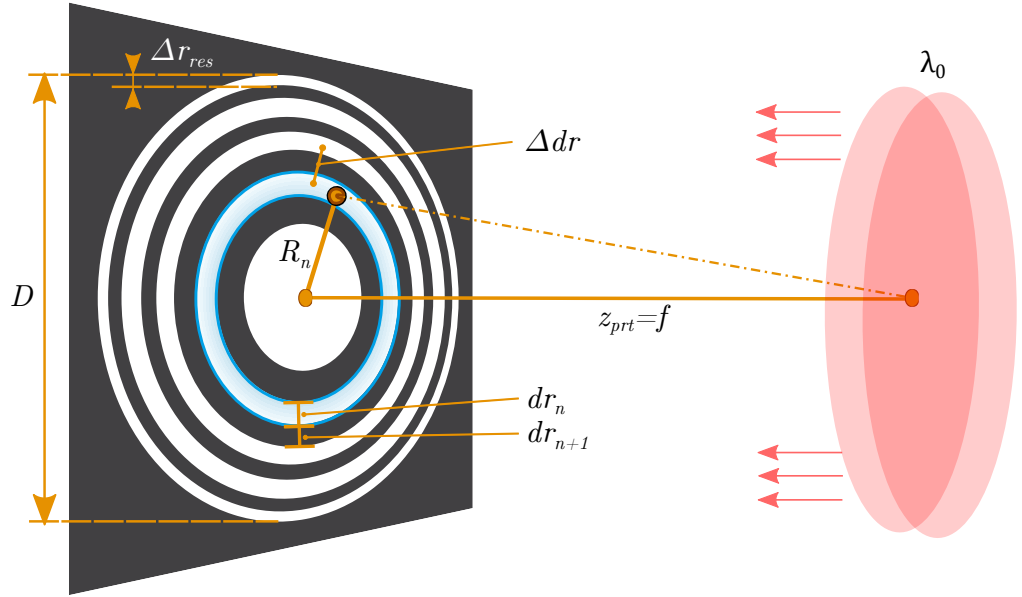
Figure 2.9.: Fresnel Zone Plate (FZP) and its most relevant parameters in relation to fringe patterns: the zone plate size D; the zone plate resolution Δr_{res}; the zone radius R_n of the nth zone; the distance z_{prt} away from the focus point or the particle; the wavelength λ_0 of illumination; the interzone distance Δdr and the zone width dr_n of the nth zone

Noticing the circle equation $R^2 = x^2 + y^2$ in the phase term of Equation (2.18) on page 33, the radius R_n of a fringe n may be also represented in accordance to a Fresnel Zone Plate from Equation (2.21) as:

$$R_n = \sqrt{\underbrace{2 \cdot f_{local} \cdot x}_{\text{zone } n} \cdot \lambda_0 \cdot z_{prt}} \quad \Rightarrow \quad \varphi = 2\pi f_{local} x = \frac{k_0}{2 \cdot z_{prt}} R_n^2 \qquad (2.22)$$

which proves the correlation between local fringe frequencies in fringe patterns and zone radii in FZPs. The zone n is simply that frequency bin f_{local} at which the spatial coordinate x is actually located. Solving for the local fringe frequency f_{local} on the left side and inserting into the right side, the result equals the phase information of Equation (2.18).

The **Interzone distance** Δdr in Figure 2.9 is the separation distance between two successive zones of the same parity (even to even or odd to odd). In optics there is no immediate benefit and thus not documented in literature. However, as will be shown later in section 4.1.1 Customized Hough Transform it aids the determination of filter cutoff frequencies in DSP. It can be roughly estimated as the total width of two directly adjacent zones (opposite parity), making use of the FZP once again:

$$\Delta dr \simeq \sum_{m=n}^{n+1} dr_m = \sum_{m=n}^{n+1} \frac{\sqrt{m \cdot \lambda_0 \cdot z_{prt}}}{2m} \tag{2.23}$$

with

$$dr_n = \frac{R_n}{2n} \tag{2.24}$$

Thereby, the width dr_n of the nth zone can be understood as the variation over the radius R_n and is the derivative of R_n with respect to n (Arndt, 2016) - see also in Appendix A.2.1.

The **zone plate resolution** Δr_{res} is the outermost zone width and not only represents the smallest detail of a zone plate (Attwood and Sakdinawat, 2017; Center for X-Ray Optics, 2014) but also determines the spatial resolution limit of zone plate lenses. With regard to particles and their fringe patterns, the resolution Δr_{res} equals the particle size d_{prt} (Poon and Liu, 2014). However, the determination of zone widths in the range of a few sample points is difficult[9]. The zone plate resolution is the difference of the two outermost zone radii:

$$\Delta r_{res} \equiv R_N - R_{N-1} \tag{2.25}$$

or

$$\Delta r_{res} \simeq \frac{\lambda_0 \cdot z_{prt}}{2R_N} \tag{2.26}$$

---

[9]Particle sizes in the lower μm- range will be similar to the camera's pixel size.

where N is the total number of zones. Equation (2.26) provides a convenient representation to highlight two parameters that are crucial for the recording of fringe patterns. Firstly, the smallest zone width Δr_{res} is the smallest detail of a fringe pattern that a detector should be capable to resolve.

Secondly, the **size** D of a zone plate only depends on the wavelength λ_0 and the distance z_{prt} as already found out in Equation (2.18) on page 33. The size of a Fresnel Zone Plate is simply Equation (2.26) reshaped to:

$$D = \frac{\lambda_0 \cdot z_{prt}}{\Delta r_{res}} \tag{2.27}$$

And thirdly, a very crucial opportunity can be drawn from Equation (2.26) or Equation (2.27). When knowing the distance z_{prt} - can be obtained with Equation (2.21) - the size d_{prt} of a particle may be estimated by the size D of the fringe pattern, given that the imaging system allows for perfectly resolved fringe patterns.

2.3.3. Physical Limits of Resolution

Diffraction Limit

Holography is based on the diffraction of light at objects. The resolution limit is therefore generally bound to the limits of diffraction. The Huygens-Fresnel principle is very well explained for single-slit diffraction and may be modified to a circular aperture of the form:

$$t(x,y) = circ(R/r_{prt}) \begin{cases} 1 & \text{for } R \leqslant r_{prt} \\ 0 & \text{for } R > r_{prt} \end{cases} \tag{2.28}$$

where r_{prt} is the radius of the particle, R the actual radial distance from the center of the aperture and $t(x,y)$ the notation of a transparency function.

Unlike in section 2.2.3 Fresnel Diffraction, diffraction by a particle is most often simplified by the far-field condition where $\frac{\pi}{\lambda}[x^2 + y^2]_{max} \ll z_{prt}$ is true. It applies when the maximum extent of a diffraction pattern is much smaller than the distance z_{prt} to the particle. The Fourier Transform of Equation (2.28) gives the solution of the so-called Airy distribution (cf. Vikram, 2005):

$$I(R') = \left[\frac{J_1[\pi \cdot d_{prt} \cdot R'/(\lambda \cdot z_{prt})]}{\pi \cdot d_{prt} \cdot R'/(\lambda \cdot z_{prt})} \right]^2 \tag{2.29}$$

where R' is the radial distance at the detection plane from the center of the object point, J_1 the Bessel function of 1st order and λ the wavelength of illumination. The maximum intensity is at the center of this Airy disc as sketched in Figure 2.10a and rapidly decreases according to the Bessel function in Figure 2.10b.
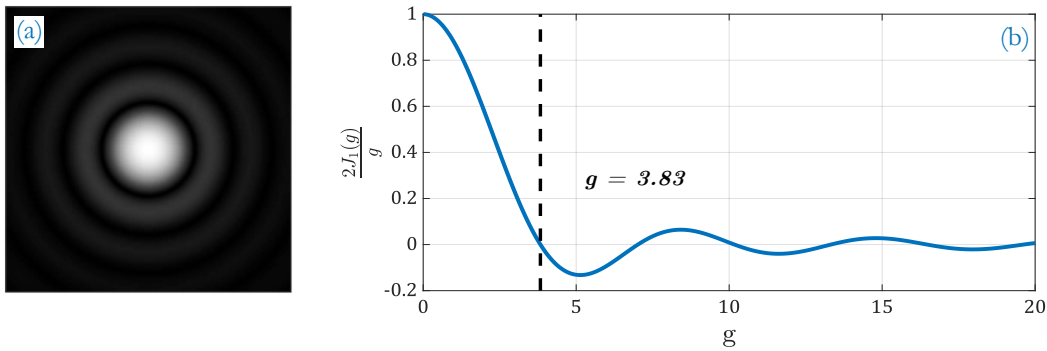
Figure 2.10.: (a) Example of an Airy disc and its intensity decay (b) according to the Bessel function $2 \cdot J_1(g)/g$ of $1^{st} order$. The first minimum at $g \approx 3.83$ correlates to the radius of the center spot.

The Airy disc has a bright center spot which is terminated by the first minimum of the Bessel function at $g \approx 3.83$. In terms of R' it means a minimum image spot diameter of (Vikram, 2005):

$$2R'|_{\text{diffraction spot}} \approx \frac{3.83\lambda \cdot z_{prt}}{\pi r_{prt}} = \frac{1.22\lambda \cdot z_{prt}}{r_{prt}} \tag{2.30}$$

Every object will cause an image spot according to Equation (2.30). Thus, the spot radius equals the minimum separation of two points that can be resolved.

Minimum Particle Size

From Equation (2.30) the smallest particle diameter, an imaging system is able to resolve, can be derived and leads to the Rayleigh resolution limit of (Vikram, 2005):

$$d_{prt} > 2.44 \frac{\lambda \cdot z_{prt}}{x_{cam}} \qquad (2.31)$$

with λ the wavelength of illumination, z_{prt} the particle's distance from the detection plane and x_{cam} the width of the imager (introduced later in section 5.1.2 Sampling Channel). Equation (2.31) is very crucial for the performance characterization of the later realized imaging unit in terms of detection limits.

Multiple Scattering

At high particle densities multiple scattering inevitably increases speckle noise - a granular interference of the scattered waves - which degrades the edge definition of fringes and limits the overall Signal to Noise Ratio (SNR). The SNR is found in Meng et al. (1993) to depend on particle diameter d_{prt}, the particle number concentration C_N and the sample depth z_{ch}. The mean noise intensity $\langle I_N \rangle$ over N particles equals the standard deviation σ_N of speckle noise and may be summarized to the simplified term:

$$\sigma_N = \langle I_N \rangle = C_N \cdot \frac{\pi^3}{48} d_{prt}^2 \cdot z_{ch} \qquad (2.32)$$

Assuming a uniform particle diameter, the noise intensity linearly inreases with the particle number concentration.

3. The Holographic Aerosol Particle Model

The Holographic Aerosol Particle Model (HAPM) is a combination of digital holography modelling based on MATLAB® and a multiphysics simulation using COMSOL®. In this way, a multi-physics sensor model is accomplished to aid as designing tool for the development of a sophisticated holographic detection & counting unit, and building up an understanding of the interrelation of all relevant influences.

This chapter is divided into elaborating the mathematical implementation of digital holography in the first three sections and concludes with Computational Fluid Dynamics & Particle Tracing simulations in section 3.4 Aerosol Modelling.

3.1. Digital Calculations of Diffraction

A recap of diffraction by a particle in Equation (2.12) to point out the starting point:

$$\psi_{prt}(x, y; z) = \mathcal{F}^{-1} \left\{ \mathcal{F}\{\psi_{prt0}(k_x, k_y)\} \cdot \mathcal{H}(k_x, k_y; z) \right\} \tag{3.1}$$

41

where ψ_{prt0} is the initial field distribution at the particle and $\mathcal{H}(k_x, k_y; z)$ the wave propagation term. The equation is the basis for the so called Angular Spectrum Method (ASM). A discretized version of Equation (3.1) is expressed by a Discrete Fourier Transform (DFT) as the following:

$$\psi_{prt}[m,n] = DFT_{2D}\left\{IDFT_{2D}\{\psi_{prt0}[m,n]\} \cdot \mathcal{H}[p,q]\right\} \tag{3.2}$$

where (m,n) are the indices of samples in spatial domain and (p,q) are the indices in Fourier domain.

A system which is sampling and dirscretizing data has two major restrictions: a certain sampling rate f_s and a finite number, say N, of sampled points. For an imaging system this implies an analog signal being sampled at a fixed spatial separation or sampling period Δ_x or Δ_y. With the number of samples N and a sampling period of Δ_x or Δ_y a certain record length L_x or L_y in either spatial direction x or y is obtained as:

$$L_x = N\Delta_x = N/f_s \quad \text{and} \quad L_y = N\Delta_y = N/f_s \tag{3.3}$$

A digital recording medium is not necessarily of equal sampling resolution in x and y, wherefore typically a number of M and N samples are given, respectively. This means for Equation (3.2) that the indices (m,n) are in the range of $-M/2 \leqslant m \leqslant M/2 - 1$ that relate to spatial locations of $-M\Delta_x/2 \leqslant x \leqslant M\Delta_x/2 - 1$, and $-N/2 \leqslant n \leqslant N/2 - 1$ relating to locations of $-N\Delta_y/2 \leqslant y \leqslant N\Delta_y/2 - 1$.

Note:

> Note from Figure 2.6 on page 26 that the $\{x, y\}$ origin is in the center of the particle and also applies to the recording plane and its accompanying Fourier Transform. **i**

The spatial frequency transfer function is now of the form:

$$\mathcal{H}[p,q] = e^{-jk_0 z_{prt}} \sqrt{1 - \frac{(p \cdot \Delta_{kx})^2}{k_0^2} - \frac{(q \cdot \Delta_{ky})^2}{k_0^2}} \tag{3.4}$$

where $k_x = p \cdot \Delta_{kx}$ and $k_y = q \cdot \Delta_{ky}$ are the discretized notations in Fourier domain. The Fourier spectrum is $2\pi f_s$ periodic, which leads to $\Delta_{kx} = 2\pi/M\Delta_x$ and $\Delta_{ky} = 2\pi/N\Delta_y$.

3.2. Basic mathematical model approach

The basic structure of the mathematical model of digital holography is sketched in Figure 3.1a. It is principally composed of the *Object Plane*, describing the particle geometry and the *Detector Plane* which characterizes the detector. The modelling steps are the following:

1. create the particle
2. calculate the wave front, diffracted by the particle
3. calculate the interference of the object wave and the reference wave
4. record the resulting field distribution by the detector.

In terms of the developed Matlab model this translates to the following basic function calls:

```
1  Obj     = initObj(Obj);
2  WaveObj = computeObjectWave(WaveRef , Obj , Det);
3  Holo    = computeHologram(WaveRef , WaveObj);
4  Holo    = computeCCD(Holo , Det);
```

When modelling multiple particles, as drafted in Figure 3.1b, each particle prt_i is treated independently with its own object plane Obj_i allocated in a distance z_{prt_i} away from the detection plane. The total object wave Ψ_{prt} arriving at the detection plane is complex and obtained by the sum of the diffracted patterns (Gire et al., 2008) of all single particles N_{prt}:

$$\Psi_{prt} = \sum_{i=1}^{N_{prt}} \Psi_{prt_i} \tag{3.5}$$

43
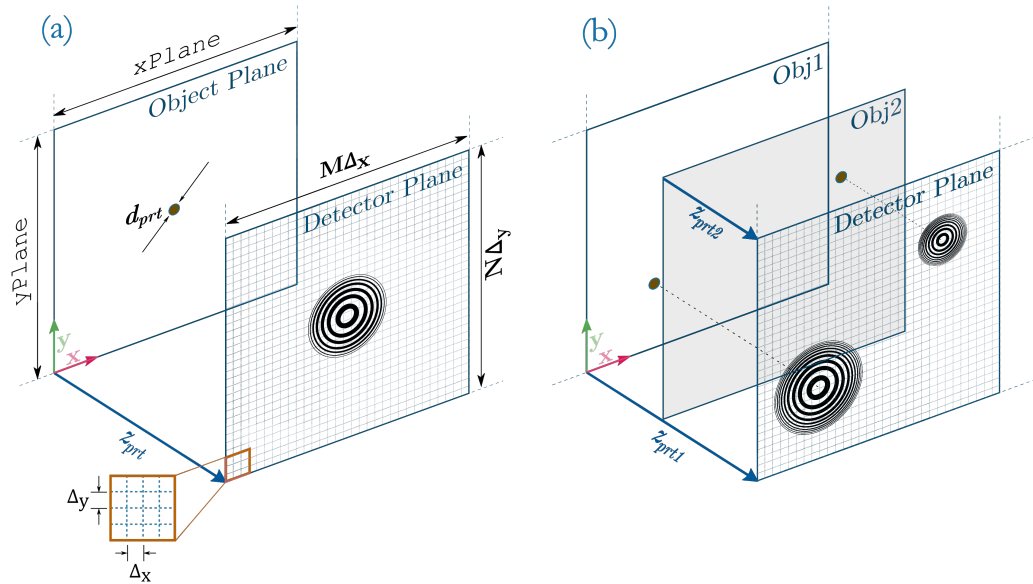
Figure 3.1.: Basic structure of the mathematical model
(a) Creation of a single fringe pattern with the most relevant parameters
(b) Creation of multiple fringe patterns with separate object planes

When dimensioning a particle sampling & imaging system[a] it has to be kept in mind that a certain size distribution of fringe patterns is associated with the Depth of Field (DoF) of the imaging system.

[a]Sampling channels with a greater depth yield a larger size distribution

The drawing in Figure 3.1 also illustrates the variation of fringe pattern extents due to the distance z_{prt_i}, known from section 2.3 Fringe Pattern - The Hologram of a Particle.

3.2.1. Object Plane

Particle

The dimensions of the object plane are mostly dependent on the particle size, shape and its desired level of detail. The particle, as shown in section 2.2 Fundamentals of Holography, is considered an ideal sphere without phase determining properties and is modelled by a circular aperture of diameter d_{prt}.

Size

The $\{x, y\}$- extent of the plane in Figure 3.1 is annotated with xPlane & yPlane and, for the sake of simplicity, equals the extent of the detection plane at first. The field distribution $\Psi_{prt}(x, y; z_{prt})$ of the diffracted wave will be first calculated under the terms of the object plane and eventually projected to the detection plane.

3.2.2. Detection Plane

At the detection plane the discredization of the camera is simulated and must meet the Nyquist sampling criteria to prevent aliasing effects (see next section). The spatial extent of the diffracted wave along the (m, n) plane is most significant for the creation of the fringe pattern. It determines the required characteristics of the detector which needs to capture the total field distribution, meaning it must be of a certain mimimum size.
In acccordance with Equation (3.3) & Equation (3.4) the extent of the detection plane is of (M, N) samples with a resolution of (Δ_x, Δ_y). Generally, these variables represent the eventual camera specifications where (M, N) is typically the so-called camera resolution - e.g.: 1920 x 1080 *Pixel* for a High Definition (HD) resolution - and (Δ_x, Δ_y) correspond to the pixel size.

Criteria for Sampling

Every sampling system has to meet the Nyquist theorem where a signal is unambiguously sampled at a rate f_s not less than twice the highest occuring signal frequency f_{sig} with $f_s \geqslant 2 \cdot f_{sig}$. From fringe patterns we know from Equation (2.19) on page 34 that the highest frequency component is found with the outermost fringe at the edge of the pattern. In other words, and again in relation to a Fresnel Zone Plate, the extent $D/2$ of a fringe pattern must be sampled by:

$$f_s = 1/\Delta_x \geqslant 2 \cdot \frac{D_x/2}{\lambda_0 \cdot z_{prt}} \tag{3.6}$$

where D_x is the representative extent along the x- direction and Δ_x the according resolution of the sampling system. This representation shows that the resolution of a recording medium Δ_x equals the finest detail Δr_{res} of a Fresnel Zone Plate from page 38. With this finest detail it follows that "the pixel size in digital holography is also the minimum achievable resolved size of a reconstructed image" - the particle.

If the distance z_{prt} from the detector to the particle is smaller than $\Delta_x D_x / \lambda_0$ aliasing occurs because the finest structure cannot be resolved. Hence, the Nyquist criteria stipulates:

$$z_{prt} \geqslant \frac{\Delta_x D_x}{\lambda_0} \tag{3.7}$$

With Particles located at a large distance, the opposite scenario must be borne in mind. From Equation (2.21) it is clear that the extent of patterns increases with increasing distances z_{prt} of particles. At some point, a pattern would exceed the size of a recording medium. The limiting condition is reached at:

$$z_{prt} \leqslant \frac{\sqrt{4\Delta_x^2 - \lambda_0^2}}{2\lambda_0}(M - M')\Delta_x \tag{3.8}$$

where Δ_x is again the resolution of the detector, M the total number of pixels of the detector and M' the particle size in unit of pixels.

> An imaging system has to meet the constraints on Depth of Field, given by the particle distance z_{prt}, to guarantee Aliasing-free imaging. Particles should be within a range of depth of:
>
> $$\frac{\Delta_x D_x}{\lambda_0} \leqslant z_{prt} \leqslant \frac{\sqrt{4\Delta_x^2 - \lambda_0^2}}{2\lambda_0}(M - M')\Delta_x \qquad (3.9)$$

Anti-Aliasing measures for modelling

Equation (3.7) shows that a fringe pattern of extent D_x is adequately described when complying with a minimum distance z_{prt} and at a certain resolution Δ_x of the detector. This means for a mathematical model, a computation plane of the minimum required size $M_{min}\Delta_x \times N_{min}\Delta_y$ is sufficient. Thus, the field distribution of the diffracted wave does not need to be calculated for the whole detection plane which would also imply extra computing costs, especially for a large number of particles.

Figure 3.2 illustrates one proposed model approach:

In Step 1, a fringe pattern is calculated according to section 3.1 Digital Calculations of Diffraction but at a plane of the aforementioned minimum required size. M_{min} and N_{min} are determined before the simulation to comply with Equation (3.9). Its determination is based on Equation (3.8) and is:

> **Example: Model realization for M_{min}**
>
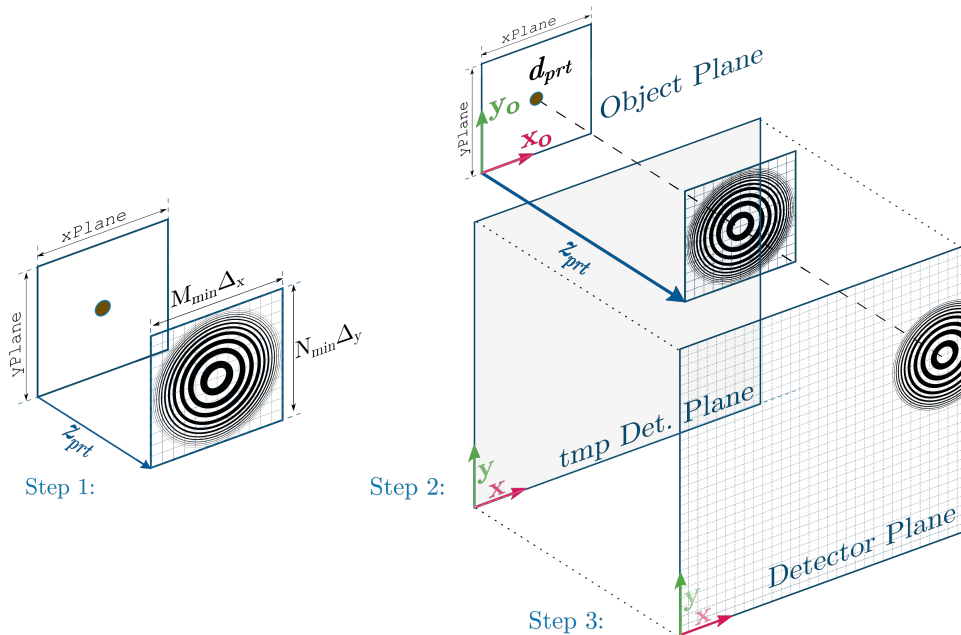> $$M_{min} \geqslant \frac{2\lambda_0 z_{prt}}{\Delta_x \sqrt{4\Delta_x^2 - \lambda_0^2}} + M' \qquad (3.10)$$

Figure 3.2.: Approach for Aliasing-free modelling;
Step 1: generation of a tailored fringe pattern
Step 2: assignment to the intended $\{x, y\}$- location on a temporary plane
Step 3: projection onto the actual Detector Plane

In Step 2, as depicted on the right of Figure 3.2, the truncated fringe pattern is assigned to the intended $\{x, y\}$- location of the particle on a temporary plane. Its initial size matches the actual detector plane but is arbitrarily extended using zero-padding (Poon and Liu, 2014) to include the whole pattern. That procedure is explained in the prevention of simulation aliasing errors - also known as *Border Effects* (Gire et al., 2008).

The detection plane equals a Fourier spectrum with its origin in the center of the plane and a fringe pattern being the frequency information in Fourier space. If now a pattern is generated at the border of a plane and thereby partly exceeding it, the protruding fraction is convolved to the opposite side of the plane as a consequence of spectral folding. Hence, aliasing arises due to a convolution at the detection plane itself.

In Step 3, taking into account the actual Field of View (FoV) of the detector, the temporary plane is projected onto the detection plane. This approach allows an Aliasing-free "imaging" of the simulated diffraction field.

3.3. Transition from static to transient particles

Sor far, particles are considered static and are described by their $\{x, y, z_{prt}\}$-locations and sizes d_{prt}. However, particles are typically passing an imaging unit in a stream of aerosol or fluid and therefore additionally carry properties such as the direction and speed of motion.
In the following section, the impact of moving particles is investigated and embedded into the mathematical model to prepare for the Holographic Aerosol Particle Model which finally simulates aerosol dynamics as prevailing in a certain sampling volume in front of an imager.

3.3.1. Movement of particles

From Equation (2.18) on page 33 we know how a hologram is obtained under ideal conditions. The solution is valid for static particles or an infinite small recording process of $\tau = 0s$. In real world applications, however, recording processes require a finite time interval of $\tau > 0$ and a moving particle will travel a certain distance during that time interval. As the detector is recording, the particle traverses and yields static fringe patterns for every instant in accordance to the changed particle position[1]. When the detector finishes exposure the particle has traveled a distance of Δd_{τ} and the eventual fringe pattern, as a consequence of the superposition of all instances, is blurred by Δd_{τ} (Vikram, 2005). Dixon, Cheong, and Grier (2011) express this incoherent superposition as:

$$I_{\tau}(\mathbf{r}, t) = \int_0^{\tau} I(\mathbf{r}, t + t')dt' \tag{3.11}$$

---

[1] The particle is moving at a speed much lower than speed of light ($v_{prt} \ll c_0$).

with I_τ the intensity distribution of the hologram after recording, $\mathbf{r}$ the position vector of the particle and τ the recording time or exposure time of the detector.

Two scenarios of traveling particles are investigated in the following section:

- a *Longitudinal Movement* along the illumination path
- an *In-Plane Movement* along the plane parallel to the detector

Longitudinal movement

An approach along the z- axis towards the detector or away from it means a longitudinal movement. This implies a modification of fringes and the whole pattern in terms of the holographic principle as:

$$R_n \pm \Delta_\tau R_n \simeq \sqrt{n \cdot \lambda_0 \cdot (z_{prt} \pm \Delta z_\tau)} \tag{3.12}$$
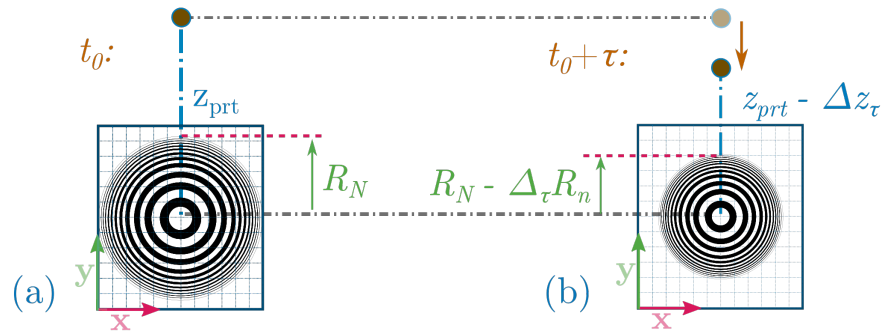

Figure 3.3.: (a) a particle in a distance z_{prt} at an initial time of t_0 yields a fringe pattern of radius R_N
(b) the same particle after recording $t_0 + \tau$ has traveled a distance of Δz_τ and yields an decreased pattern of radius $R_N - \Delta_\tau R_n$ due to the holographic principle

A particle moving a distance of Δz_τ in either direction along the illumination path in Figure 3.3b yields a change of the fringe radii of $R_n \pm \Delta_\tau R_n$. If we now want the finest detail of a pattern - the outermost fringe - be preserved during the recording, we allow in Equation (3.12) a maximum change in the expansion of the pattern by its resolution Δr_{res}.

$$\pm \Delta z_\tau = \frac{(R_N^2 \pm \Delta r_{res}^2)}{N\lambda} - z_{prt} \qquad (3.13)$$

With $\Delta_\tau R_n = \Delta r_{res}$ it means that a longitudinal displacement of $\pm \Delta z_\tau = 1.25/N \cdot z_{prt}$ would be required to affect at least the outermost fringe N of a pattern.

> **Example: practical significance**
>
> If a particle in a distance $z_{prt} = 5\ mm$ away from a detector is recorded at a rather slow exposure time of $\tau = 100\ \mu s$ and a fringe pattern is resolved with $N = 20$ fringes, the particle may approach the detector at a speed of roughly $v_{prt} = 3\ m/s$ and still barely affect the interference pattern.

> A longitudinal displacement - the movement of particles along the illumination path - is uncritical and may be neglected for system design considerations.

In-plane movement

Considering a particle moving along the $\{x, y\}$- plane in y- direction in Figure 3.4b, at the starting point of $\tau = 0$ a fringe pattern is formed according to the conditions of the static case.
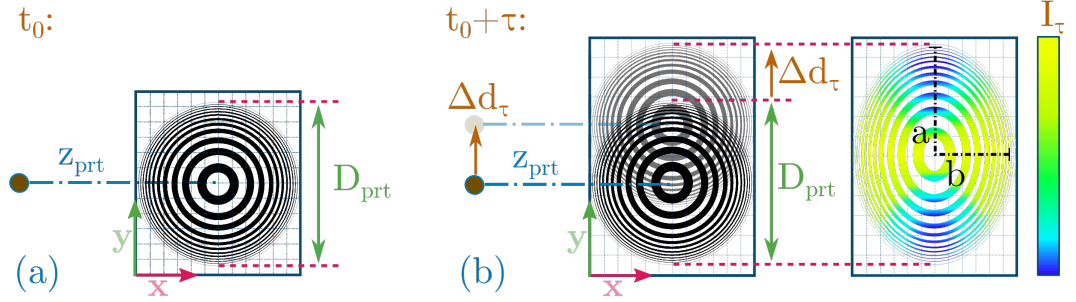
Figure 3.4.: (a) a fringe pattern recorded at an initial time of t_0
(b) while the detector is recording in $t_0 + \tau$, the particle moves a certain distance Δd_τ and fringe patterns are formed at every instant of the particle location. The superposition of all instances yields a motion-blurred fringe pattern with contrast smearing indicated as color map (right plot). The theoretical result is an ellipse with the minor axis b equaling the unaffected radius R_N of the pattern and the semi-major axis a being the elongated axis with $(D_{prt} + \Delta d_\tau)/2$.

A displacement $\Delta d_\tau = v_{prt}(t) \cdot \tau$ in Equation (3.11) entails a motion-blurred modification of the intensity distribution of a static fringe pattern $I(\mathbf{r}, t)$. It can be described by a convolution with the motion vector $\mathbf{v_{prt}}(t)$ of the particle as the following:

$$I_\tau(\mathbf{r}, t|\mathbf{v_{prt}}(t)) = I(\mathbf{r}, t) \left[1 - \frac{v_{prt}(t)}{v_0(\tau)} cos^2 \left(\theta + \frac{\phi(t)}{2}\right)\right] \quad (3.14)$$

A static unblurred fringe pattern $I(\mathbf{r}, t)$ at time t is blurred as a function of the "instantaneous speed $v_{prt}(t)$ of the particle traveling at an angle $\phi(t)$ relative to the x- axis. The degree to which the contrast is diminished depends on the particle's speed $v_{prt}(t)$ relative to a scale $v_0(\tau)$" (Dixon, Cheong, and Grier, 2011).

The degree of blurring is indicated in Figure 3.4b by a vanishing intensity I_τ in the direction of the motion. According to Dixon, Cheong, and Grier, 2011, v_0 may be simply treated as an adjustable parameter because it correlates to an already given exposure time τ.

Although largely elliminated by the effect of contrast smearing, fringe patterns are also uniformly expanded in geometry by the amount of the traveled distance Δd_τ (see Figure 3.11 middle & right). Motion-blurred fringes may therefore be approximated as ellipses with a semi-major axis a being the axis of elongation with $(D_{prt} + \Delta d_\tau)/2$ and a semi-minor axis b equaling the unchanged radius R_N of the whole pattern.
As evident from above and from Equation (2.27) on page 38 the extent of a fringe pattern D_{prt} correlates to the particle distance z_{prt} which concludes the semi-major axis a of the ellipse being also a function of the particle distance. A more meaningful feature of an ellipse is its eccentricity ε as a simple and dimensionless measure for quantification and assessment:

$$\varepsilon = \frac{\sqrt{a^2 - b^2}}{a} = \sqrt{1 - \frac{1}{u^2}} \tag{3.15}$$

where $u = a/b$ is the ratio of the semi-major to the semi-minor axis. It is expanded to take into account the distance correlation of z_{prt} from Equation (2.21) on page 35 and the elongation Δd_τ. In notation of a blurred fringe pattern the ratio u in Equation (3.15) alters to:

$$u = \frac{R_N + \Delta d_\tau/2}{R_N} = 1 + \frac{\Delta d_\tau}{2\sqrt{N \cdot \lambda_0 \cdot z_{prt}}} \tag{3.16}$$

With $\Delta d_\tau = v_{prt} \cdot \tau$ the following conclusions may be drawn from the above solution:

- static particles with $v_{prt} = 0$ yield circular fringes with an eccentricity $\varepsilon = 0$
- the smaller the particle's speed of motion v_{prt} or the exposure time τ, the smaller the eccentricity ε and the effect of motion-blurring
- the larger the particle's distance z_{prt}, the smaller the eccentricity ε and the impact of motion-blurring

> **Example: practical significance**
>
> A fringe pattern is resolved with $N = 20$ fringes and moderately elongated by 10% ($a = 1.1b$). A particle is located in a distance $z_{prt} = 5\,mm$ away from a detector and is recorded at a rather slow exposure time of $\tau = 100\,\mu s$. The particle would have passed the detector at a speed of roughly $v_{prt} = 0.5\,m/s$.

In practice the eccentricity is difficult to determine because of the aforementioned contrast smearing. As a consequence of smearing, the actual extent D_{prt} of fringe patterns cannot be determined any more due to the lack of resolution. Hence, Equation (3.16) becomes inapplicable at stronger motion blurring.

Inner fringes suffer less from smearing because of a higher contrast. Although the elongation effect is much less than for the total pattern, the direction and speed of motion can be estimated. As the eccentricity ε of concentric ellipses is constant, the ratio $u = a/b$ of all elliptical fringes is also constant and Equation (3.16) can be modified to apply to radii R_n of inner fringes:

$$ u = \frac{R_n + \frac{\Delta d_\tau / 2}{u_\odot}}{R_n} = 1 + \frac{\Delta d_\tau}{2u_\odot \sqrt{n \cdot \lambda_0 \cdot z_{prt}}} \qquad (3.17) $$

where $u_\odot = \sqrt{N/n}$ is a scaling factor between the radius R_N of the total fringe pattern and the radius R_n of the nth fringe - cf.: Equation (2.21) which yields $R_N = R_n \cdot \sqrt{N/n}$.

3.3.2. Motion Blurring

The impact of motion-blurring to fringe patterns has already been outlined in the preceding section. More generally speaking and with regard to digital imaging, the appearance of motion blur in images can occur due to a number of reasons.

Object Motion & Camera Shutter

There are two principal reasons for motion blur (Potmesil and Chakravarty, 2005):

- *Movements of objects*: the motion could be: i) of the object with a static camera; ii) of the camera at a static scene or iii) the simultaneous motion of both the camera and the object[2].
- *Movement of the Shutter*: the camera chip is exposed by the movement of a shutter across its photosensitive area. The finite opening and closing time of the shutter, as well as whether a global- or a rolling shutter technology is facilitated, alters the appearance of motion blur in images.

Note:

> Motion-blur due to different shutter techniques will not be covered in this thesis - the selection of a proper technique will be discussed in section 5.3.2 Technology Overview however. **i**

The superposition in Equation (3.11) in section 3.3.1 Movement of particles is also referred to as the recorded image function. According to Potmesil and Chakravarty (2005) the time integral may be converted into a positional integral over an equivalent stationary object because of the velocity as proportional factor. In other words: a faster moving particle means a fringe pattern being spread over a greater image area with reduced intensity. The particle's movement can be described as a uniformly linear motion in a

---

[2]Note: the later described application will be designed with a static camera

certain direction with the following convolution (Gonzalez and Woods, 2001):

$$g(x,y) = \int_0^\tau f[x - x_0(t), y - y_0(t)]dt \qquad (3.18)$$

where $g(x,y)$ is the final motion-blurred fringe pattern, $f(\cdot)$ the intensity distribution incident onto the detector during exposure τ (in fact the acquired image) and $\{x_0(t), y_0(t)\}$ the time-varying components of the particle motion.

> **Example:**
>
> A particle is linearly moving in x- direction only and at a rate of $x_0(t) = \Delta d_\tau \cdot t/\tau$, then after exposure at $t = \tau$ the fringe pattern is displaced by a total distance of Δd_τ.

Filter Transfer Function

When modelling contrast smearing of fringe patterns, a "post-processing step blurs the static fringe patterns by convolving them with the optical system-transfer frunction, derived from the path and velocity of the motion and the exposure time" (Potmesil and Chakravarty, 2005). Practically in DSP, a filter transfer function $H(u,v)$ is formulated to compute the convolution in Fourier domain as:

$$G(u,v) = H(u,v)F(u,v) \qquad (3.19)$$

where $G(u,v)$ is the motion-blurred version of the image $F(u,v)$ to be convolved, both in Fourier domain. Therein, the transfer function of the motion blur is:

$$H(u,v) = \frac{\tau}{\pi(u \cdot d_x + v \cdot d_y)} sin[\pi(u \cdot d_x + v \cdot d_y)]e^{-j\pi(u \cdot d_x + v \cdot d_y)} \qquad (3.20)$$

where d_x and d_y are the $\{x,y\}$- components of the movement Δd_τ.

Model Implementation

```
1 delta_d    = 2*sqrt(lambda * z_prt) * (u - 1) / delta_x;
2 TF         = fspecial('motion', delta_d , theta);
3 motionBlur = imfilter(holo, TF, 'replicate');
```

A modelling approach in Matlab would simply require completing the following steps:

1. calculate the displacement distance `delta_d` given in Equation (3.16)
2. call the function `fspecial` to obtain the filter transfer function `TF` of the motion-blur with the displacement length `delta_d` and the orientation of displacement `theta`
3. convolve the static fringe pattern `holo` with the filter transfer function

For modelling purposes in this thesis it is sufficient to consider only the particle's movement and with a static camera.

3.4. Aerosol Modelling

The existing digital holography model is combined with an expansion, in this thesis referred to as an Aerosol Model, to incorporate further system relevant parameters with respect to a holographic based particle counter. This expansion module is based on a Computational Fluid Dynamics (CFD)-simulation with a particle tracing tool in COMSOL® and contributes particle size distribution, particle number concentration, particle trajectories as well as flow characteristics of the simulated sampling volume.

3.4.1. A proposed Sampling Volume: CFD setup

Figure 3.5a shows the mesh of the total aerosol channel as it is evenutally realized and operated. The bottom funnel-shaped junction of pipe channels comes from the condensation unit of the later used Testing CPC where the developed sampling cell is mounted on top. Its circular output cross section defines the aerosol inlet of the herein designed sampling cell. For simulation purposes, the inclusion of the funnel-shaped junction aids in simulating flow dynamics in the sampling cell based on laminar flow modelling. Therefore, the bottom of the whole mesh is defined as the input to a laminar flow model which also complies with the real conditions in the condensation unit of the Testing CPC. The initial condition of this input is an adjustable flow rate Q_{smpl}.
The output of the sampling cell is again of circular cross section at the top of the mesh. It represents the output of the CFD model, with an initial condition set to standard atmospheric pressure with $p_{out} = 1\,atm$. This setting is reasoned in the fact that the sampling cell in the later evaluation is always operated with open outlet.

The simulation result of Figure 3.5b is the flow velocity field as can be expected at an inlet flow rate of $Q_{smpl} = 0.5\,l/min$. It indicates that the laminar flow is maintained with an average flow velocity of roughly $\bar{v}_{prt} = 0.3\,m/s$ through the straight section of the aerosol channel - the later sampling volume.
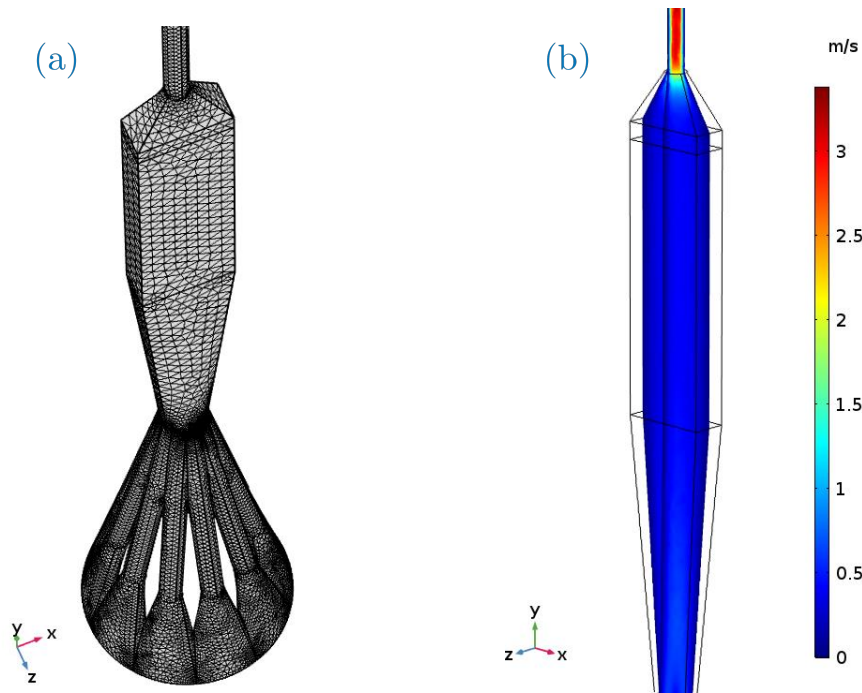
Figure 3.5.: The proposed aerosol channel and CFD-simulation result in COMSOL®.
(a) Mesh of the eventual realized total aerosol channel (including the outlet geometry of the preceeding condensation unit of a CPC)
(b) Flow velocity field in the relevant channel section at $Q_{smpl} = 0.5\,l/min$

With the proposed sampling channel cross section particles can be expected to pass the detector at maximum velocities of around $\hat{v}_{prt} = 0.5\,m/s$ at flow rates of $Q_{smpl} = 0.5\,l/min$.

3.4.2. A proposed Sampling Volume: Particle Tracing

As illustrated in Figure 3.6 the fluid dynamics of the aerosol and the particle movement in an arbitrary channel geometry[3] is simulated. The figure shows particles passing through the eventual realized sampling volume at a flow rate of $Q_{smpl} = 0.5\,l/min$ and a particle number concentration of $C = 40\,\#/ccm$. The sizes, positions and momentary trajectories of all particles are exported to load into the digital holography module of the Holographic Aerosol Particle Model (HAPM).
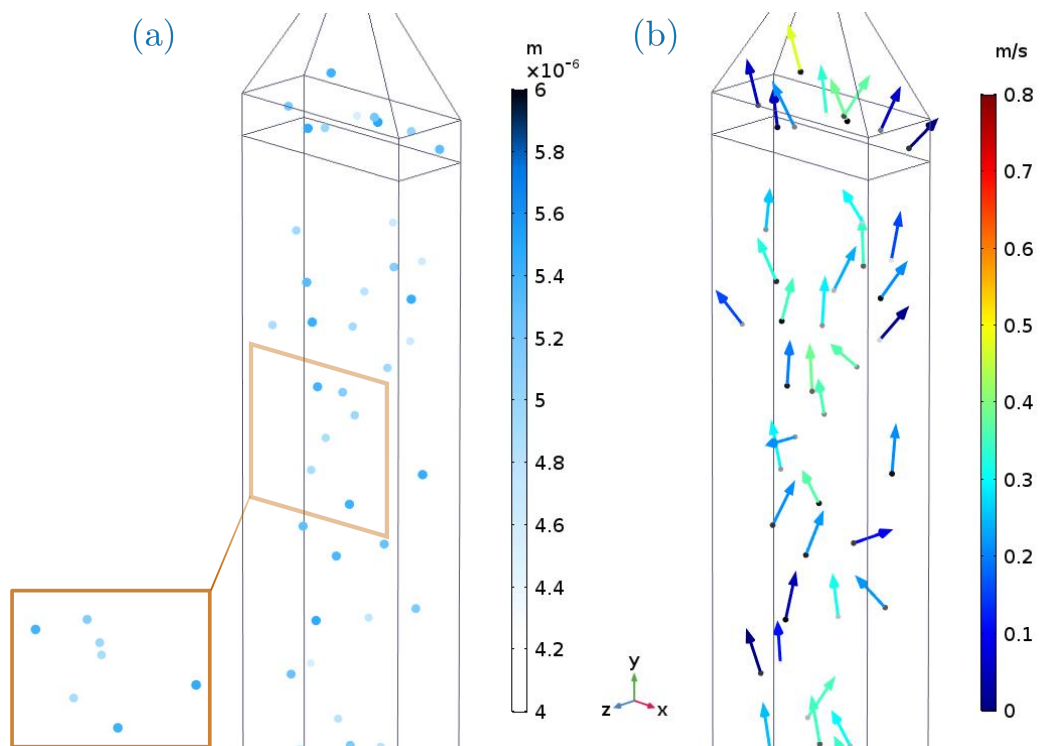

Figure 3.6.: Particle Tracing simulation results of the eventual realized sampling channel.
(a) Particles plotted by their size distribution
(b) Particles plotted with their trajectories

---

[3]Designed in SolidWorks® but principally possible in any CAD- Tool.

On the left are particles plotted by their size distribution[4] in a range of $4 - 6\,\mu m$ as expected from the outlet of the condensation unit of a CPC, on the right are the particle trajectories. The trajectories correlate to the velocity field in Figure 3.5b and also suggest an average particle velocity of around $\bar{v}_{prt} = 0.3\,m/s$ through the proposed sampling cross section.

The marked frame in Figure 3.6a indicates the detector and is situated at the eventual realized location of the sampling cell. Particles in that particular captured volume are fetched to calculate the hologram at the detection plane in Figure 3.7.
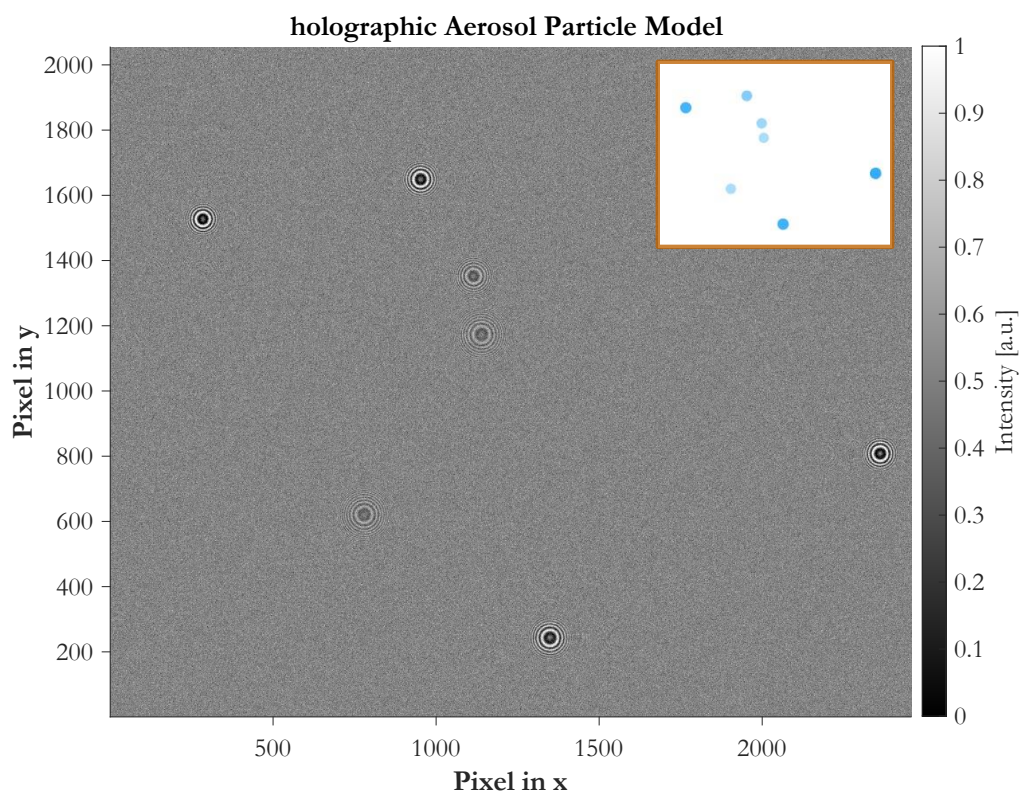

Figure 3.7.: Modelled hologram of the volume captured in the fluid dynamics simulation of Figure 3.6

[4]The particles are magnified by a scaling factor for the sake of illustration.

3.4.3. A proposed Sampling Volume: final result of the HAPM

The fringe patterns in Figure 3.7 exhibit differences in intensity as well as in geometrical expansion. Comparing the hologram with the size distribution sketched in the upper right corner it clearly reveals that larger particles (darker blue) lead to better contrast fringe patterns. For instance, the faint pair of fringe patterns in the center comes from particle sizes of roughly $4.9\,\mu m$ while the particle in the upper left area is $5.4\,\mu m$ in diameter. This particle in particular is also located closer to the detector and hence yields a slightly smaller fringe pattern (here without proof).

3.5. Summary of Functionality

The overall Holographic Aerosol Particle Model as sketched in Figure 3.8 takes into account the following functionalities and physical properties:

Component	Variable	Symbol
Light Source (only coherent)	Wavelength Intensity	λ I
Particles	Spherical shape Size 3D position Direction of motion Speed of motion	 d_{prt} $x_{prt}, y_{prt}, z_{prt}$ ϕ_{prt} v_{prt}
Sample Cell	Arbitray Volume Flow profile	V_{smpl} Q_{smpl}
Detector	Area (size) Pixel size Exposure time Noise	$M \times N$ d_{pxl} τ σ_n

In summary, this chapter clarifies that particles manifest in fringe patterns at a detector plane which carry the full 3D information of all particles in the sampled volume.

The $\{x_{prt}, y_{prt}\}$ coordinates of particles are directly projected onto the detection plane and pose the center of fringe patterns. The extent of patterns is directly linked to the distance z_{prt} of particles from the plane. Particles are modelled as spherical shaped, opaque objects of arbitrary size d_{prt} and motion in an arbitrary sampling volume V_{smpl}. Aerosol-related properties such as particle size distribution, a certain particle number concentration C_N and flow characteristics Q_{smpl} in the sampling volume are provided by a CFD- based expansion module. Flow profiles imply heterogeneous particle movements with various speeds v_{prt} and directions ϕ_{prt} of motion. Particle trajectories have the effect of blurring its corresponding fringe patterns. Speed and direction are mapped onto patterns as a certain elongation in orientation of the particle's movement. For a comprehensive modelling of motions the exposure time τ of an arbitrary imaging unit is taken into account. An imager is described by a photosensitive area $M \times N$, a pixel size d_{pxl} and Gaussian white noise σ_n to adequately simulate captured holograms.

The Holographic Aerosol Particle Model (HAPM) should not only build up an understanding of the interrelation of all relevant influences but also aids the design of sophisticated holographic detection and counting units. Hence, the following chapters are largely supported by the model.
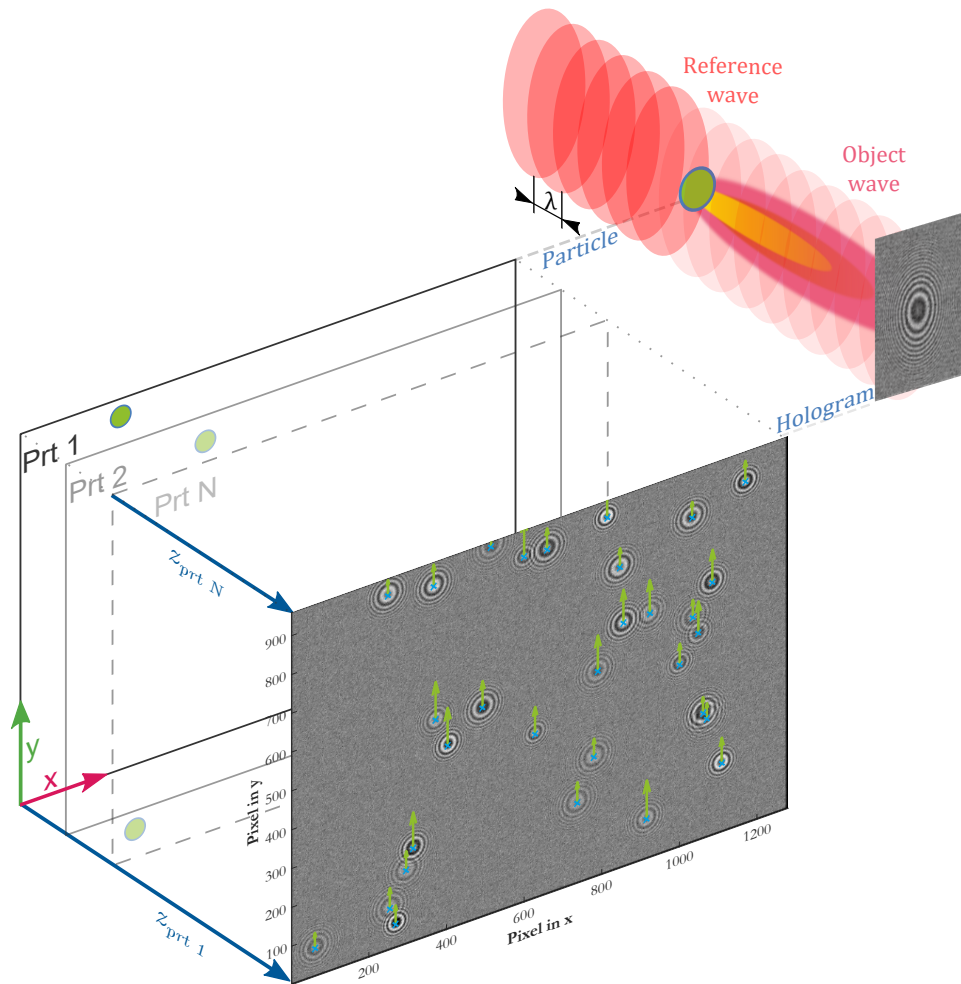
Figure 3.8.: Schematic sketch of the overall HAPM. The hologram of an arbitrary aerosol sampling volume, simulated in CFD software, is modelled to yield the resulting detector image.

4. Particle Detection & Analysis

4.1. Particle Detection Methods

Reasonably from the previous chapters, the detector plane is captured by either line scan- or area scan imagers to obtain images (cf.: 5 The Particle Imaging Unit). In typical Digital Inline Holography applications, 3D reconstruction algorithms are used to numerically reconstruct the particles in the sampled volume (Yu et al., 2014; Pan and Meng, 2001; Gire et al., 2008; Berg et al., 2017; Murata and Yasuda, 2001; Malek et al., 2004). For the sole detection and counting of particles, the recognition of its fringe patterns at the 2-dimensional (2D) detetion plane is sufficient and can be performed with common pattern recognition techniques.
In the following section, three potential pattern recognition techniques are presented. The second section focuses on the analysis of particles and how 3D information can be extracted.

4.1.1. Customized Hough Transform

The Hough Transform (HT) is a very well known feature extraction technique in digital image processing for detecting arbitrary geometrical shapes such as straight lines, circles or ellipses (Duda and Hart, 1972). It makes use of a parameter space - the so called Accumulator or Hough Space - where a voting procedure is carried out over a set of parameterized image objects;

here circles with a certain range of radii. Object edge points, which ultimately form the object's shape, are transformed into that parameter space using its respective mathematical representation. The resulting accumulated feature candidates allow for easier grouping and are therefore robust in the presence of noise, occlusions and varying illuminations.

Working Principle

The implemented customized HT is based on the work of T. J. Atherton and D. J. Kerbyson (1993) and T. Atherton and D. Kerbyson (1999) where the edge filtered image is convolved with a complex filter operator:

$$O_{PCA}(x,y) = \begin{cases} e^{j \cdot \varphi_{xy}} & \text{iff } R_{min}^2 < x^2 + y^2 < R_{max}^2 \\ 0 & \text{otherwise} \end{cases}$$

that forms a Phase Coded Annulus. In this manner, the range of scanned circle radii between R_{min} and R_{max} is phase coded (from 0 to 2π) into a complex accumulator space with the phase-coding across the annulus following a log coding:

$$\varphi_{xy} = 2\pi \left(\frac{log \left[\sqrt{(x^2 + y^2)} \right] - log R_{min}}{log R_{max} - log R_{min}} \right) \tag{4.1}$$

In parameter space, constructive accumulation now occurs only at bins where the transformed candidates intersect with the same phase - the bin which corresponds to the circle's center. Centers are then estimated by detecting such bins as peaks and determining its centroids using geometric moments (see also in section 4.1.2 Blob Labeling and Counting). The sensitivity of that peak detection is in the range of $S_{HT} = \{0..1\}$ and leads to fewer detected circles at lower sensitivity levels.
The radii are estimated by simply decoding the phase information from the estimated center location.

Image Preprocessing

In order to enhance the Signal to Noise Ratio and thus improve fringe visibility of the patterns prior to the edge filtering, a Gaussian smoothing kernel is taken. Since higher order fringes are not mandatory for the recognition of valid patterns, the filter size of the lowpass kernel and ultimately its standard deviation σ_{lp} is configured to filter the unwanted outermost fringes. The cutoff frequency of the filter is determined by making use of one of the most common and heuristic measures when dealing with Gaussian distributions, known as the 3-sigma rule (Kong, Akakin, and Sarma, 2013). The smallest feature in an image unaffected by filtering has to fit within the 3σ or 99% confidence interval. In terms of a fringe pattern, the distance between fringes of the same parity (even to even or odd to odd) may be interpreted as the smallest detail to preserve.
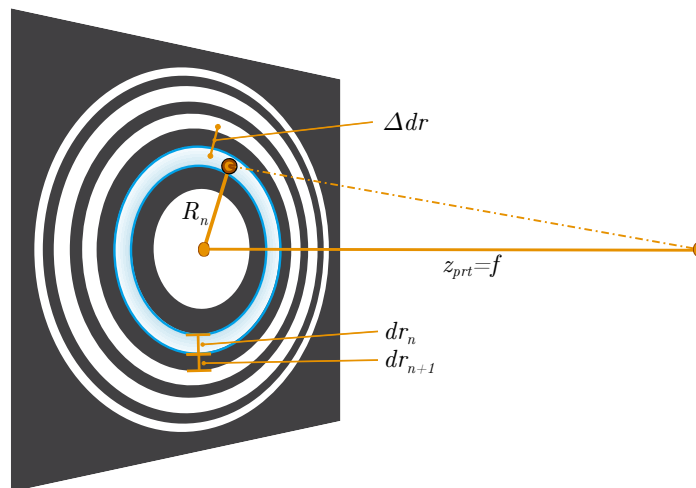
Figure 4.1.: FZP and its most relevant parameters in relation to fringe patterns: the zone radius R_n of the nth zone; the distance z_{prt} away from the focus point or the particle; the interzone distance Δdr and the zone width dr_n of the nth zone

This distance Δdr in Figure 4.1 can be estimated as the total width of two successive zones (opposite parity) by making use of the Fresnel Zone Plate from Arndt (2016) once again:

$$\Delta dr \simeq \sum_{m=n}^{n+1} dr_m = \sum_{m=n}^{n+1} \frac{\sqrt{m \cdot \lambda \cdot z_{prt}}}{2m} \tag{4.2}$$

with

$$dr_n = \frac{R_n}{2n} \tag{4.3}$$

Considering that the 99% confidence interval of a Gaussian filter kernel is its total width with $6\sigma_{lp} + 1$, the filter size of a Gaussian lowpass filter can be calculated by:

$$\sigma_{lp} = \frac{\Delta dr - 1}{6} \tag{4.4}$$

Parameterization

From Equation (2.21) on page 35 it is clear that the radii R_n of fringes are only dependent on their respective fringe index n within the pattern and the distance z_{prt} from the particle (the wavelength λ is constant). The range of possible distances z_{prt} is bounded by the sampling channel (as later outlined in subsection 5.1.2 Sampling Channel). Taking into account that the innermost fringe is principally sufficient for pattern recognition, the range of radii to search may be truncated and greatly speeds up the HT. In this work, a single-step approach is chosen where only the innermost fringe at $n = 2$ is searched with $R_2 = 22 \ldots 33\, pxl$. Due to the geometries of the later discussed sampling cell the innermost fringe may span a range of $R_2 = 23 \ldots 32\, pxl$. A margin of $\pm 1\, pxl$ is added. Analyses showed that especially at high particle densities the overlap of fringe patterns is too strong to identify higher order fringes and its intensities are tendentially to low to be detected. Thus, the Gaussian filter is set to a cutoff of $\sigma_{lp} = 2.62$ to retain an approximate level of detail of $\Delta dr \approx 17\, pxl$. The sensitivity is set to $S_{HT} = 0.93$ and was heuristically determined.

4.1.2. Blob Detection

Blob detection is a subcategory of image matching techniques, aiming at detecting regions of common properties such as a homogeneous brightness or grayscale that thereby distinguish them from background regions (Lindeberg, 1993; Jayanthi and Indu, 2016; Kong, Akakin, and Sarma, 2013; Kaspers, 2009). Blob detectors can be based on image gradients (contrast), eigenvalues or templates (Kaspers, 2009). Since the mathematical representation of fringe patterns is known, template matching (Sonka, Hlavac, and Boyle, 2014) is a suitable approach.

Blob Extraction using Template Matching

An artificially generated fringe pattern of course is a viable template to use. However, since patterns start to overlap strongly at higher particle number concentrations, a mask that emphasizes the sole center zone is more meaningful. A multi-step template matching is performed using circular masks of steadily increasing radii R_m:

$$g_m^{TM}(x,y) = \begin{cases} 1 & \textit{iff } (x - \bar{x})^2 + (y - \bar{y})^2 <= R_m^2 \\ 0 & \text{otherwise} \end{cases}$$

with $(\bar{x}, \bar{y})$ the circle center and m the current step. The templates equal non-normalized disk-like box filter kernels that gradually lowpass-filter background noise with increasing radius of the masks and thereby emphasise regions that match it.

Blob Segmentation

To segment blobs, global thresholding is necessary to find the optimal threshold in the histogram (see Figure 4.2). Although Otsu's method is one of the most widespread thresholding technique due to its good perfomance and yet simplicity, it faces clustering problems with unimodal histograms. Small object areas compared to background areas are the cause for unimodality as reported in Kittler and Illingworth (1985) and Lee and Park (1990).
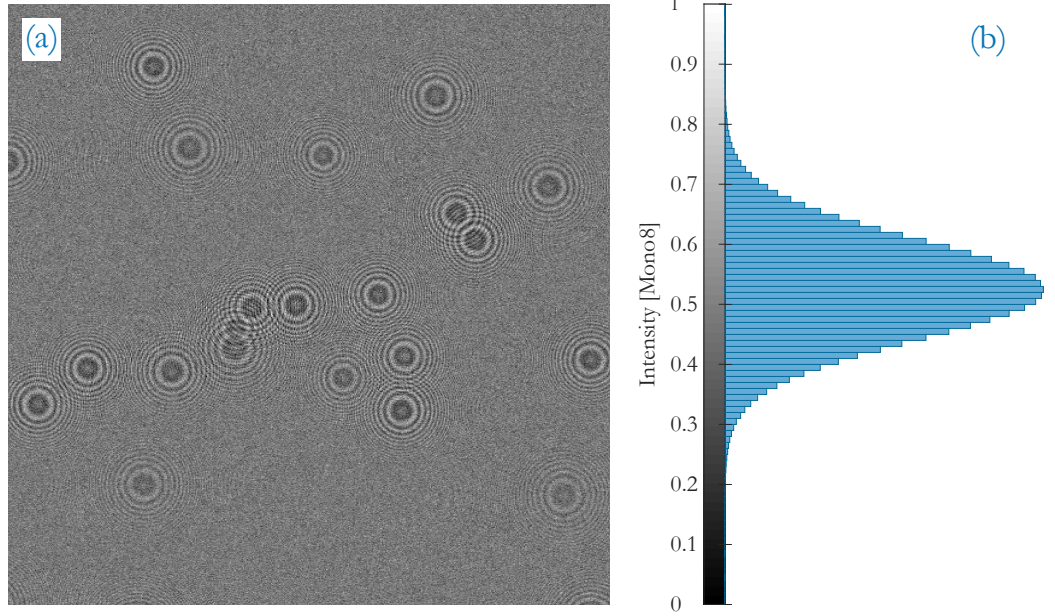
Figure 4.2.: (a) Example of a typical detection plane of low particle number concentration with overlapping fringe patterns and patterns of different extent as a result of the z_{prt}- location in the sampling channel. (b) The normalized intensity histogram.

Unimodality however is the major case in the presented work as apparant from Figure 4.2b and thus disqualifies methods of that kind of clustering thresholding. Instead, with the Maximum Entropy Thresholding of Kapur, Sahoo, and Wong (1985) and Sezgin and Sankur (2004), an entropy-based thresholding method is utilized that interprets the maximum entropy as indicative of maximum information transfer.

It is based on the probability distribution function of gray-level histograms. Assuming two distributions where one belongs to the class of blobs (dark pixels) and the other to the class of background (bright pixels), then the optimum threshold k_{opt} of inter-class entropy is found at:

$$k_{opt} = \underset{L_1 \leqslant k < L_2}{\mathrm{argmax}}[H_{drk}(k) + H_{br}(k)] \qquad (4.5)$$

where H_{drk} is the entropy of dark pixels, based on the probability P_{drk} that pixels are assigned to the class of dark pixels, and H_{br} the entropy of bright pixels with its probability P_{br}, respectively. A lower limit L_1 and an upper limit L_2 confine the threshold k_{opt} to a certain gray-level range for later discussed reasons. The standard setting is $L_1 = 0$ and $L_2 = L$ where L is the number of gray-levels. With a set of $k = \{0, 1, 2, ..., L-1\}$ of L gray-levels, the entropies of both classes are calculated as follows (Kapur, Sahoo, and Wong, 1985):

$$H_{drk}(k) = -\sum_{l=0}^{k} P_{drk}(l) \cdot log[P_{drk}(l)] \tag{4.6}$$

and

$$H_{br}(k) = -\sum_{l=k+1}^{L} P_{br}(l) \cdot log[P_{br}(l)]$$

Blob Labeling and Counting

After thresholding, blobs remain as regions of connected pixels in the binary image and are typically detected by connected components labeling (Haralick and Shapiro, 1985). All connected or neighboring pixels corresponding to a separate region are assigned the same labels. The total number of different labels equals the number of detected blobs and, in the ideal case, also equals the total number of fringe patterns. In fact, fringe patterns may strongly overlap and yield merged blobs. To discover such scenarios blob features are meaningful to assess, using different descriptors.

Regional descriptors are very often used in combination with connected components labeling and are based on mathematical moments of the form (Sonka, Hlavac, and Boyle, 2014):

$$m_{p,q} = \sum_{(x,y) \in \mathcal{R}} x^p y^q \cdot I(x,y) \tag{4.7}$$

where (p,q) are the indices of the moment and (x,y) the pixels of the region $\mathcal{R}$ in gray-scale images $I(x,y)$. The sum $p+q$ of the indices corresponds to the order of the moment $m_{p,q}$. For binary images, as given after thresholding, the term $I(x,y)$ equals 1.

Moments carry physical interpretations of shapes such as the mass (area), center of mass or gravity (centroid), eccentricity or orientation of the region. Therein, the order of moment determines the property. The most common are the zeroth order moment $m_{0,0}$ as the area A and the first order moment as the centroid with $\bar{x} = m_{1,0}/m_{0,0}$ and $\bar{y} = m_{0,1}/m_{0,0}$. The centroid is also a common feature to locate or tag the region at its center point. In the given problem statement it is of particular significance to locate fringe patterns because the centroid of fringes represents the actual location in the xy-plane (cf. in Figure 3.8 or Figure 7.2). In conjunction with the perimeter $P_{\circledcirc}$ (a boundary descriptor), the circularity is another meaningful descriptor (Gonzalez and Woods, 2001):

$$circularity = \frac{4\pi A}{P_{\circledcirc}^2} \tag{4.8}$$

It is a measure independent of size, orientation and translation, and is 1 for a circle. Merged blobs form elongated or asymmetric shapes that deviate strongly from the ideal circularity of 1 and therefore indicate multiple fringe patterns. In this work, it is used as a correction means which adds an additional count to regions where the circularity is beneath a threshold of $circularity \leqslant 0.95$.

4.1.3. Deep Convolutional Neural Networks

> This section was contributed by Isabella Hinterleitner who was involved to develop a detection method based on deep learning.

Convolutional neural networks have made some great advances in visual recognition tasks, e.g. Girshick et al. (2012). While convolutional neural networks have been used for a long time (LeCun et al., 1989), their success was limited due to the size of the available training sets and the size of

the available networks. A breakthrough has been achieved by Krizhevsky, Sutskever, and Hinton (2012) who were able to supervise a training of a large network with 8 layers and millions of parameters on the ImageNet dataset with 1 million training images. Since then, even larger and deeper networks have been trained (Simonyan and Zisserman, 2014).

Working Principle

The network architecture is depicted in Figure 4.3 and is based on the principle of a U-Net structure (Ronneberger, Fischer, and Brox, 2015). In total the network has 23 convolutional layers. It comprises a contracting information path (left path) and an expansive path (right path). The contracting path follows the architecture of a convolutional network and includes the successive application of two 3x3 convolutions, each followed by a Rectified Linear Unit (ReLu) for activation and a 2x2 max pooling operation for downsampling. At each downsampling step the number of feature channels is doubled. Every step in the expansive path consists of an upsampling of the feature map followed by a 2x2 convolution, a concatenation with a correspondingly cropped feature map from the contracting path, and two 3x3 convolutions, followed by a ReLu. Cropping is required due to the loss of boarder pixels at every convolution.

Training

Input images and their corresponding segmentation maps are used to train the network with the stochastic gradient descent implementation of Jia et al. (2014). Due to the unpadded convolutions, the output image is smaller than the input by a constant border width. To minimize overhead and make maximum use of the Graphics Processing Unit (GPU) memory, large inputs are favored over a large batch size. Hence, the batch is reduced to a single image. Accordingly a high momentum (0.99) is used, such that a large number of the previously seen training samples determine the update in the current optimization step.
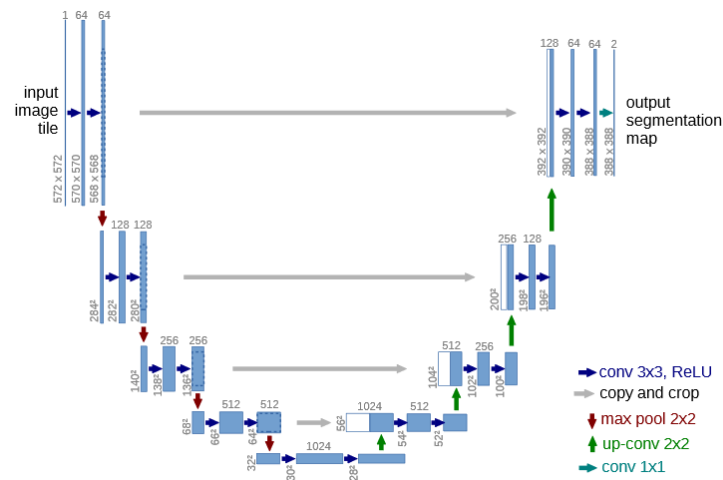
Figure 4.3.: U-Net architecture example for 32x32 pixels in the lowest resolution. Each blue box corresponds to a multi-channel feature map. The number of channels is denoted on top of the box. The xy-size is provided at the lower left edge of the box. White boxes represent copied feature maps. The arrows denote the different operations

Data processing and evaluation

Data augmentation is the main process to teach the network the desired invariance and robustness characteristics where only few training samples are available. In case of fringe patterns, shift and rotation invariance is needed as well as robustness to deformations and gray value variations. The data set is provided by the *Em Segmentation Challenge* 2012 that was started at ISBI 2012 and is still open for new contributions. The training data is a set of 30 frames (512x512 pixels) from the challenge. Each image within this data set is delivered with a corresponding fully annotated ground truth segmentation map for cells (white) and other structures within this challenge (black). In a second step, artificial data generated with the Holographic Aerosol Particle Model was trained. The network is finally trained on real world measurement samples aside from simulated data sets. An evaluation of the U-Net segmentation can be conducted by looking at the model accuracy and model loss for the training and validation set at hand (a data set as e.g. in Figure 4.2).

4.2. Analysis of Particles

4.2.1. Particle Number Concentration

A very crucial measure when dealing with particles is number concentration. The particle number concentration is determined by:

$$C_N = \underbrace{\frac{N_\tau}{Q \cdot \tau_s}}_{\text{flow-based}} = \underbrace{\frac{N}{V_s}}_{\text{volume-based}} \tag{4.9}$$

where its formulation is either flow-based, with N_τ the particle count in a certain sample time interval τ_s, or volume-based, with N the particle count in a given sample volume V_s for visual systems. Standard CPCs use nozzles to separate and individually count the condensed particles. Since the sampling volume is unknown this principle requires to operate the CPC at a constant flow rate Q and knowning the exact sample time interval τ_s to obtain particle number concentrations C_N. In contrast to such flow driven systems an imaging system has the great advantage of inherently providing the concentration. The sample volume is a known quantity, defined by the Field of View of the camera and the Depth of Field which is preset by the sampling channel depth z_{ch} (cf. later in 5.1.2 Sampling Channel).

4.2.2. Particle Localization in 3D

Depth approximation using the Fresnel Zone Plate

The $\{x, y\}$- location of particles is inherently known from holograms. Unless no Holographic Optical Element (HOE) is used to optically map or magnify the wave front, the coordinates of fringe patterns diretly relate to its originating particles.
The z- component is available as the phase information in fringe patterns. As described in 2.3.2 Fringe Pattern vs. Fresnel Zone Plate the particle's distance z_{prt} determines the radii of fringes. With the help of the Fresnel

Zone Plate the z- coordinate of a particle can be approximated by reshaping Equation (2.21) to:

$$z_{prt} \simeq \frac{R_n^2}{n \cdot \lambda_0} \tag{4.10}$$

Reconstruction of the Object Plane

Another way to obtain the particle's full 3D- coordinates is to reconstruct the object plane. This is often called *numerical reconstruction* of wavefronts, *backward propagation* or solving the so called *Inverse Problem* and follow various approaches (Poon and Liu, 2014; Pan and Meng, 2001; Gire et al., 2008; Berg et al., 2017; Murata and Yasuda, 2001; Malek et al., 2004).

Section 2.2.2 Diffraction by a Particle illustrated how the field distribution on the detection plane is obtained by the Angular Spectrum Method according to Poon and Liu (2014). This method is also called the *double Fourier transform method* to implicate that the reconstruction of the object plane is an inverse operation in Fourier space. In order to come to the solution of backward propagation, both sides of Equation (2.12) on page 30 are Fourier transformed and multiplied by the inverse spatial frequency transfer function $\mathcal{H}^{-1}$.

$$\mathcal{F}\{\psi_{prt}(x,y;z) \cdot \mathcal{H}^{-1}(k_x,k_y;z)\} = \Psi_{prt0}(k_x,k_y) \tag{4.11}$$

With $\mathcal{H}^{-1}(k_x,k_y;z) = \mathcal{H}(k_x,k_y;-z)$ the inverse transfer function simply yields the initial field in a negative propagation distance $-z$:

$$\psi_{prt0}(x,y;z) = \mathcal{F}^{-1}\left\{\mathcal{F}\{\psi_{prt}(x,y;z)\} \cdot \mathcal{H}(k_x,k_y;-z)\right\} \tag{4.12}$$

-z= 5.18mm   -z= 5.85mm   -z= 6.51mm
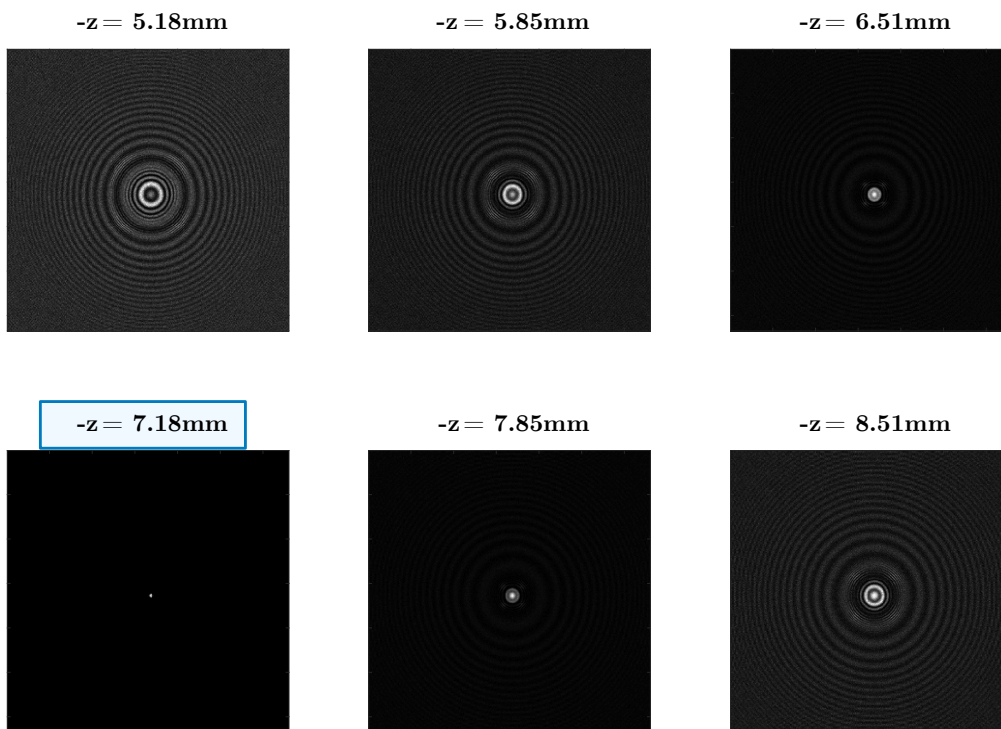
-z= 7.18mm   -z= 7.85mm   -z= 8.51mm

Figure 4.4.: Example of backward propagation to reconstruct the object plane of a modelled particle. The actual z- depth of the particle is found where the intensity distribution is at minimum at $-z = 7.18\,mm$.

A rather simple way to find the actual object plane is to find the minimum of the gray level on the z-axis crossing the particle center (Murata and Yasuda, 2001). Similar to that, finding the minimum of the intensity distribution over the whole $\{x, y\}$- plane may look like Figure 4.4. Only at the origin of the object wave at $-z = 7.18\,mm$, the field distribution becomes zero and the image of the plain particle is left. In practice, however, noise complicates an accurate calculation of the wavefront's origin.

4.2.3. Particle Size

Once the object plane is reconstructed the shape and size of the object can be analyzed by typical 2D image processing means such as image segmentation followed by feature extraction of segmented regions (not elaborated in this thesis - cf. Gonzalez and Woods (2001) and Song et al. (2016)).
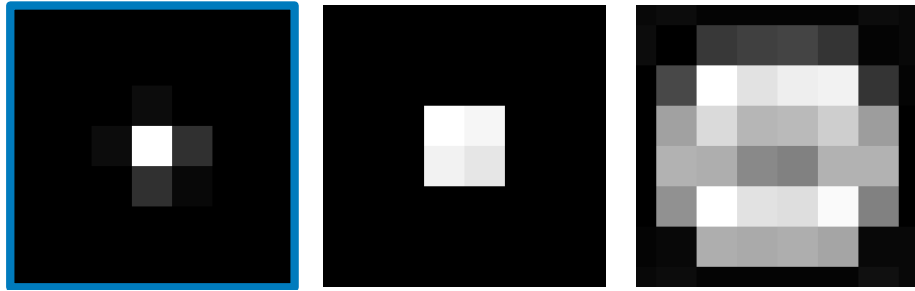

Figure 4.5.: Reconstructed object plane of particles with size: $d_{prt} = \{1, 2, 5\}\, pxl$;
The object plane of the $1\, pxl$ particle belongs to Figure 4.4

Figure 4.5 illustrates 3 modelled particles in a distance of $z_{prt} = 7.18\, mm$ which are reconstructed with Equation (4.12). The assumed distance, as well as the pixel size of the detector with $d_{pxl} = 3.45\, \mu m$ resemble the later available sampling depth and camera, respectively. The particle diameters are multiples of the pixel size with $d_{prt} = 1\, pxl$[1] in the left figure, $d_{prt} = 2\, pxl$ in the middle and $d_{prt} = 5\, pxl$ in the right figure.

This example emphasizes that micro-particles of sizes in the range of pixels or subpixels are difficult to determine accurately. Unfortunately, the expected particle sizes are in that particular range which would require a microscopic alignment using lenses. Super-resolution solutions are provided by e.g. Song et al. (2016) and Verrier and Fournier (2015) which allow the sizing of subpixel objects.

---

[1] A particle of $d_{prt} = 3.45\, \mu m$ also fulfils the criteria of the Rayleigh resolution limit in this example. Later in the experiments, particle sizes in the range of 1-2 pxl are expected.

4.2.4. Particle Trajectories

According to section 3.3.1 Movement of particles the longitudinal displacement of particles along the illumination path is negligible while in-plane movements transfer the information of particle's trajectories to its respective fringe patterns stronger (cf. Figure 3.4 on page 52). With a particle's speed of $v_{prt}(t)$ the pattern is motion-blurred by a displacement of Δd_τ to form a theoretically elliptical pattern.

Displacement of Particles

According to Equation (3.17) on page 54, the traveled distance can be estimated by:

$$\Delta d_\tau \simeq 2u_\odot \cdot \sqrt{n \cdot \lambda_0 \cdot z_{prt}} \cdot \left(\frac{a}{b} - 1\right) \qquad \text{with} \qquad u_\odot = \sqrt{N/n} \qquad (4.13)$$

where the ratio of the ellipse's semi-major to semi-minor axis a/b is constant for all fringes of the pattern. $u_\odot$ is a scaling factor between the radius of the Nth fringe (the radius of the total fringe pattern) and the radius of the nth fringe. From the above equation it is obvious that the particle's distance z_{prt} has to be determined as well - cf. 4.2.2 Particle Localization in 3D.

The direction of motion equals the orientation of the ellipse whereby only a spatial angle of $\pm 90°$ is determinable. Consequently, it is subject to predetermined convention whether a particle is moving in forward or backward direction from a fluidic point of view.

Elongation of Fringe Patterns

Fringes and fringe patterns, like blobs before in 4.1.2 Blob Labeling and Counting, can be considered regions for which mathematical moments are applicable. The detection of blobs is based on the determination of regions' center of gravity $\bar{x} = m_{10}/m_{00}$ and $\bar{y} = m_{01}/m_{00}$ which is a *spatial*

moment of first order. The elongation and orientation of regions is a typical translational invariant property, known as a *central moment* of second order. Central moments are derived from spatial moments by reducing spatial moments from Equation (4.7) with the center of gravity $(\bar{x}, \bar{y})$:

$$\mu_{p,q} = \sum_{(x,y)\in\mathcal{R}}\sum (x - \bar{x})^p (y - \bar{y})^q \cdot I(x,y) \tag{4.14}$$

Second order moments contain three components $\mu_{2,0}, \mu_{0,2}$ and $\mu_{1,1}$ and share terms with the inertial tensor, known from physical mechanics. In analogy to mechanical moments the inertial tensor of the rotation of a region (Haralick and Shapiro, 1985) is built as:

$$J = \begin{bmatrix} \mu_{2,0} & -\mu_{1,1} \\ -\mu_{1,1} & \mu_{0,2} \end{bmatrix} \tag{4.15}$$

The eigenvalues of this 2x2 covariance matrix are the main inertial axes and correspond to the semi-major axis a and semi-minor axis b of an ellipse. Its elongation can be defined as the ratio of the larger to the smaller eigenvalue. The final solution to the axes' lengths is:

$$a = \sqrt{2}\sqrt{\mu_{2,0} + \mu_{0,2} + \sqrt{(\mu_{2,0} - \mu_{0,2})^2 + 4\mu_{1,1}^2}} \tag{4.16}$$

$$b = \sqrt{2}\sqrt{\mu_{2,0} + \mu_{0,2} - \sqrt{(\mu_{2,0} - \mu_{0,2})^2 + 4\mu_{1,1}^2}} \tag{4.17}$$

Eccentricity of Fringe Patterns

As already outlined, the eccentricity ε is a meaningful feature because it is a simple and dimensionless measure for quantification and assessment. Substituting the above solutions of the semi-major axis a and the semi-minor axis b into Equation (3.15) on page 53, the eccentricity can be directly calculated in terms of central moments of second order by:

$$\varepsilon = \frac{(\mu_{2,0} - \mu_{0,2})^2 - 4\mu_{1,1}^2}{\mu_{2,0} + \mu_{0,2}} \tag{4.18}$$

Orientation of Fringe Patterns

The orientation of an object is defined as the tilt angle ϕ between the major axis of the object and the x-axis of the image. In the case of $a \geqslant b$, the tilt angle is summarized to (Haralick and Shapiro, 1985):

$$\phi = \frac{1}{2} \arctan \frac{2\mu_{1,1}}{\mu_{2,0} - \mu_{0,2}} \tag{4.19}$$

4.3. Coincidence & Correction Methods

This section was published in Georg Brunnhofer, Alexander Bergmann, Klug, et al., 2019 and is complemented with definitions valid for all particle detection methods presented in the first section of this chapter.

4.3.1. Time-based versus Area-based Coincidence

In standard CPCs coincidence is a very well known limitation to reach high particle densities. Particles in standard CPCs (as nuclei in droplets) are separated by a nozzle and pass through a light curtain to scatter light. A count event is referred to as an electrical pulse, which a single photosensitive element - commonly a photodiode - is generating from each individual particle scattering occurrence. Typically, a comparator threshold defines when a pulse is valid as a count event. However, because of the small 3D viewing / measurement volume which is optically mapped to the photo detector, there is a finite probability of multiple particles coinciding in that particular volume[2]. The most common implementation to correct for time-based coincidence in such flow-based counting units is the so called *Live Time Correction* (Susanne V. Hering et al., 2005). Therein, the total measurement time is deducted by the *dead time*, in which the system cannot accept any new count event. A statistical correction method based on a Poisson process was proposed by Collins, Dick, and Romay (2013), which focuses on the probability of multiple events occurring in such *per event dead times*.

The realized sampling channel of the later described Particle Imaging Unit can be considered as a large scale expansion of that aforementioned 3D measurement volume. Therefore, in analogy to a *dead time* in the electrical signal of standard counting units, a *dead area* may be introduced in the sense of images - cf. Figure 4.6. Both approaches, *Dead Area Correction* as well as using a Lambert W function as proposed by Collins, Dick, and Romay (2013) are potentially transferable to area-based coincidence problems such as in volume-based counting systems.

---

[2]Actually, this counting principle is a 0- dimensional detection approach since the detection optics is focusing onto the exact location of particles.
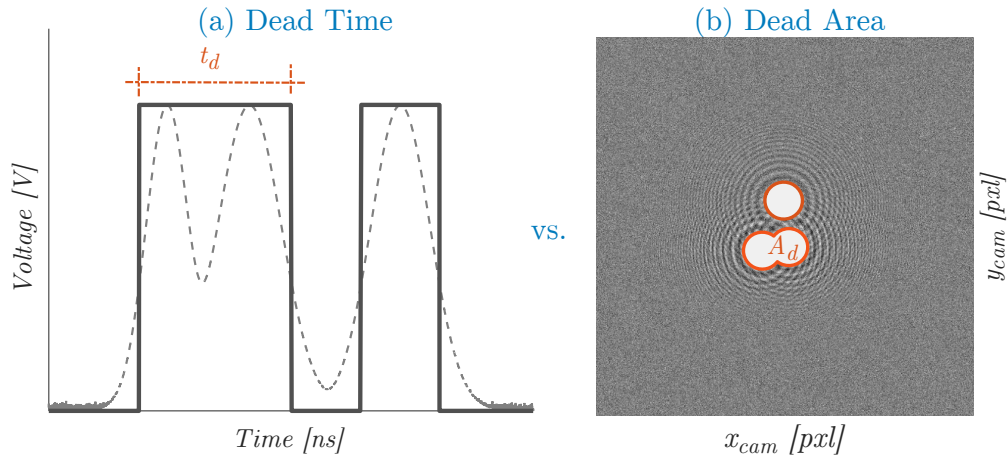
(a) Dead Time

vs.

(b) Dead Area

Figure 4.6.: Occurence of coincidence; (a) as dead time t_d in a certain period of time in flow-based systems (a comparator threshold typically defines a valid count event); (b) as dead area A_d in a certain period of area in volume-based systems

4.3.2. Dead Area Correction

Similar to the definition of *dead time*, where a system is blind to new count events in a certain period of time, an imaging system is blind to new events in a certain period of area, e.g.: the scene behind an imaged object. The imaged object is, thus, considered as the dead area in an image in which the camera is blind for further count events. The image or frame itself is understood as the sample interval.

The common live-time corrected particle number concentration notation as in Susanne V. Hering et al. (2005) may be adapted to:

$$C_a = \frac{N_m}{z_{ch} \cdot (A_{cam} - f_D \cdot A_d)} \qquad (4.20)$$

with C_a the dead area corrected particle number concentration, N_m the measured particle count per frame, z_{ch} the depth of imaged volume, A_{cam} the area which is spanned by the imager, A_d the total dead area and f_D a dead area correction factor. For every fringe pattern a certain *per event*

dead area is defined in which an overlap of one or multiple patterns is not separable by simple image processing means. This area is a fraction at the center of the pattern and will be determined later in this section. As the expansion of fringe patterns depends on the particle's distance along the illumination path, a dead area correction factor f_D takes into account the z- dependency.

4.3.3. Poisson Process – Lambert W function

The rate of particles flowing through a sampling channel occurs at random and, hence, follow a Poisson process. The Poisson distribution describes the probability of a given number of events occurring in a fixed interval of time, distance, area or volume. As particles are mapped to a detector plane, coincidence can be described as the probability of overlapping fringe patterns.
The probability P of x events occurring at a given rate N_a, in a certain area Ω is given by:

$$P(X = x) = \frac{e^{-\mu}\mu^x}{x!} \tag{4.21}$$

$$\mu = N_a\Omega \tag{4.22}$$

In analogy to Collins, Dick, and Romay (2013), the probability that no event occurs in a certain fraction of the detector area, Ω, is:

$$P(X = 0) = e^{-\mu} = e^{-N_a\Omega} \tag{4.23}$$

and leads to the probability that one or multiple fringe patterns would be coincident at the actual count rate N_a:

$$P(X \geqslant 1) = 1 - P(X = 0) = 1 - e^{-N_a\Omega} \tag{4.24}$$

In order to express a relation between the measured count rate N_m and the actual count rate N_a, Equation (4.24) may be solved to:

$$1 - e^{-N_a \Omega} = 1 - \frac{N_m}{N_a} \Rightarrow N_m = N_a e^{-N_a \Omega} \qquad (4.25)$$

$$\text{with} \quad \Omega = \frac{A_d}{A_{cam}} \qquad (4.26)$$

where the occupied detector area Ω is the fraction of the total *Dead Area* A_d over the total detector area A_{cam}. The *per event dead area* is considered as a certain centered part of fringe patterns in which one or multiple overlapping patterns are not separable by simple image processing means.

Since Equation (4.25) cannot be solved analytically, Willink (2010) proposed the so-called Lambert-W function to correct for *Dead Times* in a counting process. The Lambert-W function is defined as:

$$y = W(x) \Leftrightarrow x = y e^y \qquad (4.27)$$

and may be adapted to:

$$N_a \cdot \Omega = -W(N_m \cdot \Omega) \qquad (4.28)$$

where the left and right sides of Equation (4.25) are multiplied by $-\Omega$.

4.3.4. Definition of Dead Area & Practical Approximations

As the spatial extent of patterns originate from particles' positions along the illumination path, a strong variation of pattern sizes occurs while implicating an event-dependent dead area. For simplicity, particles in a sampling channel are assumed to be uniformly distributed. This allows one to work with a mean fringe pattern size as if caused from a particle positioned halfway the sampling channel's depth z_{ch}. The capability of separating

events strongly depends on the applied image processing algorithms and is therefore evaluated individually. Also, fringe patterns are assumed to be circular for which the spanned dead area A_d is followingly determined through the diameter δ_d of a circle.

Hough Transform

The customized HT recognizes patterns by accumulating votes of circle center points and circle radii. When fringe patterns start to overlap, the accumulation points of votes in the Hough space also start to merge and, thus, span a certain dead area in Hough space.
As the recognition of patterns is based on circle extraction, the smallest detectable unit unaffected by overlaps is the innermost circle. Moreover, it is the most pronounced and yields the major contribution to the recognition.

In a first and simplified approach, the innermost circle is approximated as the *per event dead area* because it represents the smallest resolvable fringe pattern indicator. Figure 4.7(a) illustrates the processing result of the customized HT with δ_d the diameter of the innermost detected fringe. Note that fringes are recognized by its outer edge (the edge filter is sensitive to high-to-low gradients).

Blob Detection

Although the functional principle of the blob detection is totally different to the Hough Transform, the spanned dead area is almost identical. Extracted blobs are emphasized center zones of fringe patterns. These blobs are enveloped by the innermost circle but, unlike the Hough Transform which orients towards the outer edge of circles, the inner edge confines the blob area. Therefore, the *per event dead area* spanned by blob detection is slightly smaller. Figure 4.7(b) illustrates the processing result of blob detection with δ_d the diameter of the detected blob.
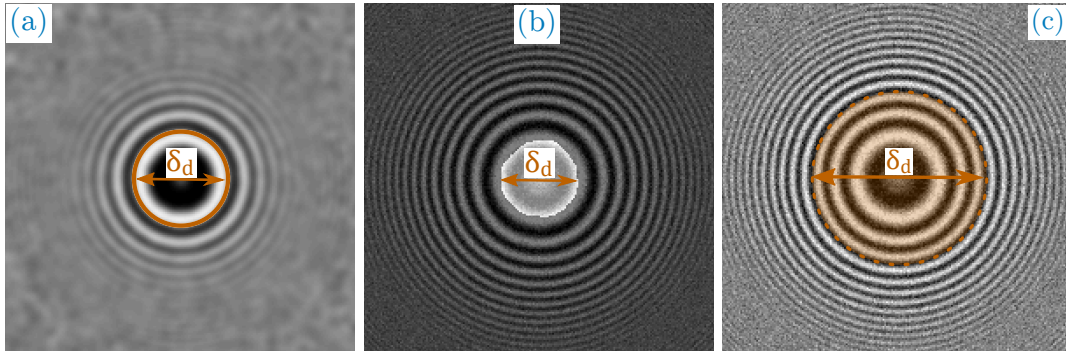
Figure 4.7.: Comparison of Dead Area definitions with the diameter δ_d, nessessary to determine the per event dead area.
The figures show the image-processed results and the individual diameters to each method: (a) customized HT; (b) Blob Detection; (c) Deep Convolutional Neural Networks (DCNN)

Deep Convolutional Neural Networks

The mechanism by which neural networks extract features is a non-trivial task and content of numerous and continuing research. Hence, defining the correct *per event dead area* spanned in a neural network is difficult. In addition, it strongly depends on the network structure, its number of layers and its training sets and conditions.

In anticipation of the later presented counting results, fringe patterns are mostly recognized by three of the innermost fringes[3] as indicated with δ_d and the marked area in Figure 4.7(c). This conclusion can be drawn by reverse engineering the coincidence correction effect in 7.3.2 Dead Area vs. Lambert-W Correction in Area-based Detection. There, an approximate linear response of the coincidence correction curve is achieved with a dead area spanned with $\delta_d = 100\,pxl$. In an average-sized fringe pattern this obtained diamater corresponds to said 3rd fringe.

---

[3]Only valid for lower particle densities - cf: Figure 7.13 on page 147.

In conclusion, it can be assumed that the network is primarily trained on unadulterated patterns where the three innermost fringes are the major contributors to the pattern recognition. The network is obviously trained to be most sensitive to these inner features of patterns whereas seemingly lacking training data to find overlapping occurences as well. In fact, more research needs to done when working with deep neural networks and estimating dead area conditions.

From the perspective of coincidence correction, blob detection is superior in terms of distinguishability of coinciding particles because of the smallest appearing dead areas.

5. The Particle Imaging Unit

As outlined in the introductory chapter, the primary goal is to provide an alternative counting approach for a Standard- CPC. The herein called Particle Imaging Unit (PIU) is therefore intended as an easy-to-replace counting unit and is designed on basis of the earlier described Holographic Aerosol Particle Model (HAPM). The choice of the optical alignment originates from the work of Falk (2014). He investigated the implication of a visual-based particle counting system carried out in dark field or in bright field mode and concluded that the amount of diffracted light in dark field mode is insufficient for detection. Instead, his results suggested a bright light approach and ultimately imply an in-line holographic alignment. Despite a lower SNR, an in-line setup is preferred over an off-axis modification, mostly due to its geometrical simplicity.

While the earlier works of Falk (2014) and Cresnoverh (2015) were a proof of concept, where particles were sampled in open space directly above the outlet of a particle source, the herein presented follow-up work also focuses on the design of a closed sampling cell to provide a well defined sampling volume of interest.

The following described PIU comprises three core components: a laser, a sampling cell and an imager/camera to form an in-line holographic alignment as shown in Figure 5.1.

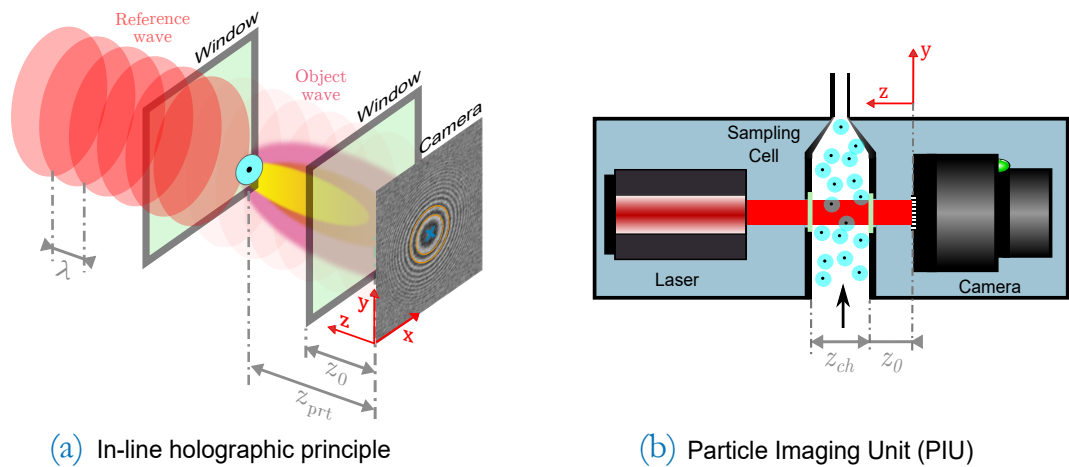(a) In-line holographic principle   (b) Particle Imaging Unit (PIU)

Figure 5.1.: (a) in-line holographic principle where a single particle creates a fringe pattern at the camery plane. The detection is based on recognizing the set of concentric rings (in orange & blue);
(b) schematic of the in-line holographic counting unit, subsequently caller PIU

5.1. Sampling Cell

5.1.1. Requirements

1. With the overal goal of an alternative solution to the counting units of state-of-the-art CPCs, the Particle Imaging Unit sampling cell has to match the outlet geometry of the condensation unit to be attached. These counting units directly follow the condensation section which are commonly prepared to attach a separation nozzle as its mandatory element.

2. The temperature of such counting units are typically held slightly higher than the temperature of the condensation section to prevent the working fluid from condensing on the optical components. This is also crucial for the PIU and its cell windowing. An even more important reason implies a missing nozzle: in nozzle-based units the expansion of droplets is, to some extent, reinforced by adiabatic cooling through

the pressure drop downstream the nozzle. Although the contribution to the final droplet size is negligible, the entailing acceleration of droplets prevents evaporation before their eventual detection. In the proposed nozzle-free imaging approach, droplets are order of magnitudes slower and exhibit a longer travel path at which their size should retain. Conditioning the cell is therefore essential to maintain the supersaturated atmosphere and, thus, sustain the droplet size.

3. The sampling channel, in particular its cross section, has to allow operational aerosol flow rates of CPCs (in particular $0.5 \, l/min$ but typically in the range of $0.3 - 1.5 \, l/min$) while keeping particle velocities in a tolerable range for good quality imaging.

4. The optical axis between laser and camera must be insusceptible to mechanical vibrations and displacements. Dislocations in the range of the camera's pixel pitch already have a big impact on the detectability of the imaging system. While static translations may be compensated through calibration, non-deterministic displacements are intolerable.

5.1.2. Sampling Channel

The geometry of the sampling channel addresses number 3 of the above listed requirements but is the most important for holographic imaging. Figure 5.2 shows the sampling geometry of the Particle Imaging Unit. Its designing is supported by the HAPM where the influence of the channel's cross section is simulated to obtain meaningful holograms in terms of fringe pattern sizes and size distribution as well as motion-blur degradation due to the particles' motion. The eventual dimensioning is subject to the following aspects:

1. a rectangular cross section is favourable due to its coplanarity;
2. the width x_{ch} of the sampling channel specifies the dimension of the imager;
3. the depth z_{ch} of the sampling channel determines the size of fringe patterns at the detection plane;

4. the resulting cross section affects the speed of particles through the channel.
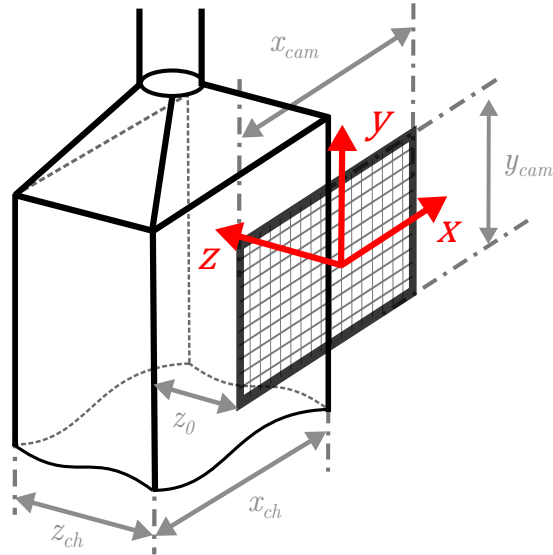

Figure 5.2.: Sampling channel geometry of the PIU

Sampling Channel Cross Section

A volume imaged by a camera is formed by $x_{cam} \times y_{cam} \times z$, with z as the camera's DoF[1]. The imaged volume is the basis for the later determination of particle number concentrations. Therefore, a rectangular cross section $x_{ch} \times z_{ch}$ of the sampling channel is meaningful to have a well defined sampling volume. This fact also reveals the advantage over nozzle-based counting systems as the sampled aerosol volume is known inherently.

Sampling Channel Width x_{ch}

The width x_{ch} of the sampling channel should preferably match the width x_{cam} of the imager to cover the whole sample flow. Since a lens-less imaging

---

[1]Note that an Angle of View (AoV) does not arise as no lens is used and the sensor is illuminated with a collimated beam.

design is desired and hence no camera objective used to extend the Field of View, imager size and channel size are mutually dependent. Nevertheless, smaller camera outlines are possible because of the described volume definition, which is also important for other reasons. This will be addressed later in this document.

Sampling Channel Depth z_{ch}

The depth z_{ch} of the sampling channel also determines the Depth of Field in terms of the holographic principle. The z- axis defines the size of particle's fringe patterns on the detection plane. A strong variation in distances leads to a wide range of fringe pattern expansions. Thus, finding a meaningful range of distances which yield fringe pattern sizes with sufficient pixel resolution to be determinable and not occupying too much of the detection plane is essential for high density particle detection. A larger DoF additionally implies a higher coincidence probability of particles. This is why a small z- extent is favoured. Empirical model tests using the Holographic Aerosol Particle Model suggest dimensions in the lower mm- range.

Speed of Particles

The cross section of the sampling channel affects the particle velocity which is of great importance for high quality imaging. As with faster traveling particles, the associated motion blur (discussed in 3.3.2 Motion Blurring) degrades the contrast and sharpness of imaged fringe patterns. There are generally two ways to regulate the speed of particles:

1. vary the $x_{ch} \times z_{ch}$ cross-section of the sampling channel, preferrably the width x_{ch} (cf. 5.1.2 Sampling Channel Width x_{ch})
2. adjust the flow rate through the sampling cell

From the simulation results in section 3.4.1 A proposed Sampling Volume: CFD setup a maximum particle velocity of $0.5\,m/s$ can be expected at a flow rate of $Q_{smpl} = 0.5\,l/min$ through the therein proposed sampling volume. This assumed flow rate is typical for the target CPC and, therefore, basis for the sampling cell design.

Final Dimensions

In conclusion, the dimensioning of the sampling channel is a compromise between the optimal aerosol flow rate, available imagers (size, pixel pitch, exposure time) or imaging optics, and a meaningful distribution of fringe pattern expansions on the detection plane to achieve high detectable particle densities.

> The best compromise is found with a sampling channel cross-section of $x_{ch} \times z_{ch} = 10 \times 4\,mm$.

As will be seen in later experiments, it allows flow rates of up to roughly $Q_{smpl} = 1\,l/min$ and still yielding tolerable fringe pattern contrasts. The size distribution of fringe patterns is also in a good range for easy detection and processing by image processing algorithms. Furthermore, several camera chips are available that not only fit the channel width x_{ch} (as explained in section 5.1.2 Sampling Channel Width x_{ch}) but also satisfy the requirements of appropriate exposure time and pixel pitch.
The width of $x_{ch} = 10\,mm$ is selected on basis of the later described imager size. The imager rates a width of $8.5\,mm$. A small margin is included to avoid possible diffraction artefacts caused by the sampling cell walls in the Field of View of the imager. An optical depth of $z_{ch} = 4\,mm$ in the sampling cell is chosen and founded in empirical model tests using the Holographic Aerosol Particle Model. The tests resulted in fringe pattern sizes in an approximate range of $20 - 70\,pxl$ which are satisfactory for robust pattern recognition.

5.1.3. Cell windowing

As previously mentioned, the imaging unit is realized in an in-line holographic arrangement without imaging lenses. In order to facilitate a closed

sampling cell, insertion frames equipped with proper windowing are inserted on both sides of the illumination path. N-BK7 broadband windows with a diameter of 1/2″ are used in the given setup and, thus, determine the illumination cross section in the sampling channel. The general idea of insertion slots is to enable the possibility of easy exchange of different optical elements such as windows or lenses.

5.1.4. Fabrication

To satisfy the requirements listed in subsection 5.1.1 Requirements, the sampling cell is a 3D- printed part made of AlSi10Mg, which is one of the standard alloys for Selective Laser Melting (SLM). It combines high specific strength with good thermal conductivity at a low coefficient of thermal expansion ("AlSi10Mg-0403 powder for additive manufacturing" 2015). The latter is especially important as temperature fluctuations would lead to a noticeable misalignment of the optical path.
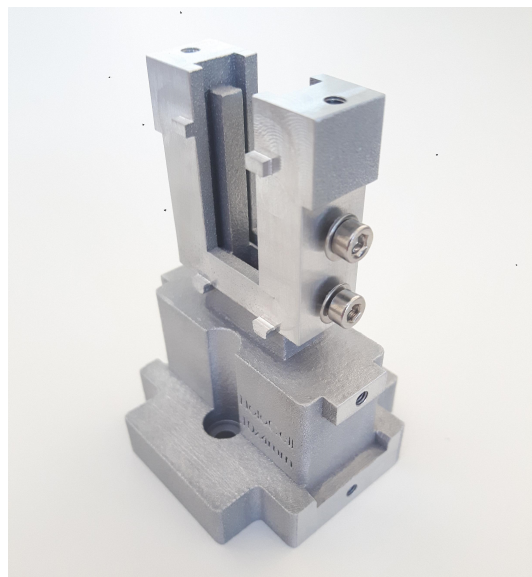

Figure 5.3.: 3D-printed HoloCell made of AlSi10Mg

In terms of thermal expansion, the sampling cell and the window insertion frames are matching components.
Where high thermal conductivity is of less significance or even unwanted, assembly parts are manufactured with an in-house Onyx 3D-printer.

5.2. Laser

As evident from the Rayleigh criteria in Equation (2.31) on page 40 the wavelength of the light source determines the minimum resolvable size of particles. Furthermore, it also contributes to the size of fringe patterns on the detection plane according to the characteristics of a Fresnel Zone Plate in Equation (2.27) on page 38.

5.2.1. Requirements

In addition to the aforementioned aspects, the following requirements should be met:

1. Because of the in-line arrangement of the Particle Imaging Unit, the required optical output power[2] is low since the light source directly illuminates the detector. The light source should provide high enough illumination level while not saturating the detector in order to acquire good quality images. The wavelength should of course correlate to the spectral range of the detector.

2. The light beam should be temporally coherent along the illumination path to obtain high contrast holograms. The coherence length should thus be larger than the distance from the particles to the detector to ensure interference among the reference wave and the diffracted waves. A shorter coherence length would mean partial coherence that inevitably degrades the degree of interference and the contrast of

---

[2]Permanent light sources and of-the-shelf imagers are considered in the first place. Shorter acquisition times may be achieved with pulsed light sources which means higher illumination power. This is crucial to enable high speed sampling applications.

holograms. The quality of wavefront reconstruction largely depends on the degree of coherence.

3. The intensity distribution of the beam should be as flat as possible to illuminate the sampling volume of interest as homogeneous as possible. Furthermore, spatial coherence across the beam cross-section would yield homogenous hologram contrasts over the entire detection plane. A compromise between these typically contradicting properties should be found. The beam should also be of low noise and stable over time to avoid fluctuations in the imaging.

4. The opportunity of light modulation is beneficial if the detector is not well suited for continuous-light applications. The modulation can be used as a flasher function and also counteract motion-blur effects as described in section 3.3.2 Motion Blurring.

5.2.2. Selection

The choice of the appropriate light source also origantes from the work of Falk (2014) and his selected laser is taken on. He worked with a low-noise diode laser which is designed for the application of laser diffraction measurements. Figure 5.4 illustrates in annotation 1 the flat intensity distribution of the output beam cross section which is formed by the slit-shaped aperture of annotation 2. As the dimension of the slit is too small to illuminate the entire sampling cell of the Particle Imaging Unit the laser is operated with removed aperture. The beam exhibits almost constant lighting intensity along its cross section, while the beam flatness is slightly decreasing towards the edge to avoid self-diffraction. This avoidance in self-diffraction is essential and, together with a slightly smaller detection area than the sampling volume, this restriction in active sampling volume proved appropriate.

High beam flatness is generally contradicting to spatial coherence since the intensity distribution of spatially coherent waves is typically Gaussian shaped. This reduced spatial coherence and a reduced temporal coherence length ($< 300 \mu m$) pose a major drawback and essentially allows for only partial coherence holography which lowers hologram contrast. However,

this is acceptable as the later presented results will reveal. The low noise operation and good beam flatness while facilitating a compact design mostly outweigh this disadvantage.

Nevertheless, further research on partial coherence holography should be addressed in follow-up research where also spatial coherence should be of research focus to improve hologram contrasts.
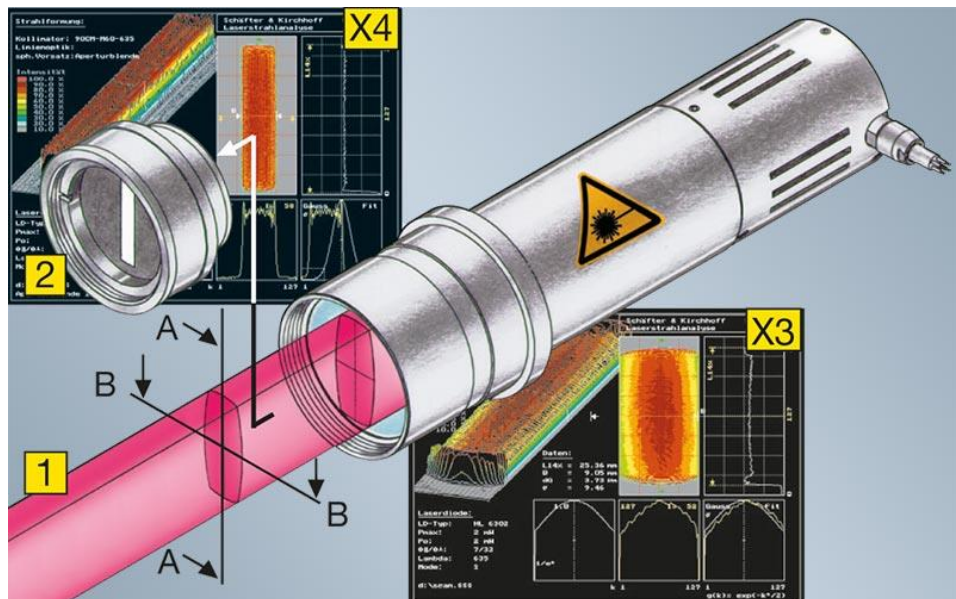

Figure 5.4.: Datasheet figure of the selected Diode Laser from Schäfter+Kirchhoff (Source: Schäfter + Kirchhoff GmbH, 2014)

The wavelength of $\lambda = 635nm$ complies with the optimum range of quantum efficiency of typical monochromatic and color camera chips. This is essential for good quality imaging due to better SNR[3].

The laser is primarily operated in continuous light mode where the sampling cell is permanently illuminated and the duration of sampling - hence the exposure time - is determined by the camera. However, an external modulation of the laser also enables the ability to specify an overall system exposure, composed of the laser modulation rate and the exposure time of the camera. With a modulation frequency of $f_{mod} = 100kHz$ an exposure

---

[3]The best match is achieved by using green light though, as most cameras are optimzed to the perception of the human eye which is most sensitive to the green spectrum.

time down to $10\mu s$ may achieved with the laser. This hybrid mode of operation is also known as *stroboscopic imaging* and will be made use of in section 6.4 Variation of Aerosol Flow Rate & the stroboscopic Imaging.

In summary, the selected laser - a **LNC-91CM-M60-635-1-H02-H-6 Low Noise Laser Diode Module** from Schäfter & Kirchhoff - features the following properties:

Performance Characteristic	Value
Low Noise	$< 0.1\%$ RMS @ $1MHz$
Reduced coherence length	$< 300\,\mu m$
Beam divergence	$0.03\,mrad$
Wavelength	$\lambda = 635nm$
Output optical power	$P_{out} = 1mW$, adjustable from 1 to 100%
External modulation	TTL up to $f_{mod} = 100kHz$
Laser class	3B

5.2.3. Mounting

Because of multiple integrated optical stages, the laser is manufactured in an elongated housing (symbolically drafted in Figure 5.4). A direct mounting to the sampling cell using a single joint is therefore not feasible. Instead, the laser is attached to the cell by a 3D- printed mounting bracket and supported with optomechanical elements from THORLABS at the back side of the laser (see later in Figure 6.1 on page 112).

5.3. Imager

The choice of an appropriate imager/camera is subject to various criteria and in strong interrelationship with the illumination conditions as well as

the dynamic range, exposure procedure and resolution of the imager. Also, the dimensions of the sampling channel have to be taken into account and whether imaging optics need be used.

First of all, a decision on the type of camera needs to be made. The types are generally categorized into the following two (Stemmer Imaging AG, 2020):

1. *Line scan camera*: It consists of a single linear array of light sensitive pixels and builds up images one line at a time. This type of camera is used in imaging applications of linear motion, extremely high resolution of speed or to scan broad objects such as at the inspection of continuous material, cylindrical or rotating objects.
2. *Area scan camera*: It consists of a sensor that occupies an area rather than a single line of light sensitive pixels. The produced image is two dimensional. Its applications are numerous and of course well known in the current era of photography and digital media.

The use of an area scan camera is preferred over a line scan camera as it is technically less demanding and because of the paramount availability of different machine vision solutions. Additionally, the imaging span or area of interest is rather small, a linear motion of particles is not necessarily given and the requirement of high resolution of speed is not important at this stage of research.

5.3.1. Requirements

The selection of an appropriate imager model is also based on the HAPM of chapter 3 and addresses the following requirements:

1. The imager, as exposed to bright light conditions, should provide a high dynamic range to resolve small differences in intensity of fringe patterns while allowing high lighting levels of the sampling channel.
2. The pixel pitch should be as small as possible to resolve single particles, ideally with no need for additional optical means.
3. The imager size should preferably cover the volume of the entire sampling channel - cf. Figure 5.2.

4. The exposure time[4] should allow good quality imaging by keeping motion blur caused by moving particles within reasonable limits.

5.3.2. Technology Overview

> A thorough overview summarized in this section is found at Stemmer Imaging AG (2016). *CCD or CMOS : can CMOS sensors replace CCDs in all cases ?* Tech. rep. URL: https://www.stemmer-imaging.com/media/uploads/cameras/avt/de/de-Allied-Vision-WhitePaper-CCD-vs-CMOS-0416-KAVTO115-201604.pdf; Stemmer Imaging AG (2020). *Cameras*. URL: https://www.stemmer-imaging.com/en-at/knowledge-base/cameras/?choose-site=active (visited on 01/03/2020).

The fundamental question to target in a second step is the choice of sensor technology - Complementary Metal-Oxide-Semiconductor (CMOS) versus Charge Coupled Device (CCD). The first requirement in 5.3.1 Requirements addresses that selection.
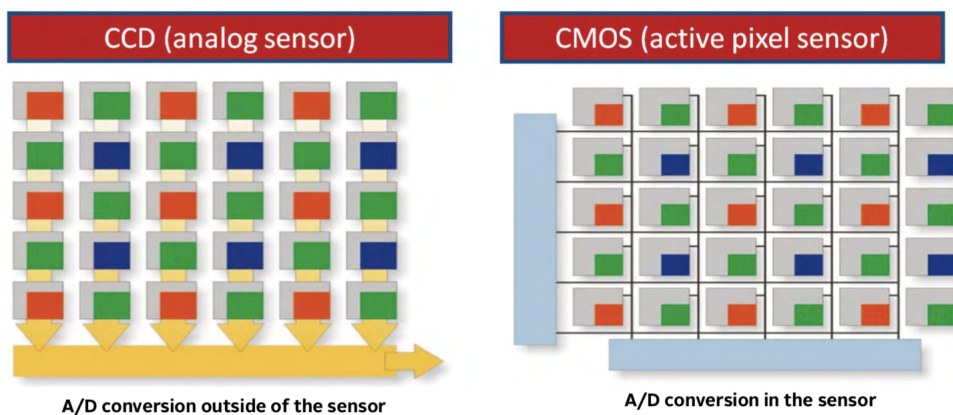

Figure 5.5.: Technology principle of CCD and CMOS sensors (Source: AG (2016))

---

[4]A permanent light source is considered in the first place. Thus, the imager determines the overall system exposure time.

Charge Coupled Device (CCD)

An essential feature of CCDs is the concurrent illumination of all pixels. This implies a perfect global shutter functionality which is thus well suited for applications requiring very short exposure times. The accumulated charge of pixels is read out horizontally or vertically by transporting the charge from pixel to pixel. This procedure limits the readout speed and is disadvantageous for that technology. "The serial charge-to-voltage conversion of all pixels takes place outside the sensor in the camera's electronics". The amount of charge is proportional to the intensity of incident light and the exposure time. Further benefits are high pixel homogeneity, high sensitivity as well as good signal quality in low light conditions.

Complementary Metal-Oxide-Semiconductor (CMOS)

"In contrast to CCDs, the charge-to-voltage conversion occurs in every pixel of the sensor which enables a faster readout. The digital information is directly converted on the sensor chip. However, this requires an elevated design complexity". Modern CMOS sensors with a Global Shutter are available in different resolutions, are capable of adjustable Region of Interest (RoI) readout and allow high frame rates.

Most relevant Terms

Frame rate: is the number of individually captured images/frames per second - Unit: $[fps]$

Full-well capacity: is the maximum electrical charge a pixel can carry. The greater the full-well capacity the greater the dynamic range. Larger pixels allow more photon-to-electron conversions and have larger well capacities - Unit: $[\%]$

Quantum efficiency: "is the percentage of photons of a specific wavelength that are converted into electrons" - Unit: $[\%]$

Background noise: is the signal measured without light hitting the sensor.

Light sensitivity: is also often referred to as responsivity and is the generated output voltage as a function of the incoming light intensity. The main influencing parameters are the quantum efficiency and the background noise. If the amount of light is limited or the exposure time is short a good sensitivity is required - Unit: often in $[V/(nJ/cm^2)]$

Dynamic range: "is the ratio between the smallest and largest amplitude of a signal a sensor chip can produce". A higher dynamic range means small differences in intensity over a wide range of intensities and thus yield better contrast in images - Unit: often in $[dB]$

Signal to Noise Ratio: "describes the ratio between the maximum signal and the noise floor" and thus, in contrast to the dynamic range, takes the noise component into account - Unit: $[dB]$

Blooming effect: occurs when the incident light exceeds the capacity of a pixel and charges impinge into neighboring pixels. This is recognized in images as bright spot at the over-exposed pixel region.

Smearing effect: occurs in Charge Coupled Devices after the actual exposure. Additional charge carriers are produced during charge transport from pixel to pixel. This is recognized in images as white stripes leaving a bright spot. The direction of the stripes originate from the direction of the readout procedure.

Shutter: admits the correct amount of light to the sensor chip and hence controls the exposure time. In general, shutters are divided into two types:

1. Global shutter: all pixels are exposed concurrently (CCDs are technologically based on global shutters).
2. Rolling shutter: the start and end of exposure on each row or column happens sequentially. Rolling shutters may cause motion-blur as mentioned in section 3.3.2 Motion Blurring.

Region of Interest: is a certain part of an image which is adjustable on sensor level and can be as small as one pixel. Due to technology reasons where pixels have to be read out in parallel only CMOS sensors provide this functionality. Reducing the size of the image reduces the required transmission bandwidth or increases the imaging frequency / frame rate.

CCD versus CMOS: Comparison and Technology Selection

The following table compares the most relevant properties:

	CCD	CMOS
Frame rate	considerably slower due to line-by-line readout	considerably faster; further increased by adjustable RoI.
Pixel size & pixel density	smaller sizes possible (but reduced SNR); low - high	size dependent on packaging and shutter technology; low - high
Light sensitivity	formerly: superior and thus used under low-light conditions; nowadays: marginally better	marginally worse; can deal with overexposure
Dynamic range	clearly better	lower but High Dynamic Range (HDR) modes allow extremely bright objects as well as darker image areas
Blooming/ Smearing effect	existing due to lower full-well capacity and additional charge carriers	not existing
Shutter	global; well suited for short exposure times	rolling or global; well suited for moving objects
Region of Interest	Fixed because of shift-register structure	Adjustable because of single pixel circuitry
Costs	moderate	less expensive - moderate

As in in-line holography the imager is illuminated by the primary beam, high light intensity capabilities are required. While blooming or smearing effects might therefore be likely, short exposure times and a higher dynamic range justify the use of CCDs. However, High Dynamic Range modes and an improved Global-shutter efficiency in CMOS sensors enable to visualize high-contrast images while preventing motion-blur. Furthermore, shorter exposure times may be achieved by modulating the light source.

> Considering the above advantages and taking into account the emerging trend of manufacturers focusing on CMOS technology, it is the preferred sensor type.

5.3.3. Dimensioning

The remaining points 2. - 4. of the requirements list in section 5.3.1 Requirements address the dimensions of the sensor chip.

Pixel size

The pixel size/pitch should be in the range of the expected particle size, preferably smaller to resolve it with several pixels. Unfortunately, the pixel pitch in CMOS sensors is in strong relationship to the carried out shutter principle due to packaging and complexity reasons of the sensor. That determining factor has to be taken into account as for moving object images, the shutter method has a significant impact. Rolling Shutters require less internal logic and thus allow higher pixel densities. However, the drawback with less logic effort is that the exposure of the sensor is row-wise shifted, which adds additional shear to the imaged object - known as rolling-shutter-effect

(AG, 2016). Preventing that effect, a Global Shutter[5] facilitates simultaneous exposure of all pixels, but at the expense of pixel density.

Imager size

The size of the imager, respectively the width x_{cam} of the sensor chip is, to a major extent, predetermined by the sampling cell geometry. However, it is chosen slightly smaller than the extent of the sampling channel x_{ch}. This is explained by the fact that every beam shaping component (such as the sampling channel) causes diffraction patterns at beam forming edges. With a slightly larger sampling channel these unwanted patterns are moved out of the imagers Field of View. The camera's capability of defining its Region of Interest additionally allows for masking these patterns.

Exposure time

It directly affects the quality of holograms since overexposure of moving objects implies motion blur to images. Quite to the contrary though, the fact of low intensity object waves necessitate long enough exposure times to obtain sufficient fringe pattern contrasts. When aiming flow rates of $Q_{smpl} = 1\,l/min$ and tolerating particles to pass only a few pixels ($10 - 12$ pixels were empirically determined to be tolerable and still allow high-contrast holograms), the required minimum exposure time is in the range of $\tau_{cam} = 20\mu s$.

5.3.4. Camera model selection

A **UI-3082SE-M board-level camera** from IDS Imaging Development Systems GmbH (2018) was found to best meet the requirements listed before.

---

[5]A Global Shutter is required unless the light source is determining the overall system exposure time, that is, the illumination pulses are shorter than the acquisition time of imagers.
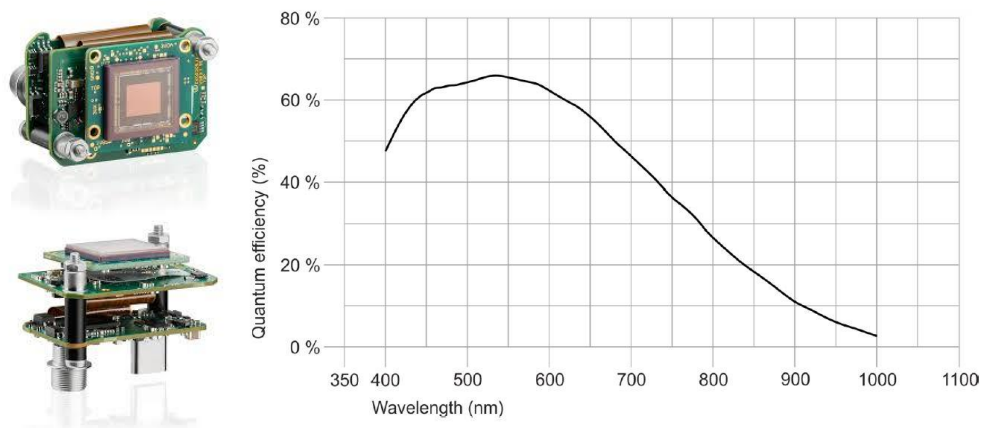
Figure 5.6.: The selected UI-3082SE-M board level camera from IDS (Source: IDS-imaging)
Left: The board-level camera; Right: Quantum efficiency of the camera chip

It is based on a monochromatic CMOS sensor and provides the best compromise between appropriate imager size, small pixel size and Global Shutter availability.

Performance Characteristic	Value
Shutter system	Global-Shutter
Resolution	$2456 \times 2054\,pxl$
Photosensitive area	$8.473\,mm \times 7.086\,mm$
Pixel size	$3.45\,\mu m$
Frame rate (continuous)	$77\,fps$
Exposure time	$0.025\,ms - 999\,ms$
External I/O	Trigger input, Flash output, General Purpose Input/Output (GPIO) pins
Interface	USB Type-C

With the given camera dimensions and a sampling channel depth of $z_{ch} = 4mm$, fringe pattern are of sizes with sufficient pixel resolution to be determinable and do not occupy too much of the detection plane. This is a crucial prerequisite to distinguish patterns, especially at higher particle number concentrations. Also, a quantum efficiency of 60% at the matching wavelength of $\lambda = 635\,nm$ of the laser is essential to achieve highest SNR.

> **Example: Combination of sampling volume and camera**
>
> With a minimum exposure time of $\tau_{cam} = 25\,\mu s$ and a pixel size of $d_{pxl} = 3.45\,\mu m$ a particle may travel at a speed of $v_{prt} = 1.38\,m/s$ and yield a tolerable displacement of 10 pixels. Due to the sampling channel dimensions, the captured sampling volume rates roughly $V_s = 0.24\,cm^3$. and allows for flow rates that are tolerable around $Q_{smpl} = 1\,l/min$.

5.3.5. Mounting

The sampling cell is designed to either attach customized camera mountings or 30 mm cage systems from THORLABS. As can be seen in Figure 5.6, a board-level camera type is used with the sensor chip and the periphery separated to two Printed Circuit Boards (PCBs) and connected via ribbon cable. In that way, sensitive measurements are assured by decoupling vibrations and relief strain from the sensor chip.

The distance z_0 in the sampling geometry of Figure 5.2 on page 92 between the sensor chip and the inner sampling channel wall defines the minimum fringe pattern size. It must also comply with the Nyquist criteria in Equation (3.7) on page 46 for aliasing-free sampling. As a rule of thumb, a minimum distance of the following proves appropriate:

$$z_0 \geqslant 100 \cdot \frac{\Delta_x^2}{\lambda} \tag{5.1}$$

where Δ_x is the pixel pitch and λ the wavelength of illumination.

5.4. The total Particle Imaging Unit

Figure 5.7 shows the total PIU with the equipped window insertion frames and the UI-3082SE-M board-level camera (only the sensor chip PCB) mounted with a 3D-printed bracket. The periphery PCB of the camera is separatly mounted at the rear bottom of the cell (supressed in the figure).

The right drawing is a cut of the sampling volume section to disclose the distances z_0 between the inner sampling channel wall and the camera chip as discussed in the previous section. The distance z_{ch} is essential from the design considerations in 5.1.2 Sampling Channel Depth z_{ch}.
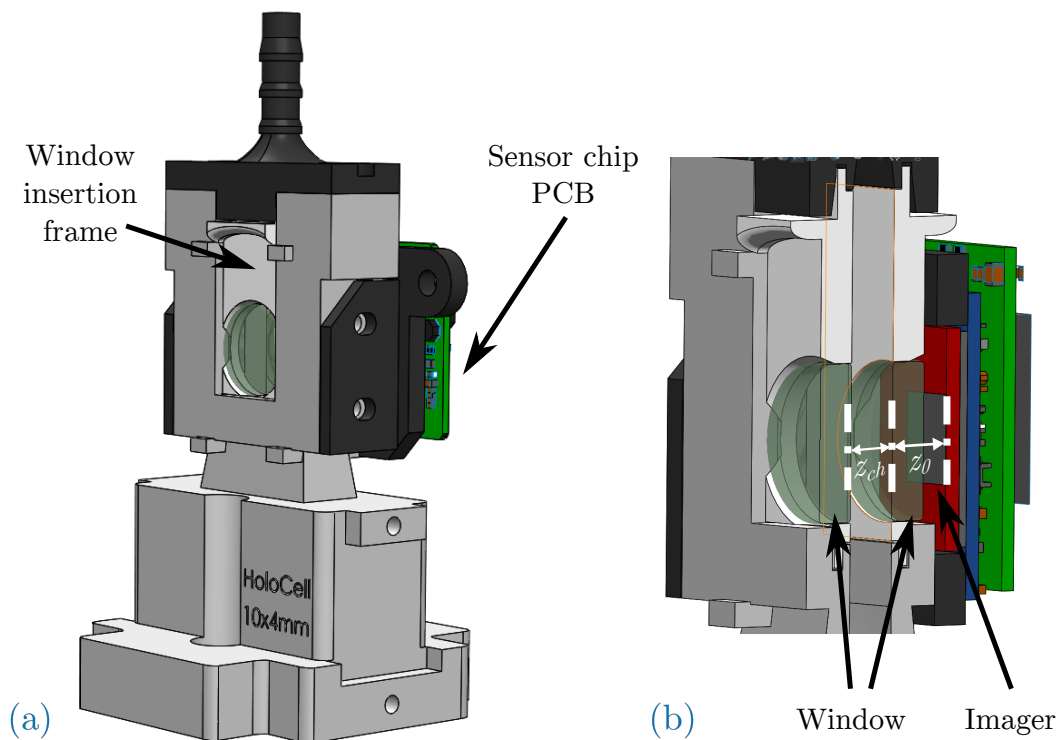

Figure 5.7.: SolidWorks$^{®}$ design of the Particle Imaging Unit (PIU)
(a) the total sampling cell (named: HoloCell) with mounted sensor chip
(b) cut of the sampling volume section.

6. Experiments in the Lab

6.1. The holographic CPC

A prototype of a holographic CPC is depicted in Figure 6.1a. It consists of the Condensation Nucleus Magnifier as the bottom unit and the attached Particle Imaging Unit as the holographical based counting unit. Optical post assemblies from THORLABS are used to position the laser instead of the manufactured laser mounting in Figure 6.1b. In this picture, the PIU is presented in its final configuration level with the laser, camera mountings[1] and fans for preconditioning the cell.

6.2. Acquisition of Holograms

Data Acquisition (DAQ) in this thesis means that the aerosol stream through the sampling cell of the PIU is captured by an imager. The resulting measurement image is a hologram which contains the information of all present particles in the captured sampling volume. Subsequently, a measurement image is referred to as a frame. It represents the more common term in the field of imaging, not least because the data acquisition in the experiments is conducted at a certain framerate.

---

[1] The periphery- PCB of the camera is separated to the bottom socket of the cell
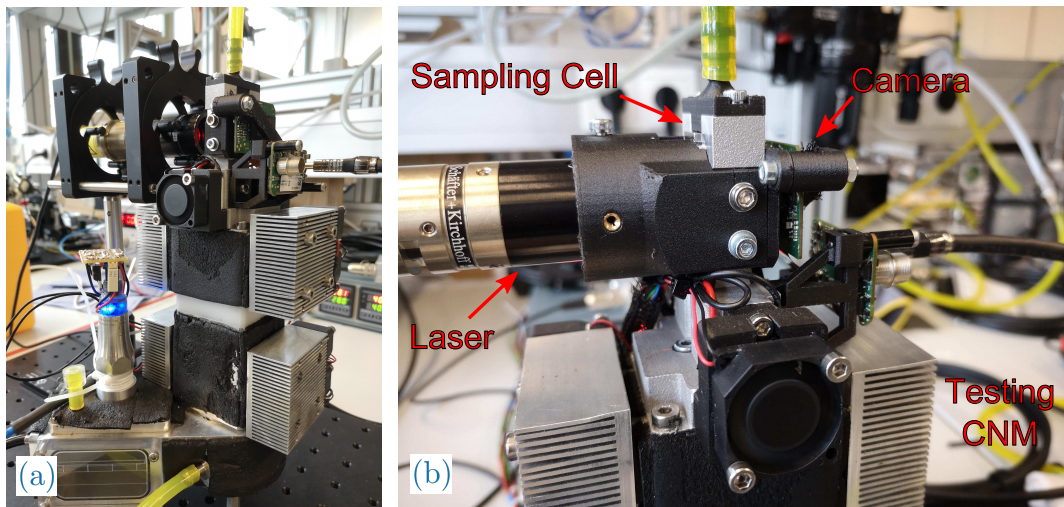
Figure 6.1.: The holographic CPC; (a) View of the total system.
(b) Detailed view of the PIU on top of the testing CNM outlet.

6.2.1. DAQ of Measurement Samples

For the purpose of reliable measurements a MATLAB® App (see the Graphical User Interface in Appendix D) is developed that: 1.) interfaces and controls the camera of the PIU; 2.) calibrates the PIU - see next sections; 3.) acquires, processes and prepares measurement frames; 4.) visualizes live and stored holograms; 5.) detects and counts particles using the developed algorithms from chapter 4 Particle Detection & Analysis and calculates the current particle number concentration; 6.) interfaces and controls a reference CPC - here a TSI-3775; 7.) synchronizes the reference device with the DAQ of the PIU; 8.) performs backpropagation of single holograms to analyse particles; and 9.) manages and saves the collected measurement data

Several steps need to be carried out for proper DAQ of measurement samples:

1. calibration images must be captured before the measurement to calibrate the PIU - cf. 6.3.2 Calibration of the PIU
2. measurement frames are acquired

3. all acquired measurement frames are corrected by the calibration image - cf. 6.2.2 Preparation of Images
4. for long term measurement stability a dynamic calibration is also meaningful - cf. 6.2.3 Dynamic Calibration

6.2.2. Preparation of Images

As the intensity of diffracted waves are magnitudes lower than the direct beam, fringe patterns have a fairly low contrast and are hardly recognizable in the raw image. Furthermore, various system artifacts usually accumulate in the raw image.
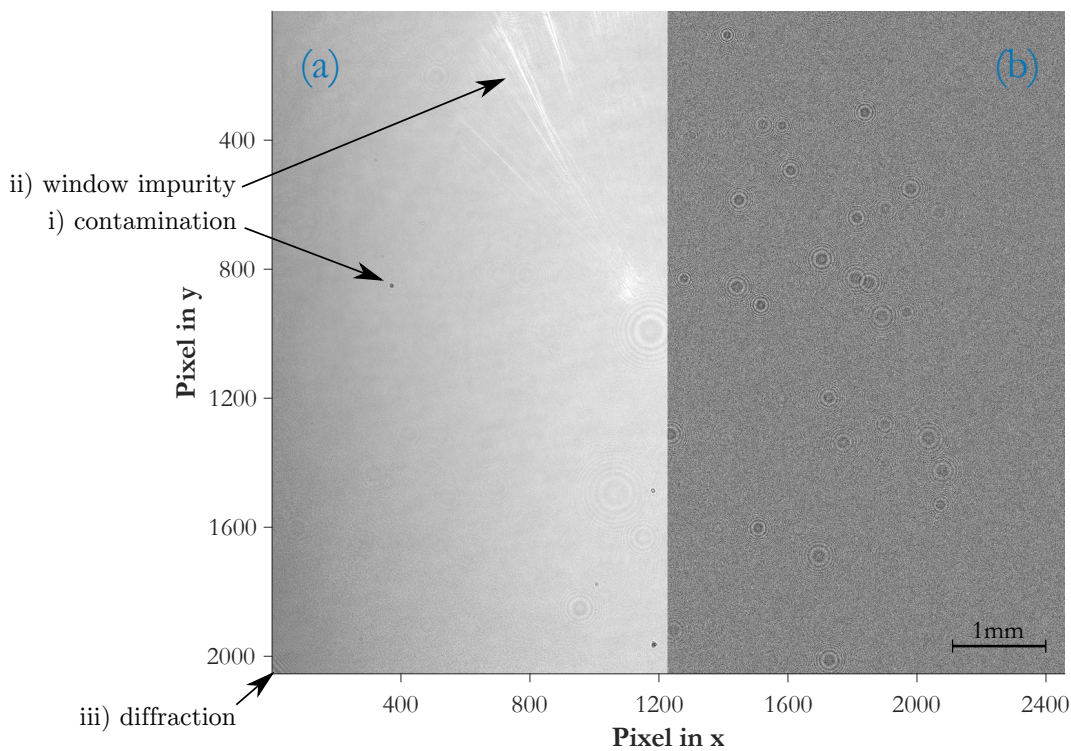

Figure 6.2.: Imaged Hologram Plane: (a) left half of sampled volume as raw image. (b) right half of sampled volume as background corrected image

In order to suppress system artifacts, background correction is necessary where each imaged frame is subtracted by a calibration image (cf. section 6.3.2 Calibration of the PIU). Figure 6.2 depicts the comparison between the raw image of the measurement sample (a) and the background-corrected result, ready for particle detection. Various system artifacts accumulate in the raw image:

i) Contamination of optical elements in the illumination path

The outer laser lens, the sampling cell windows and the sensor chip are under ambient conditions and, thus, prone to contamination such as particles, working fluid residues or residues from insufficient optics cleaning. This is visible where small and intense spots originate from particles sticking onto the sensor chip, and large and rather faint fringe patterns indicate impurities on either the laser lens or the cell windows.

ii) Wear of the sampling cell windows

The partial halo in the upper left image area comes from the sampling cell windows and may be caused by impurities, wear or adhesive residues.

iii) Diffraction patterns

Diffraction patterns are not only caused by objects in the illumination path but by any beam forming edge because every point of the edge acts as a point source of spherical waves. The lower left corner reveals diffraction patterns from the window frame.

6.2.3. Calibration Images

Calibration applies in order to acquire the idle conditions of the imaging unit when no particles are present in the optical path and, thus, system artifacts are subtracted. While non-deterministic effects are difficult to counteract,

it compensates for static artifacts and long term drifts. Non-deterministic effects may be vibrations, for instance caused from fan rotations, and intensity fluctuations of the light beam. Vibrational displacements in the range of the pixel size of the imager are thus unwanted.

Static Calibration

Static calibration is simply the acquisition of frames when no particles are present in the aerosol stream. Multiple "particle-free" frames are captured and averaged to one static background correction image that is subtracted from every succeeding measurement frame to obtain the hologram plane of Figure 6.2b on page 113.

Dynamic Calibration

Long term drifts, as primarily originating from optical path misalignments, are compensated by dynamic calibration. Each new measurement frame adds a weighed contribution to the static background correction. The approach is based on a linear combination of images:

$$I_{0'} = (1 - \alpha) \cdot I_0 + \alpha \cdot I \qquad (6.1)$$

where I_0 is the actual background correction image (without particles), I the actual measurement frame (with particles) that contributes to the updated background correction image $I_{0'}$ by a weight of α.

6.3. Variation of Particle Number Concentrations

6.3.1. Experimental Setup

Below, the main components of the experimental setup, as shown in Figure 6.3, are listed and described in detail in the following paragraph:

- ① Flow controlled pressurized air inlet
- ② Atomizer + Diffusion Dryer
- ③ Dilution Bridge
- ④ Bifurcated flow diluter + laminar mixer
- ⑤ Bypass + mass flow fine tuning
- ⑥ Referencing Condensation Particle Counter (CPC)
- ⑦ Testing Condensation Nucleus Magnifier (CNM)
- ⑧ Particle Imaging Unit (PIU) + Aerosol outlet
- ⑨ TSI-3082 Electrostatic Classifier

The Testing CNM ⑦, equipped with the PIU ⑧, is operated in pressurized mode where the aerosol is fed to the aerosol inlet through the following Flow Control & Size Selection, and Dilution setup: with an ATM220 Atomizer from TOPAS ② a test aerosol is atomized using a 50 ppm NaCl solution. The particle size distribution rates a geometric mean diameter of $d_g = 53.6\,nm$. The reference device ⑥, a TSI-3775, has a 50% cutpoint at $d_{50} = 4\,nm$. The testing CNM, however, is a non-calibrated prototype with a cutpoint at around $d_{50} = 30\,nm$. A quantification of the counting results of the PIU is only meaningful if the Reference CPC as well as the Testing CNM have the same particle growth characteristics. To allow comparability and minimize particle size dependent detection efficiency, a TSI-3082 Electrostatic Classifier ⑨ is used to select particles of size $d = 100\,nm$, for which both condensation units ensure highest counting efficiency.
Pressurized Air (PA) ① at 1.5 bar is supplied to the atomizer. The total flow rate through the dilution section is set to $0.6\,l/min$ by venting overflow aerosol to the ambient over an additional needle valve ⑤. In that manner,
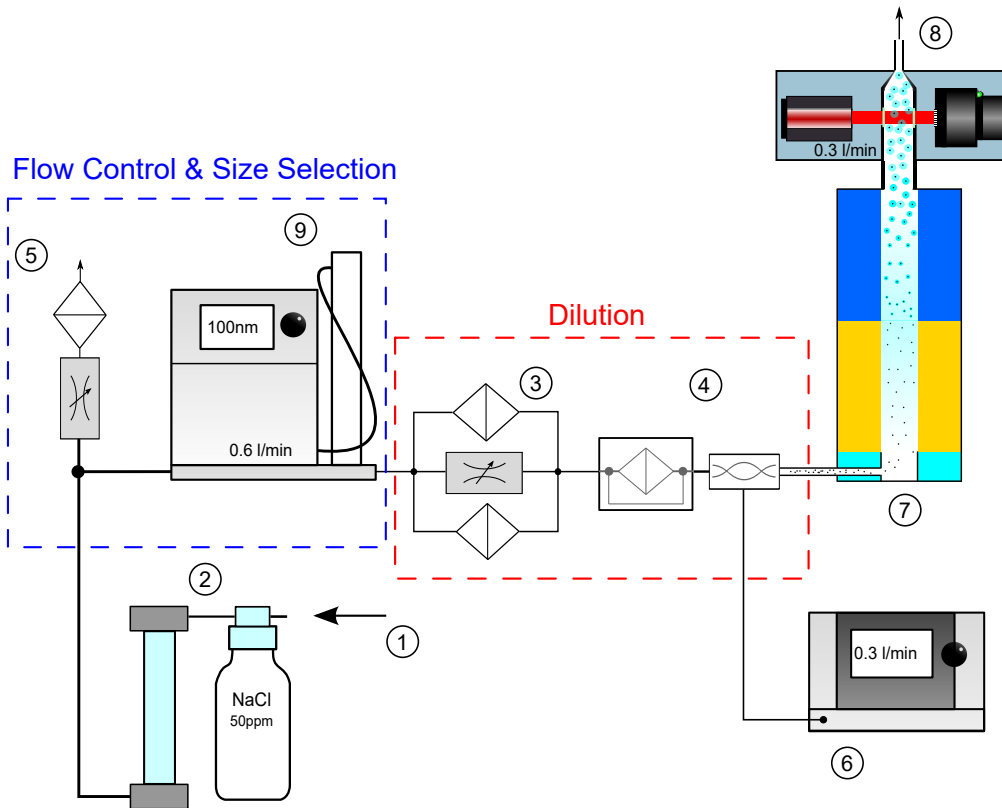
Figure 6.3.: Experimental setup for measurement of particle concentration

an equivalent portion of $0.3\,l/min$ is drawn by the reference[2] and the remaining portion is let through the Testing CNM. Dry air is assured by an oil trap connected directly after the laboratory gas supply; ③ a controllable dilution bridge, consisting of multiple parallel High Efficiency Particulate Air (HEPA) filters and a needle valve to set the dilution, aer used as an adjustable pre-dilution stage; ④ a bifurcated flow diluter from (Bainschab and Alexander Bergmann, 2018) with a fixed dilution rate of 1:17 acts as secondary dilution stage to allow fine adjustment of particle number con-

---

[2]The utilized reference CPC provides a Low Flow Mode which draws $0.3\,l/min$ and a High Flow Mode with $1.5\,l/min$ (TSI Incorporated, 2007). For best comparability the Low Flow Mode is chosen and the aerosol flow through the Testing CPC is tuned to the same level.

centration over the entire dilution path. Note that the total filter area of the upstream dilution bridge is much higher and deliberately placed in front.

The developed MATLAB® App triggers the imaging of the PIU ⑧ and requests new samples of the TSI-3775 ⑥ at the same time. New data acquisition is conducted manually.

6.3.2. Calibration of the PIU

Before each new measurement series, "zero-particle" images are acquired, where the bypass path of the dilution bridge ③ is closed with the needle valve and the total aerosol flows through the HEPA filter section. The sampling flow through the Testing CNM ⑦ remains unchanged to calibrate under regular working conditions. Multiple calibration frames are averaged to a static background image which is subtracted from every measurement image - see the background correction of a particle measurement in Figure 6.2b on page 113. To ensure long term measurement stability, dynamic background correction is activated with a contribution weight of $\alpha = 0.1$ for measurement frames - see in 6.2.3 Dynamic Calibration.

6.3.3. Conduct of the Experiment

The detection- and counting efficiency of the PIU ⑧ is valdidated with a sweep of particle number concentrations. For referencing, the TSI-3775 ⑥ is sampling at the same flow rate of $0.3\,l/min$ and in parallel to the Testing CNM ⑦. Before each measurement series, the particle size distribution of the atomized NaCl solution ② is set to a $100\,nm$ mode with the Electrostatic Classifier ⑨ to operate both condensation units with particle sizes where particle growth is guaranteed. After calibration of the PIU, the particle concentration is manually ramped by adjusting dilution with the needle valve of the dilution bridge ③. The concentration is step-wise increased and monitored with the reference TSI-3775. After the concentration at the Reference CPC ⑥ stabilized, a new measurement sample is manually acquired with the aforementioned MATLAB® App.

6.4. Variation of Aerosol Flow Rate & the stroboscopic Imaging

6.4.1. Experimental Setup

Similar to the previous experimental setup, the main components as shown in Figure 6.4 are the following:

1. Flow controlled pressurized air inlet
2. Atomizer + Diffusion Dryer
3. Dilution Bridge
4. Bifurcated flow diluter
5. Bypass + mass flow tunings
6. Bubble Flowmeter
7. Testing Condensation Nucleus Magnifier (CNM)
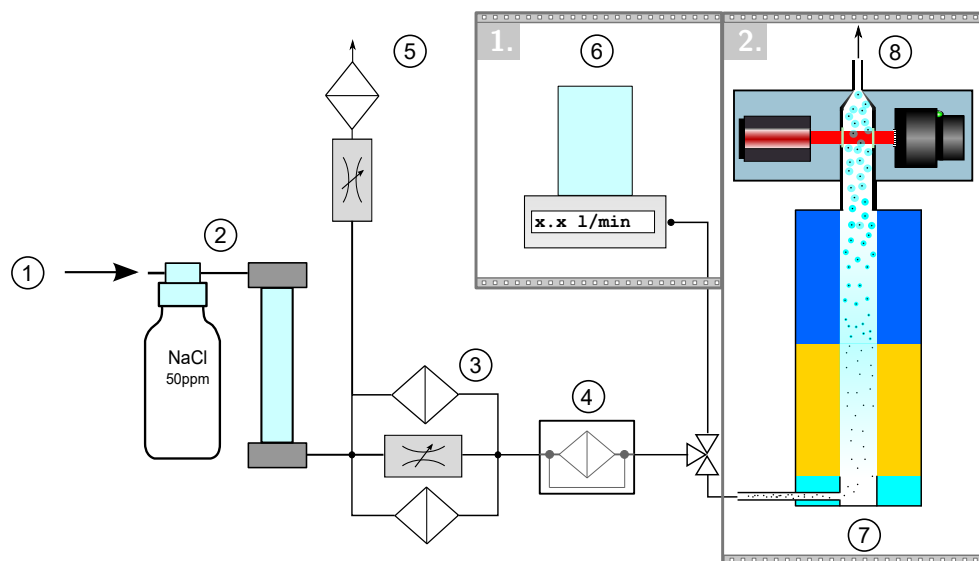8. Particle Imaging Unit (PIU) + Aerosol outlet

Figure 6.4.: Experimental setup for mass flow variations

Again, the Testing CNM (7), equipped with the PIU (8), is operated in pressurized mode using the 50 ppm NaCl solution as test aerosol. The controllable dilution bridge (3) and the bifurcated flow diluter (4) are unchanged and set to provide a constant particle number concentration. The flow rate through the CPC is manually adjusted with the bypass path (5) and measured with a bubble flow meter (6). Instead of the sketched 3/2-way valve, the flow rate is ⎡1.⎤ determined with the bubble flowmeter in series and replaced by the Testing CPC for measurements in a ⎡2.⎤ step.

6.4.2. Stroboscopic Imaging

Typical imaging applications use continuously emitting light sources that illuminate the scence of interest - here referred to as **regular imaging**. Therein, the camera determines the exposure time through its shutter time. As the shutter speed of a camera is limited, the minimum possible exposure time τ_{cam} is also limited (cf. Figure 6.5 ⎡1.⎤). Moving particles, as evident from section 3.3.1 Movement of particles, constitude a problem if their displacement Δd_τ during exposure is to large. Such resulting motion blur could be either compensated by reducing the speed of particles or by further minimizing the exposure time τ.

Unless the imaging system is restricted by a continuous light source, an overall system exposure time τ can be achieved when modulating it. This approach is known as **stroboscopic imaging**. The principle in Figure 6.5 ⎡2.⎤ is the following:

1. the overall system exposure time τ is now determined by the flash duration τ_{on} of the laser
2. the exposure time τ_{cam} of the camera may be arbitrary. If no light is incident onto the camera chip any longer no more photons can be captured by the pixels and the charge collection process is over.
3. both the laser and the capturing of the camera are synchronized which is meaningful for several reasons:

   - *Determinism:* a non-synchronized exposure may lead to a partial overlap of the exposure windows τ_{on} & τ_{cam} and result in an unkown system exposure time.
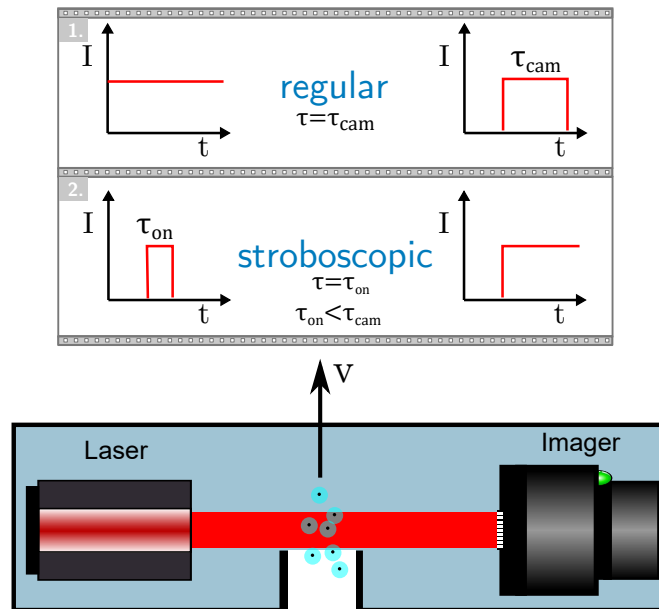
Figure 6.5.: Holographic Imaging: 1. in regular mode where the laser is continuously illuminating and the camera determines the exposure time; 2. in stroboscopic mode where the pulsed laser determines the overall exposure time

- *Partial window overlap:* a deterministic partial window overlap can be deliberatly provoked to further reduce the overall system exposure time (if both camera and light source are at its speed limits)
- *Delay time compensation:* both the light source and the camera exhibit hardware or software delays of the trigger- or strobing process which can be equalized by adequate compensation delays.

4. the laser is adapted to higher light intensities as more light in a shorter period of time can be captured by the photosensitve elements of the camera.

6.4.3. Conduct of the Experiment

Impact of Motion Blur

Measurements are conducted in regular imaging mode where the camera determines the duration of exposure. The aim of this experiment is to evaluate the influence of increasing particle speeds to the imaging quality and the particle's fringe patterns. Therefore, the aerosol flow through the Testing CPC ⑦ is step-wise increased $Q = 0.3, \ldots, 1.2\,l/min$ by manually closing the bypass valve ⑤. The flow rate is determined with a bubble flow meter ⑥ placed instead of the CPC in the pneumatic path prior to new measurements.

The Effect of Stroboscopic Imaging

The utilized LNC-91CM-M60 laser facilitates a TTL modulation input and can be externally modulated up to a frequency of $f_{mod} = 100kHz$. This means a minimum possible exposure time of $\tau_{on} = 10\,\mu s$ which proved sufficient to first ascertain the effective measure against motion blur and second allow for flow rates up to $1.5\,l/min$, required by typical CPCs.
The UI-3082SE-M camera is equipped with GPIO pins that can be configured as flasher ouputs and trigger inputs. The primary idea is to directly modulate the laser with the camera's flasher output capability. However, with experienced delay times of roughly $64\,\mu s$ the flasher output of the camera disqualifies for deterministic short time laser pulse generation. Instead, an Arbitrary Waveform Generator is used to synchronously modulate the laser and trigger the image capturing of the camera via its trigger input. Therefore, Channel 1 of the function generator generates the modulation pulse of $\tau_{on} = 10\,\mu s$ and Channel 2 generates a strobe flank to trigger the camera. The exposure time of the camera is set to a longer duration of $\tau_{cam} > 1ms$ since the laser pulse now determines the duration of exposure. To compensate timing delays of the camera, the laser pulse generating Channel 1 is time delayed with respect to the camera triggering Channel 2. In this way, the flashing window of the laser is moved into the time period where the camera is already capturing.

To evaluate the counter measure of stroboscopic imaging, the experiment is conducted at a constant flow rate of $Q = 0.9 \, l/min$[3] through the Testing CPC. First, measurements frames are acquired with the PIU operated in regular mode and with the regular configurations: the laser is permanently on and the exposure time of the camera is set to $\tau_{cam} = 56 \, \mu s$.

In a second step, measurement frames are acquired with the laser modulated at $\tau_{on} = 20 \, \mu s$ and configured to a stroboscopic imaging mode as discussed above.

---

[3]Higher flow rates yield condensation at the windows due of insufficient heating.

7. Discussion of Results

This chapter discusses results also published in Georg Brunnhofer, Alexander Bergmann, Klug, et al., 2019 and G. Brunnhofer et al., 2020. It additionally includes unpublished and revised material.

7.1. Performance of the different Particle Detection Methods

In the following section the results of the customized Hough Transform, blob detection and the Deep Convolutional Neural Networks are compared in terms of detection performance and computational speed and which method is most suitable for the application in Holographic Particle Counters. For that purpose, an imaged hologram of a real measurement sample is taken as an example image where the density of fringe patterns is moderately high. Subsequently, a selected section of that image is used to first assess the Hough Transform and blob detection on an empirical basis. It contains strongly overlapping but also clearly separated fringe patterns and poses certain complexities to both methods. The neural network needs to be assessed with multiple validation images instead.

The second part outlines a qualitative comparison of all methods based on a real measured data set.

7.1.1. Customized Hough Transform

The aforementioned image section in Figure 7.1b shows mutliple overlaps of several fringe patterns in the lower right corner and a very strong merge in the lower left part. The dense group of patterns in the right corner is

almost entirely detected, except for one missing hit (tagged in orange). The preprocessed image (a) reveals that all innermost fringes are resolved very sharply and suggests that the sensitivity S_{HT} of the HT should be refined to recognize the missing hit as well. However, a higher sensitivity was identified to lead to an increase in false-positive hits and was hence deliberately avoided.
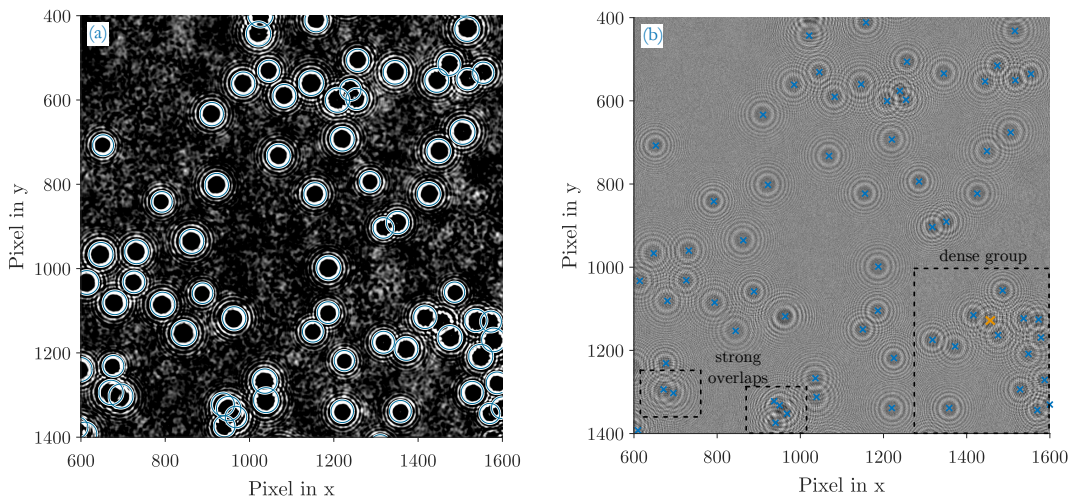

Figure 7.1.: Detection result of the customized HT (selected image section)
(a) Gaussian filtered fringe patterns ($\sigma_{lp} = 2.62$) where all detected fringes are highlighted with circles
(b) the original fringe patterns. Its determined centroids equal the actual position of the particles in the xy- plane. There is one missing hit (orange).

Strong overlaps in the lower left corner are reliably separated. While a distinction of the left two patterns can be validated through visual inspections and experiences, the right group is strongly bundled and requires backpropagation means to verify the particles in the reconstructed 3D-volume (not elaborated in this work but the actual count of particles in this particular bundle is indeed 4).

7.1.2. Blob Detection

The Particle Imaging Unit provides fringe patterns in which the majority of center spots are dark. These dark centers equal multi-scale blobs that are extracted by the multi-step template matching approach. Since the filter kernels of the templates are non-normalized, a bias in pixel intensities is introduced during filtering. In terms of the image histogram it narrows the mainlobe of Gaussian intensity distribution due to lowpass filtering and shifts it to brighter intensity values as a consequence of the bias (compare the histograms of Figure 4.2 on page 70 with Figure 7.2b).
The final histogram is right-sided with a mainlobe relating to the background and a certain side-distribution to its left which contains the information of the darker center blobs (and fringes of odd parity).
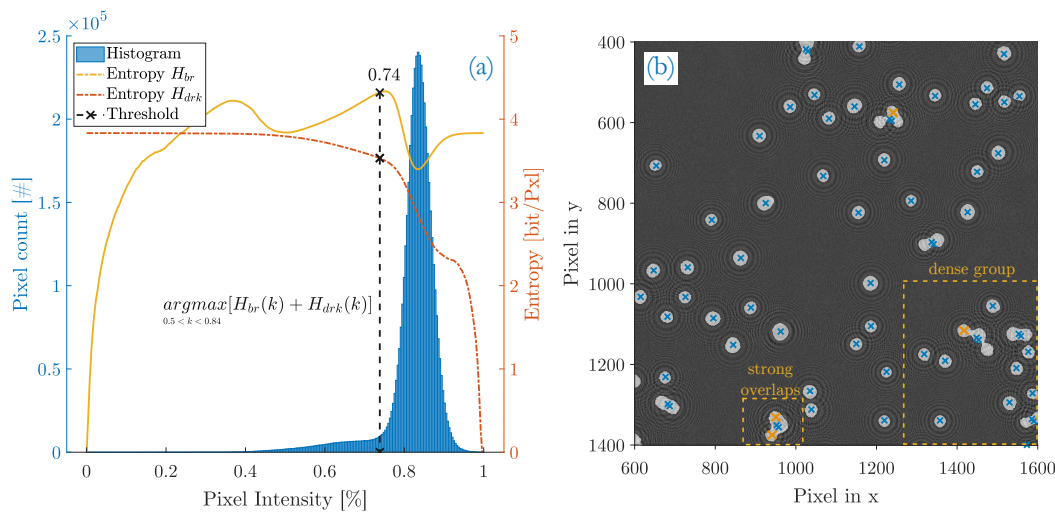
Figure 7.2.: Detection result of blob detection (selected image section).
(a) histogram and the optimal threshold k_{opt} of the whole image, obtained by maximum entropy thresholding. Equation (4.5) needs to be confined to a lower threshold limit set to $L_1 = 0.5$ and an upper limit of $L_2 = 0.84$ which is the peak of the mainlobe.
(b) fringe patterns overlaid with the corresponding blobs that result from a threshold of $k_{opt} = 0.74$. Four hits are missing (orange).

With maximum entropy thresholding, the optimal intensity threshold k_{opt} is found where the best contrast is obtained in terms of maximum information transfer. Its indicative measure is the maximum sum entropy $H_{max} = \max[H_{br}(k) + H_{drk}(k)]$. Figure 7.2a shows the determination of the sum entropy with the entropy H_{br} of bright pixels and the entropy H_{drk} of dark pixels plotted separately. In this particular example image, the correct optimum threshold is located close to the left of the mainlobe at $k_{opt} = 0.74$. However, the algorithm would actually fail to find that threshold because the background entropy H_{br} gains a peak at lower pixel intensities (at $k = 0.37$) and the actual maximum sum entropy would be erroneously reached at that particular threshold value. To avoid such misinterpretations, the thresholding limits L_1 and L_2 in Equation (4.5) are introduced. The upper limit L_2 equals the histogram bin of the mainlobe peak and is determined for each sample image individually. Evident from the given fringe pattern properties, the intensity of blobs will not exceed background levels and is therefore always located left of the mainlobe. L_1 is a rather empirical value and is set to 0.5 as a threshold for right-sided histograms.
The unwanted peak in the background entropy H_{br} is a system artefact introduced by the imaging process of particles and can have different reasons. Some were identified as being caused by: 1. higher background flicker as a consequence of high particle densities. A rising number of particles means an increase of speckle noise due to multiple scattering; 2. fluctuations in the background that may come from vibrations during the imaging process or instabilities of the light source; or 3. an inhomogeneous exposure of the camera with a tendency to poorer illumination at the detectors corners.

Figure 7.2b depicts the same image section of fringe patterns as before but overlaid with the resulting blobs after thresholding. Blue crosses are the centroids of each fringe pattern and correlate to the $xy-$ position of its respective particle unless the shape of the blob deviates too much from an ideal circle of 1. In such cases, the assumption is made that at least 2 fringe patterns are overlapping and a correction in the count of detected particles is made by $+1$ for each affected blob. A second cross nearby the actual blob centroid marks the correction made. Of course, the actual particle position does not relate to the determined centroids any more. Orange crosses annotate valid fringe patterns which the algorithm does not recognize. These are mssing hits.

7.1.3. Deep Convolutional Neural Networks

The detection performance of the DCNN is evaluated in terms of accuracy and precision. A computer with an Intel Xeon W-2145 (Skylake-W) 8-Core CPU and a GPU (NVIDIA GeForce RTX2080 TI) is used. Regarding the training dataset, around 6,000 artificially generated holograms were modelled with the Holographic Aerosol Particle Model and ultimately 64 images are selected as a validation dataset. In these datasets the number of particles steadily increases from 0 to greater than 200 particles. The number of epochs for the training was 50 and the training time was approximately 4.5 hours.

Table 7.1.: Accuracy and precision of the DCNN

Number of particles	Precision	Accuracy
53	0.55	0.98
88	0.45	0.91
103	0.36	0.87
155	0.35	0.74
180	0.25	0.69

Table 7.1 shows the accuracy and precision values of the selected samples. In this selection, particles are ranging from 53 to 180. The accuracy is calculated by the number of True Positives + True Negatives divided by the total number of predictions. The formula for precision is the number of True Positives divided by True Positives + False Positives. If no detection of a False Positives takes place the precision is 1.0.

7.1.4. Comparison of Computational Speed

The comparison of computational speed is based on a dataset of ramped particle number concentration and will be discussed in detail in the next section (7.2.1 Variation of Particle Number Concentration). The processing time of all three counting methods is examined on every sample point of the measurent curve. These sample points of C_N are directly proportional to the counting rate of particles N as given in Equation (4.9). Figure 7.3

compares the computational speed of the methods as a function of particle number concentration. It must be mentioned that both the blob detection and the customized Hough Transform are MatLab based algorithms which are executed on CPU without GPU support. The U-Net, on the other hand, is a Python script running on a GPU which is optimized for Artificial Intelligence (AI) applications.

The blob detection and the U-Net are nearly constant over all measurement samples. With an average processing time of roughly $0.45\,ms$ the blob detection is the fastest and selected as the benchmark to which the other algorithms are normalized for comparison. The U-Net is slightly slower with an average processing time of $0.68\,ms$ or, in terms of computational speed, takes a factor of 1.56 longer in calculation than blob detection.
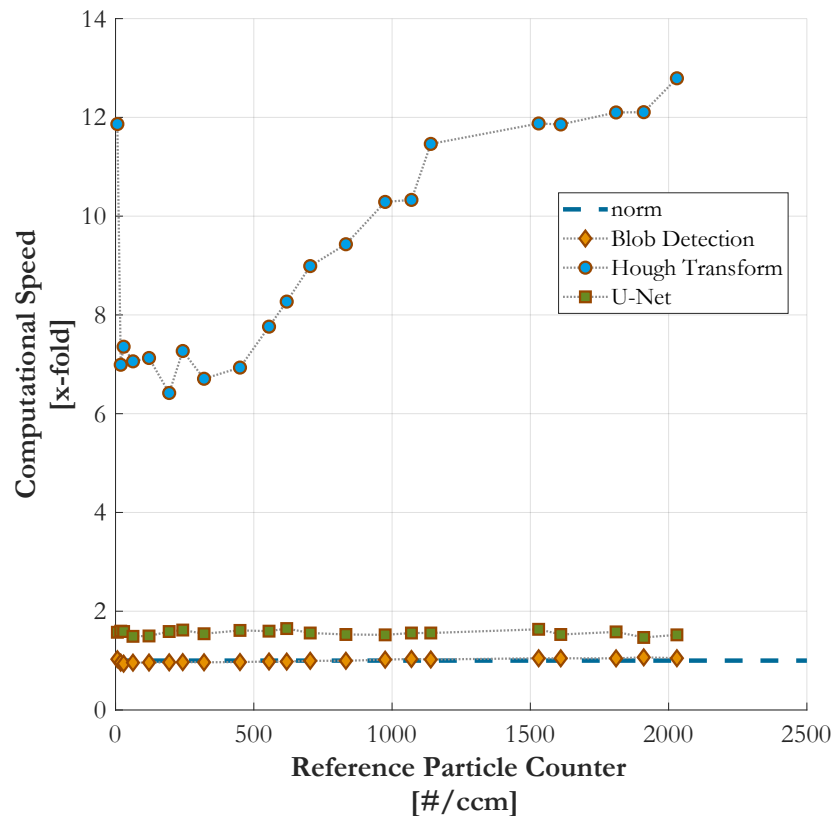

Figure 7.3.: Comparison of processing time

The customized Hough Transform takes at least 6 times longer and exhibits a strong dependence on the particle rate. There, the number of particles may be interpreted as the number of cycles the algorithm has to iterate to obtain its counting result. It is reasoned in the single transformation of every fringe pattern occurence into Hough space. On closer inspection the bob detection behaves similarly due to the segmentation and labeling of the growing number of blobs. The impact is at a very small and narrow scale though. Hence, the dependence on the number of particles is negligible. The U-Net utilizes linear and invariable convolution, pooling and sampling operators and therefore operates at a steady speed.

7.2. Experimental Validation

7.2.1. Variation of Particle Number Concentration

Figure 7.4 shows the measurement result of the particle number concentration ramping, monitored by the reference TSI-3775. The measurement samples are acquired by the Particle Imaging Unit and processed with the three discussed counting algorithms:

- (a) customized Hough Transform
- (b) the blob detection with maximum entropy thresholding
- (c) DCNN based on a U-Net

The concentration is ramped from 0 to 2030 $\#/cm^3$ which, in terms of images to process entails an average count of roughly 0 to 488 fringe patterns per image. Each data point is the averaged counting rate over multiple acquired frames at a camera frame rate of 23 fps. With 3 frames per measurement point the total sampling time per point is about $\tau_s = 130\,ms$ and therefore similar to the period settings of the moving average filter of the TSI-3775 (TSI Incorporated, 2007).
The measurement curve is fitted with a polynomial regression function of 2nd order where the second coefficient is the slope b of the regression.
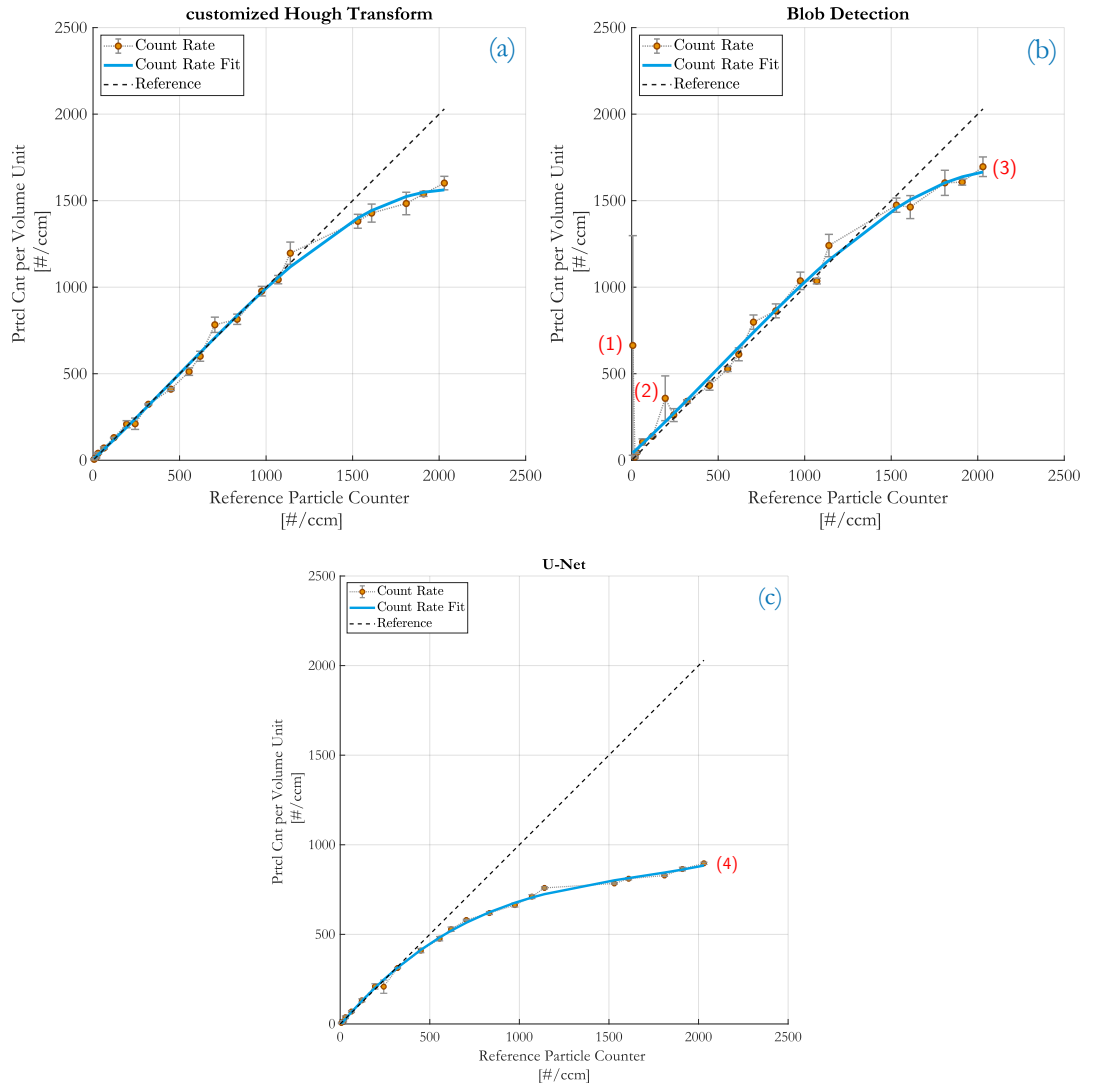
Figure 7.4.: Comparison of the monitored particle number concentration to the counting
rates obtained by the PIU.
(a) with customized HT
(b) with blob detection and maximum entropy thresholding
(c) with DCNN based on a U-Net

Correlation between the PIU and a Reference CPC

For each detection method, Figure 7.4 illustrates the following:

- ─── a polynomial fit of the measurement set
- ⋯⋯ the slope b of the fit
- ‑ ‑ ‑ ‑ the ideal correlation between the flow-based particle number concentration result of the TSI-3775 and the volume-based counting rate of the PIU

The slobe b can be seen as the correlation factor of the actual measurement set. From Equation (4.9) on page 75 it is clear that this factor with $b = 0.28$ for the customized Hough Transform, $b = 0.29$ for blob detection and $b = 0.22$ for the U-Net corresponds to the sampling volume of $V_s = 0.24\,cm^3$. The slight mismatch is caused by the regressive behavior of the counting rate. It is reasoned in the phenomenon of particles coinciding along the optical path at higher concentrations (as described in section 4.3.1 Time-based versus Area-based Coincidence).
All three counting methods provide good linearity as long as fringe patterns are spatially well separated ($C_N < 500\,\#/cm^3$). As the particle density increases, the likelihood of partially overlapping fringe pattern rises and the detection performance of the DCNN significantly drops. On the contrary, the customized Hough Transform and the blob detection can handle particle number concentrations up to approximately $C = 1250\,\#/cm^3$ (or 300 particles per frame) before a regression is noticeable. This implies that partial overlaps are separable very well with these two methods (compare also Figure 7.1 and Figure 7.2). At higher counting rates fringe patterns do not only partially overlap any more but start to superimpose to a mutual pattern of fringes at which neither algorithm is capable of resolving this complex formed patterns (a separation task like this now requires backpropagation algorithms - cf. 4.2.2 Particle Localization in 3D).

Figure 7.5 clarifies the implication of coincidence where fringe patterns at higher particle densities are simply missed (here: exemplarily detected with the customized Hough Transform). At lower counting rates, less particles are present in the sampling volume and spatially well distributed to generate pronounced and well separated fringe patterns at the detector (see in Figure 7.5a). At higher particle densities, starting at around 1250 $\frac{\#}{ccm}$, the
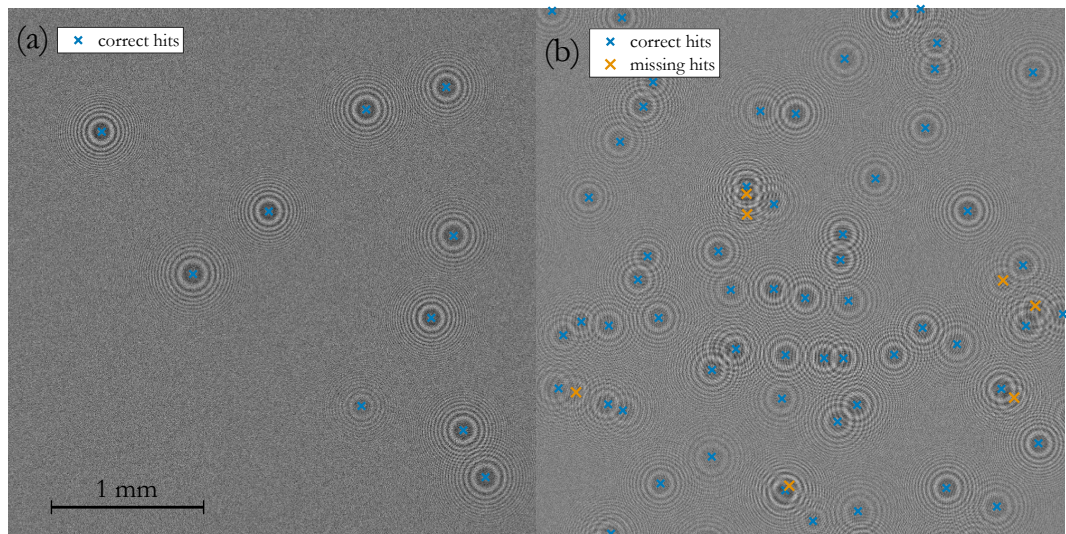
Figure 7.5.: Zoomed segments of frames with the customized HT at: (a) low particle density of 78 $\frac{\#}{frame}$ and no missing hits; (b) medium particle density of 273 $\frac{\#}{frame}$ with missing hits. Because of intrinsic higher speckle noise in the right frame segment, the contrast is lower while the background noise level is increased.

probability of coinciding particles and, thus, overlapping fringe patterns rises (see in Figure 7.5b).

Furthermore, multiple scattering increases background noise level and lowers the contrast of fringe patterns - cf.: Equation (7.1) on page 138.

Comparison of the Algorithms' Detection Performance

Referring again to the counting results in Figure 7.4 the conclusion can be drawn that the counting performance of the customized Hough Transform and the blob detection is very similar in terms of counting rates.

The **customized Hough Transform** is more robust against noise and intensity fluctuations in images and therefore less erroneous, however. The detectability of fringes at even strong overlaps is very high as was discovered in Figure 7.1 on page 126. Images without particles are unproblematic and make this method a good candidate for "zero-particle" monitoring.

In **blob detection**, strong overlaps of fringe patterns lead to merged blobs (see also Figure 7.2 on page 127). This problem is counteracted with the implemented corrective measure where non-circular blobs are treated as multiple occurances (cf. 4.1.2 Blob Labeling and Counting). Such blobs are double counted which acts to some extent as a coincidence correction. As a result, the blob detection even gains a slight advantage over the Hough Transform at higher particle densities (3). However, annotations (1) and (2) reveal the weaknesses. They indicate sample points where only single measurement frames are distorted by high background fluctuations. As a consequence, the recognition of patterns in these frames fails and yields mainly False Positives, as evident from the concerned measurement frames in Figure 7.6.
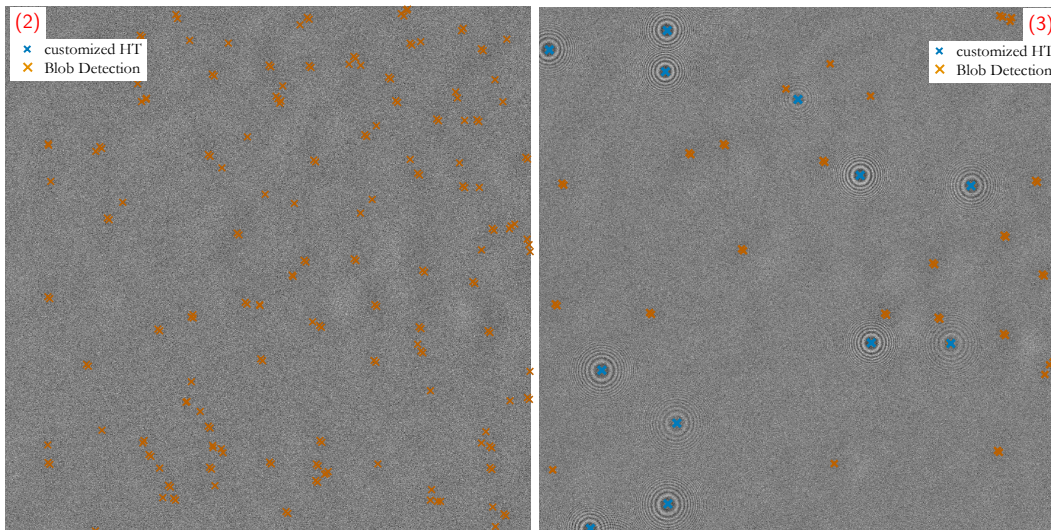

Figure 7.6.: Zoomed segments of measurement samples from Figure 7.4 that suffer strong background fluctuations: (1) zero-particle frame; (2) particle number concentration of $C_N = 194\,\#/cm^3$; While the customized HT outputs correct hits (only True Positives), the blob detection in both scenarios fails (also False Positives) because of a misinterpreted intensity threshold in the histogram.

Therein, high background fluctuations are distorting the pattern recognition. Since blob detection is based on histogram thresholding a misinterpreted threshold leads to incorrect detection hits. The fluctuations add low pixel

intensity shares to the histogram which are confused with dark areas of fringe patterns. In the case of zero-particle frames the impact of a misinterpreted threshold is vastly. Because the histogram is divided into foreground and background pixels, zero-particle images are more difficult to classify and prone to misclassifications. The **DCNN**, and in particular its detection performance, is comparible with the other methods at low particle concentrations ($< 500 \, \#/cm^3$). It is capable of classifying zero-particle images as well as images with higher background fluctuations and is as powerful as the customized Hough Transform. The high accuracy at low particle numbers from Table 7.1 also confirms these good detection rates. At higher concentrations though, Figure 7.4 with annotation (4) and Table 7.1 illustrate the strong decrease in detectability. The reason is that as the number of particle increases, fringe patterns start to overlap for which the network is insufficiently trained. Although the training dataset contained numerous occurences of fringe pattern overlaps, the network was trained specifically for individual occurences Since the accuracy of a DCNN depends on training, an enhanced set of training data would improve the detection performance at least to a limited extent. Due to the lack of real measurement samples and its ground truth data, primarily only modelled holograms could be used. Thus, the training relies on the degree of reality in the Aerosol Particle Model which provided the training data.

Another reason is in the loss of border pixels in every convolution step. Fringe patterns located at the border of images are therefore likely to be missed. Especially at higher particle concentrations the probability of more particles passing at the edge of the detector increases, degrading the detection performance additionally.

General Limit of Detection (LoD)

The **sensitivity** of measuring particle number concentration is determined by the sampling volume and rates about $4.16 \, \frac{\#}{ccm}$ for a single shot. When averaging multiple frames, the sensitivity may be easily increased by raising the camera's frame rate. In this manner, an improvement of e.g.: factor 20 is achieved with a frame rate of $20 \, fps$ (the integration interval is then 1s), which yields an improved sensitivity of $0.208 \, \frac{\#}{ccm}$. Integration time, however, may also be increased while maintaining a constant frame rate and thereby

improving sensitivity. It may not only be increased by averaging multiple frames but also by adapting the sampled volume. CMOS- imagers typically allow to configure a certain Region of Interest which implies to alter the imaged sampling volume.

The **minimum particle size** that is theoretically detectable with the Particle Imaging Unit is in the size range of around $1\text{-}2\,\mu m$. Therein, the shortest distance $z_{prt} = z_0$ yields the lower limit and $z_{prt} = z_0 + z_{ch}$ the higher limit. This is defined by the Rayleigh resolution limit in Equation (2.31) from section Minimum Particle Size.
In practice, the minimum detectable size of particles is also a matter of detecting sufficient intensity of the particle's diffracted wave to outstand system noise (Falgout, Chen, and Guildenbecher, 2019). Consequently, the dynamic range of the camera also contributes to the achievement of lower size limits which realistically lie in the range of $3\text{-}4\,\mu m$. Investigations may be a task for further studies.

General Detection Uncertainties & Limitations

Because of the direct imaging of the total number of particles in a given volume, the method is not only of first principle but also a true "zero-particle" monitor. However, several influences contribute to uncertainties in the unambiguous recognition of particle's fringe patterns and consequently affect the unambiguity of particle number concentration.

Illumination inhomogeneity in the sampling volume may lead to darker regions where particles are illuminated with lower light intensity and thus diffract less energy. The beam profile of lasers typically exhibit a Gaussian intensity distribution. The utilized laser is designed to have a flat intensity profile over a certain cross section of the beam. Originally, an aperture defines that cross section and makes the laser suitable for applications using that specifc light beam shape. In the Particle Imaging Unit the aperture needed to be removed to have the whole beam cross section available. As evident from the raw image in Figure 6.2a on page 113, the laser intensity

at the edge of the channel is decreasing, resulting in a weaker particle illumation. As a consequence, a vanishing intensity of fringe patterns in that affected regions raises the probability of missing detection hits.

Multiple Scattering is an inevitable cause of imaging quality degradation at higher particle densities because of the rising impact of speckle noise with (recap of Equation (7.1) on page 138):

$$\sigma_N = \langle I_N \rangle = C_N \cdot \frac{\pi^3}{48} d_{prt}^2 \cdot z_{ch} \tag{7.1}$$

Comparing Figure 7.5a with Figure 7.5b, the intensity of the background level is slightly increased while the contrast of fringe patterns is lower. For CPCs, where the particle diameter is uniform, the noise intensity linearly inreases with the particle number concentration.

Coincidence of particles is the major drawback when using standard 2D pattern recognition techniques for particle detection instead of typical wavefront reconstruction algorithms. As evident from Figure 7.5, fringe patterns start to overlap at higher particle densities as a consequence of the rising probability of coincidence. 2D pattern recognition schemes fail to differentiate all valid hits and underestimated the actual counting rate.

7.2.2. Variation of Aerosol Flow & the Stroboscopic Imaging

The experimental results are taken from the bachelor thesis *"Analyse und Maßnahme zur bildgebenden Detektion von bewegten Aerosol Partikeln"* of Philip Bergmann, which was conducted and supervised in the course of the PhD thesis.

Impact of Motion Blur

The experiment of aerosol flow variations aims to show the impact of motion blurring caused by either too high particle velocities or to long exposure times. The blurring effect on fringe patterns, however, depends on multiple influences: the contrast of fringe patterns is influenced by illumination conditions (light intensity, duration of exposure), the size of the particles and its optical properties. The expansion of fringe patterns depend on the $z-$ location of the particles. Unfortunately, the velocity of particles affects fringe patterns as a function of all aforementioned influences. On top of this, the aerosol stream does not provide constant particle velocities.
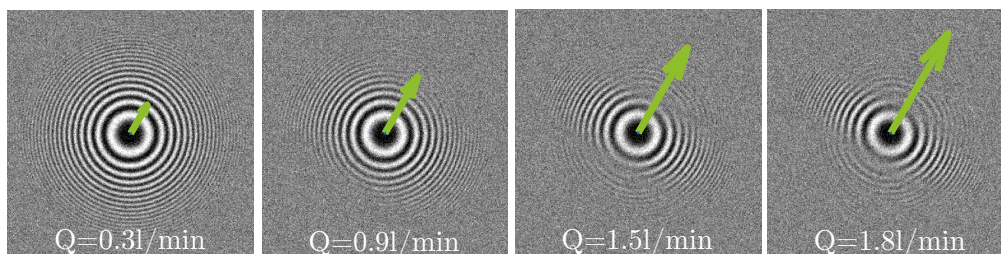

Figure 7.7.: Modelled fringe patterns with gradually increased speed of motion to demonstrate the impact of motion blur.

A quantitative analysis would require finding particles of identical conditions to compare. Instead, and for the sake of demonstration, motion blur is modelled and exemplarily illustrated in Figure 7.7. A particle is modelled with a constant size and location but with a gradually increased speed of motion in direction of the annotated arrow.

With increasing particle velocities, as a consequence of higher flow rates, fringe patterns are stronger smeared by motion blur along the motion axis. The higher the flow rate the greater the impact of smearing. Experiments clearly proved the degradation of fringe pattern contrasts, level of detail of fringes and reveal the direction of motion based on the blurring.

Stroboscopic Imaging

While the flow rate through the Testing CPC is kept constant at $Q = 0.9\,l/min$, the imaging mode is changed from the regular to the stroboscopic mode. Figure 7.8 contrasts a measurement frame acquired in regular mode (a) with a measurement sample imaged in stroboscopic mode (b). In regular mode, the exposure time is determined by the camera with $\tau_{cam} = 56\,\mu s$. The duration of exposure is clearly to long to obtain a good quality image. The fringe patterns are faint and suffer from lower contrast and fewer details.

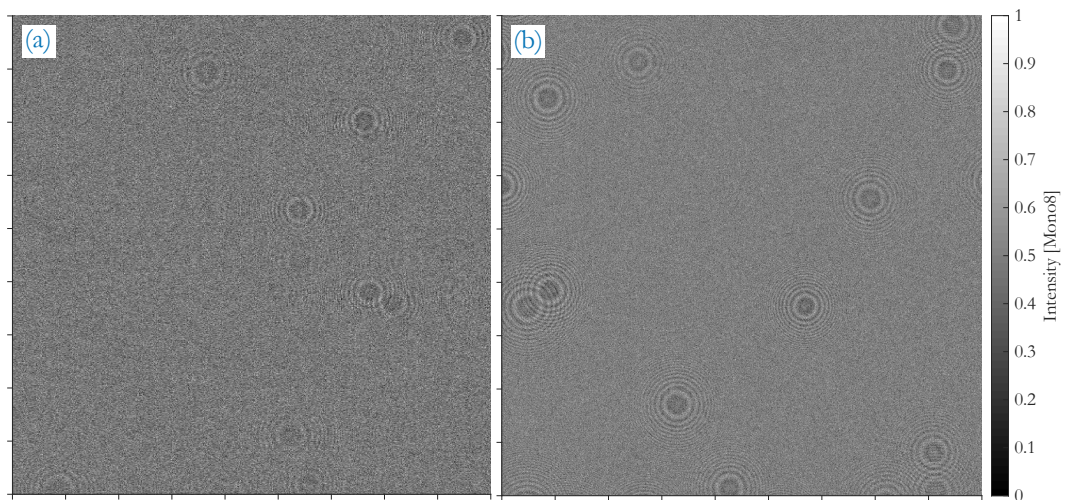
Figure 7.8.: Demonstration of stroboscopic imaging at a flow rate of $Q = 0.9\,l/min$; (a) measurement frame acquired in regular mode with $\tau_{cam} = 56\,\mu s$; (b) measurement frame acquired in stroboscopic mode with $\tau_{on} = 20\,\mu s$

In stroboscopic mode, the overall system exposure time is reduced to $\tau_{on} = 20\,\mu s$. Fringe patterns are cleary sharper and more pronounced.
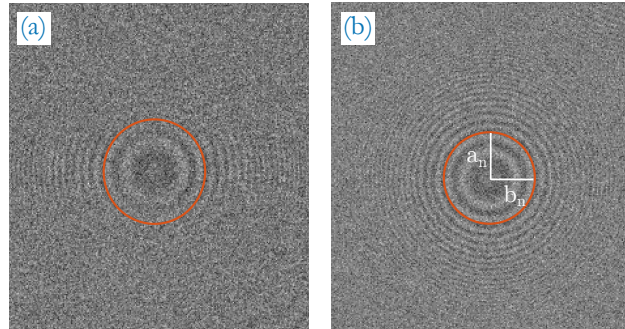
Figure 7.9.: Comparison of zoomed fringe patterns with circles marking each 4th fringe; (a) acquired in regular mode with $\tau_{cam} = 56\,\mu s$ (the direction is apparently vertical); (b) acquired in stroboscopic mode with $\tau_{on} = 20\,\mu s$

Having a closer look at fringe patterns in both cases in Figure 7.9, shorter exposure times (b) definitely improve the quality and level of detail of fringes. At rising particle speeds or longer exposure times, fringes of higher frequencies are blurred entirely, especially along the axis of motion.

Approximation of Speed of Motion

Subsequently, the elaborated hypothesis of extracting particle trajectories from section 4.2.4 Particle Trajectories is verified on basis on Figure 7.9 where in both cases, the course of the 4th fringe is approximated and marked with an ellipse of semi-major axis a_n and semi-minor axis b_n. The major axis points in the direction of the blurring and, hence, in the direction of motion. The minor axis is the unchanged radius of the corresponding fringe because it is unaffected by blurring. It can be used to estimate the particle's depth z_{prt} with Equation (4.10) on page 76.
Based on the obtained depth z_{prt}, the index of the evaluated fringe n and the determined axis ratio $a_n/b_n = a/b$ of the corresponding framing ellipse, the particle's speed of motion can be estimated with Equation (4.13) on page 79.

Table 7.2.: Measured and calculated values for motion-blurring in Figure 7.9

Mode	Given					Calculated			
	τ	a_n	b_n	n	N	z_{prt}	Δd_τ	v_{prt}	Error
	μs	pxl	pxl	-	-	mm	μm	m/s	m/s
regular	56	40	38.5	4	30	6.9	28.34	**0.506**	± 0.335
stroboscopic	20	35	34.5	4	30	5.6	9.44	**0.472**	± 0.472

Table 7.2 represents the results of speed of motion estimation in Figure 7.9. The exposure time τ is predetermined by the camera in regular mode, and by the laser modulation in stroboscopic mode. While the total number of fringes is assumed to be $N = 30$ for typically resolved fringe patterns, $n = 4$ is chosen because the 4th fringe is detectable and yet affected by blurring in both imaging modes. The background of half pixel notations is that the diameter of fringes is measured rather than their radii to reduce already high measurement uncertainties. In case of the short exposure time in stroboscopic mode, the elongation of the pattern is only 1 pixel and thus very vague.

The table reveals that a particle's displacement of only few pixels is identified in both imaging cases. This makes a precise determination of particle distances and speed of motions difficult, however.
Distances of $z_{prt} = 6.9\,mm\,\&\,5.6\,mm$ and velocity estimations of roughly $v_{prt} = 0.5\,m/s$ are plausible for the sampling cell and the applied flow rate of $Q = 900\,ml/min$ through it. Nevertheless, uncertainties are large due to subpixel resolution requirements.

A fringe pattern is motion-blurred by the displacement Δd_τ. Inner fringes are less affected by the smearing but the effect is still identifiable and can be used to estimate the particle's speed of motion v_{prt} and its distance z from the detector. However, only few pixels or subpixels carry information which involve large estimation uncertainties.

7.3. Results of Coincidence & Correction Methods

7.3.1. Time-based versus Area-based Coincidence

The interlink between time-based pulse signals and fringe patterns (cf. Figure 4.6 on page 83) is best explained with the intensity distribution of fringe patterns in form of a surf plot in Figure 7.10.
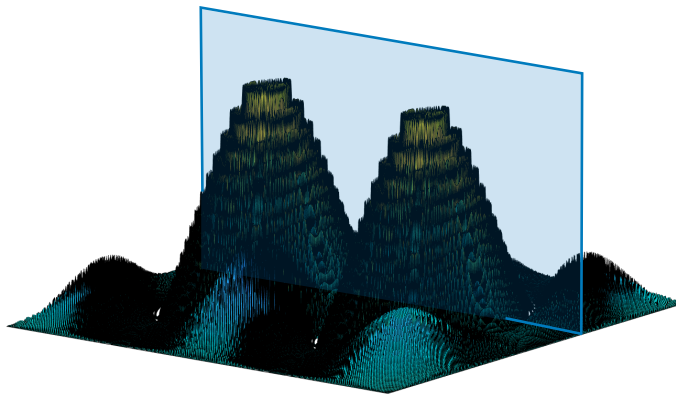

Figure 7.10.: Intensity distribution of two fringe patterns and a cut plane through the center of the patterns

It illustrates two fringe patterns where fringes are clearly recognizable as rings of a certain intensity level. The intensity distribution follows a Gaussian decay curve which is evident from the Point Spread Function (PSF) known from 2.3.2 Fringe Pattern vs. Fresnel Zone Plate. The delineated plane cuts both fringe patterns through its centers and indicates the reason why light pulses in light scattering systems cause Gaussian-shaped detection signals. Light scattering pulses are integrated over the light energy when captured by photodetectors and yield the envelope of intensity along the marked cut plane. Figure 7.11 clarifies this by comparing the imaged hologram (a) with the intensity distribution along the cut plane (b).
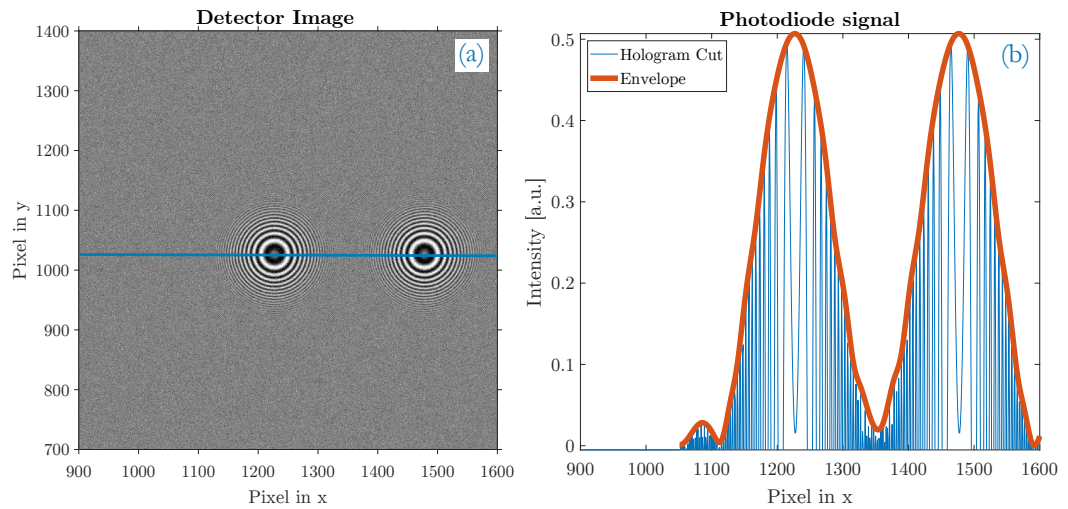
Figure 7.11.: (a) Modelled hologram with two fringe patterns and the cut plane through its centers;
(b) Intensity distribution along the cut plane and its envelope

The resulting envelope shows the same Gaussian behavior known from light pulse responses in flow-based counting units (Susanne V. Hering et al., 2005; Collins, Dick, and Romay, 2013). The relationship of the x- axis between the number of pixels in the graph and a time representation in time-based systems is simply the velocity of particles traversing the detector[1].

Coincidence in time-based counting appears when consecutive light pulse responses merge to a single peak due to their short time sequence of occurences. In an area-based system this means a close spatial location. Figure 7.12 demonstrates this coincidence in the area-based case (a) and the time-based impact (b). Whereas fringe patterns are still distinguishable, the time-based response merges to a single pulse and would lead to an incorrect interpretation of events. The only possible indication of time coincidence is provided in the signal shape and the deviating signal amplitude.

---

[1]The scale of pixel sizes as well as light pulse responses in time signals are in the μ- range. This results from particle velocities (in m/s) typically in the two-digit range.
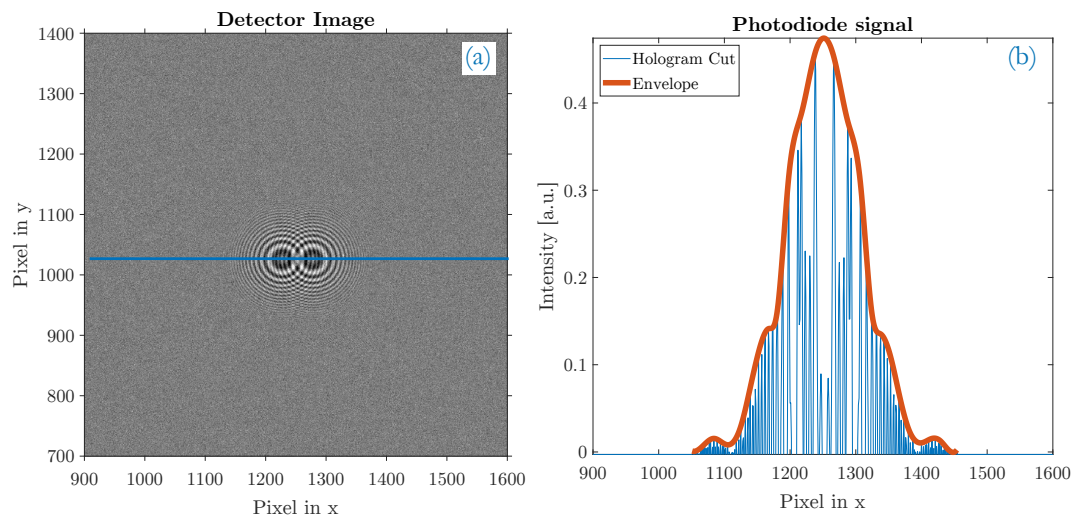
Figure 7.12.: Coincidence of two particles and the implications to area-based (a) and time-based detection;
(a) Modelled hologram with two fringe patterns and the cut plane through its centers; (b) Intensity distribution along the cut plane and its envelope

Coincidence originates from closely located particles in space and appears in time-based as well as in area-based detection systems. The relationship is the intensity distribution of light. Whereas an area-based detection faces an overlap of fringe patterns, time-based methods notice the merge of light pulse responses due to the integral of the intensity distribution (the envelope).

7.3.2. Dead Area vs. Lambert-W Correction in Area-based Detection

In order to determine the per event dead area A_d for all three detection methods an artificial fringe pattern is created with the Holographic Aerosol Particle Model. The size of the pattern is the average that is expectable from the geometries of the Particle Imaging Unit (as if a particle is located in the center of the cell). According to 4.3.4 Definition of Dead Area & Practical Approximations, a diameter of $\delta_d = 53\,pxl$ is found for the customized Hough Transform, $\delta_d = 43\,pxl$ for blob detection, and $\delta_d = 100\,pxl$ for the DCNN, respectively. In all cases this diameter is considered as the determining parameter, spanning a circular shaped *per event dead area* Ω. Figure 7.13 shows the trends of particle number concentration where in all plots the results are corrected by Dead Area Correction and the Lambert-W function.

- (a) customized Hough Transform
- (b) the blob detection with maximum entropy thresholding
- (c) DCNN based on a U-Net

Dead Area vs. Lambert-W Correction

In the lower concentration regions the correction effort is very low and the output of both correction methods equal[2]. At higher count rates the Dead Area Correction tends to underestimate due to its simple nature of deducting *live volume*. In contrast, the Lambert-W function is based on statistical correction and takes into account the rising probability of multiple hidden particles in a consistent sampling volume. At even higher count rates the effect of statistical correction outperforms the Dead Area Correction. Nevertheless, both methods classify as suitable coincidence correction means. The results also confirm the transferability from time-domain-based counting units to imaging-based units.

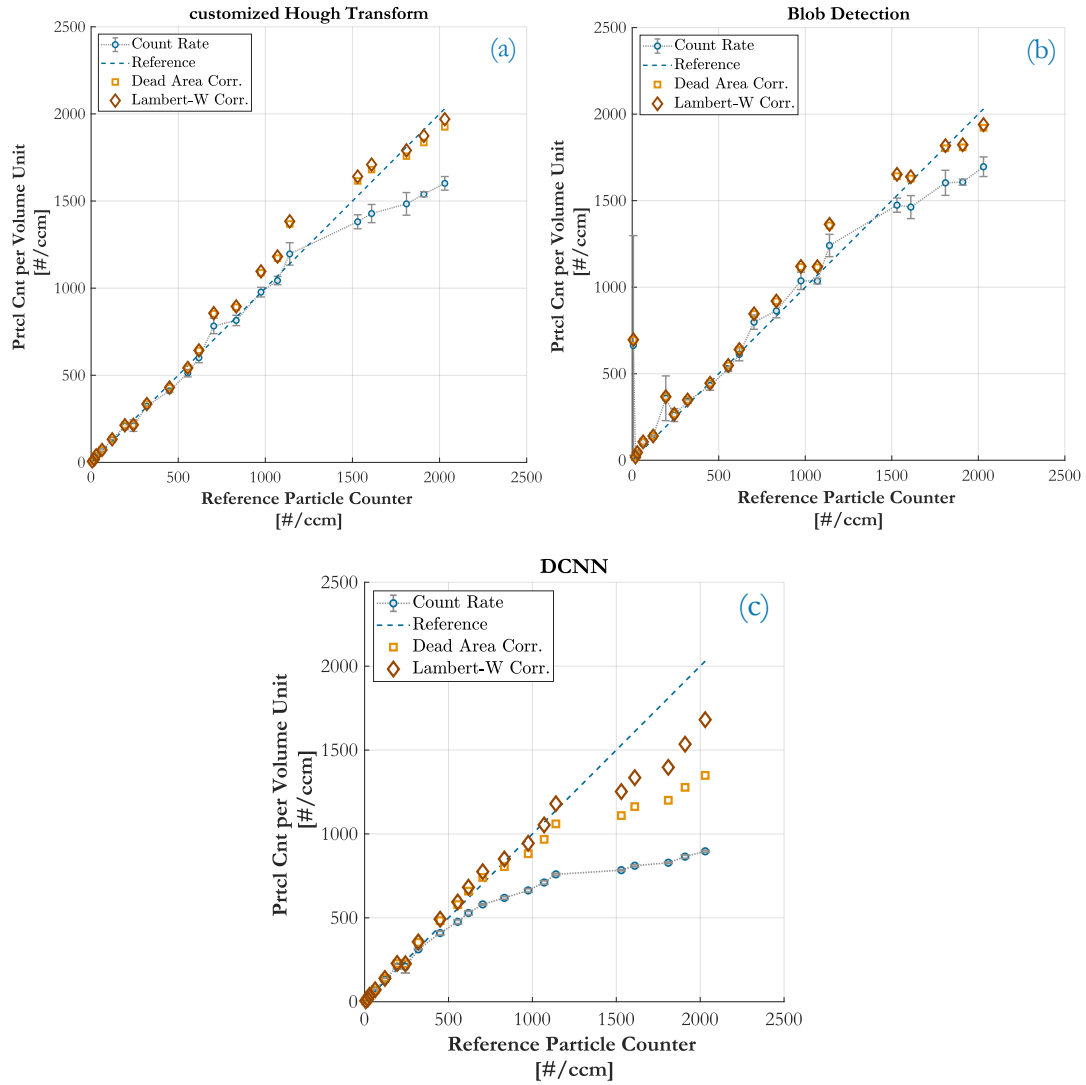[2]Outliers are of course exceptional cases were falsifications are even enhanced.

Figure 7.13.: Comparison of the monitored particle number concentration to the rates obtained by the PIU. The concentration is coincidence-corrected by *Dead Area* and *Lambert-W* correction. (a) for customized HT with $\delta_d = 53pxl$; (b) for blob detection with $\delta_d = 43pxl$; (c) for DCNN $\delta_d = 100pxl$

Details on the customized Hough Transform, blob detection & DCNN

Figure 7.13 also contrasts how the counting results of the customized Hough Transform, blob detection and DCNN are coincidence corrected. The course of the correction curves is based on the individual per event dead areas δ_d of all detection algorithms. While the DCNN does not yield promising counting results in any case, the coincidence corrected course of the customized Hough Transform and blob detection are in good accordance with the actual course of the Reference Particle Counter.
The curve of the DCNN is only trustworthy up to roughly $C_N = 1200 \, \#/cm^3$, for which the coincidence correction is perfectly conducted as well. Moreover, the curve flattens stronger than can be justified by the mere occurence of particle coincidences. Most probably, fringe patterns at the border of images are filtered too much or even vanish in the process of downsampling in the neural network and are therefore not detected. As described in 4.1.3 Deep Convolutional Neural Networks, every convolution step entails a loss of border pixels and may be the main reason for the flattening of the counting curve.

Aside from the special case of the DCNN, the results of coincidence correction proof that the determined per event dead area for all methods is reasonable.

8. Conclusion & Outlook

8.1. Summary

In automotive legislation, exhaust emission regulations become more and more stringent. The United Nations Economic Commission for Europe (UNECE) introduced the Regulation 83 (R83) addendum that specifically focuses on PN measurements. Altough a CPC is still the most widespread and acknowledged technology to determine particle number concentrations, various restrictions restrain a future-proof application. The state-of-the-art approach of optically detecting and counting particles is one restriction that was addressed in this thesis. The main goal was to investigate and develop an alternative counting solution to advance the technology of CPCs.
The holographic principle has already been proven by previous master theses to be a very promising technology to tackle the research questions, stated in 1.2.4 Research Questions. In-depth research on holography and its various application fields and optical setups revealed that Digital Inline Holography (DIH) is best suitable in terms of feasibility, complexity and effort, and at lowest costs.

A first focus was laid on the modelling of an in-line holographic detection approach of aerosol particles. The developed Holographic Aerosol Particle Model (HAPM) combines a numerical model of DIH with a multiphysics simulation tool. In this way, a multi-physics sensor model was accomplished that supports as designing tool for the development of a sophisticated holographic detection & counting unit, and building up an understanding of the interrelation of all relevant influences.

In a second step, the particles' interference patterns - so called fringe patterns - were invetigated to extract the most relevant features provided at the recorded detection- or hologram plane. It was found out that the circular

fringe patterns can be detected by simple 2-dimensional image processing means. Instead of typical 3D- backpropagation algorithms, common pattern recognition techniques are sufficient to detect and count particles at the 2D-hologram plane and even extract details on the full 3D position of particles, their size, shape and trajectories. With a customized Hough Transform (HT), a variant of blob detection and a Deep Convolutional Neural Networks (DCNN), three different pattern recognition techniques were customized, validated and compared in terms of detection performance of fringe patterns and computational speed. While model data generated from the HAPM aided the design of the methods, the validation and comparison was based on real measurement samples.

The third goal was to design and validate a novel Holographic Particle Counter. It is based on the HAPM. Introduced as Particle Imaging Unit (PIU), the counting unit is based on an in-line holographic arrangement comprising a laser, a sampling cell and a camera. The counting unit can be used to determine particle number concentrations of particle sizes that are in the lower μm- range. It resolves particles that are larger than roughly $3 - 4\mu m$ which corresponds to pixel size of the imager. It is applicable in various fields where e.g. particles, droplets, solids, cells or bubbles need to be detected, counted and analysed. As the presented concept is a direct and volume-based imaging system, no flow rate measurement is required which is especially advantageous over standard light scattering methods of CPCs. Particles in the sampling volume are detected all at once. The particle number concentration is inherently determined which makes it a simple and cheap standalone "single-particle" counting unit on the one side, but also a true "zero-particle" monitor.

All three pattern recognition algorithms were tested and show basic suitability as counting methods, though with different limitations and drawbacks. At particle densities up to $1000 \frac{\#}{ccm}$ the count response of the customized Hough Transform and blob detection are linear and make these counting approaches perfectly suited for precise low concentration monitoring. A solution based on a DCNN only works satisfactorily at lower particle rates of around $600 \frac{\#}{ccm}$ where only few overlaps of fringe patterns occur. At rising particle densities, the probability of particles coinciding in the sampling volume rises which lead to said fringe pattern overlaps at the hologram plane that inevitably reduce the detection performance of all methods. The result-

ing coincidence affected counting rates follow the same rules as time-based counting units of standard CPCs. Therefore, two coincidence correction methods were transferred to the 2-dimensional domain where its analogy to the time domain is shown and proven.

By taking coincidence correction into account, blob detection turns out to be the best method with respect to counting rates. The superior computational speed with constant processing times (even without GPU support) enable a RT application and makes it the best candidate for particle counters. The customized Hough Transform is more robust against noise and intensity fluctuations in images and shows slightly better precision at the detection of fringe patterns. The longer processing times, which vary as a function of particle rate, disqualifies it for practical use, however. The accuracy and detection performance of the DCNN may be increased by training with greater datasets and real measurement samples. Although this is a topic for further investigations, similarly high counting rates are difficult to achieve due to the high amount of different overlapping possibilities of fringe patterns. The requirement of a GPU is additionally disadvantageous over CPU-executable RT applications.

Since the total sampling volume of the PIU is scanned at once, an expansion of the volume may be realized to an arbitrary extent and thereby the range of measurable particle concentrations be linearly upscaled. The sensitivity of the system in single shot mode is about $4.16 \frac{\#}{ccm}$ and is easily increased by a factor of 20 and more by increasing the camera's frame rate or the overall sampling period.
A stroboscopic imaging approach was evaluated to further decrease the exposure time of the camera and reduce the disadvantageous effect of motion blurring during image acquisition. This principle allows higher aerosol flow rates through the sampling channel while preserving imaging quality. It coult be shown that flow rates up to $1.2\,l/min$ and more are possible, though with modifications required in the current conditioning concept of the PIU. Motion blur, however, is also useful to determine the speed of motion and direction of motion of particles in the sampling volume. The knowledge of the average aerosol flow speed provides a direct measure for volume flows and could be used for an integrated flow monitor.

8.2. Research Questions - answered

The research questions from 1.2.4 Research Questions can be answered as follows:

1. **What is an alternative solution to nozzle-based counting designs?**
   A light scattering arrangement is in fact a 0-D imaging apparatus which requires to focus on a specific focal point to map the scattered light onto a detector. Holography was invented to overcome such problems of limited Depth of Field (DoF) and enables the imaging of whole volumes. Hence, nozzles can be removed and a sampling volume of arbitrary extent can be imaged by holographic means.

2. **How could the probability of coincidence be reduced to measure higher particle concentrations?**
   The probability of coincidence is reduced by decreasing the particle density in a sampling volume. In other words, particles have to be distributed over a larger volume. The removal of the nozzle is therefore a major step. In an extended sampling volume, of course, particles may coincide as well. Nevertheless, coincidence is minimized when reducing the DoF and capturing over a larger sampling area instead.

3. **How could a real volume-based determination of particle number concentrations be achieved?**
   When particles are larger than the wavelength of the incident light (e.g. $d_{prt} > 4 - 5\lambda$), light passing the particles follow the rules of diffraction. An imaging system, where a detector acquires that forward diffracted fraction of light and the original light of the direct illumination beam is called an in-line holographic arrangement (provided that the light source is coherent). It is able to sense the entire illumination volume between the light source and the detector and inherently determines the particle number concentration of this sensed volume.

4. **Could the velocity of particles be minimized for the sake of a slower counting mechanism?**
   Removing the nozzle slows down the aerosol flow considerably, so the counting procedure may be slower. While nozzle-based designs

must detect all particles in a certain time period (and therefore be fast), Digital Inline Holography systems have to detect all particles in a volume at once. This requires powerful image processing algorithms in terms of detectability rather than computational speed. An accelerated image acquisition rather improves the dynamics and accuracy of the counting system. In DIH, slower particles are even preferred.

5. **Is it possible to detect lowest particle number concentrations while extending the measurement range to higher rates?**
   Results have shown that the developed Particle Imaging Unit is powerful at lowest particle concentrations and is applicable as a "zero-particle" monitor. At higher particle concentrations (for CPCs it's actually quite low) particle coincidence is still a limiting factor of the presented system. However, the sampling volume may be arbitrarily extended and multiple counting units be parallelized. Particle densities larger than $30.000\,\#/cm^3$ are principally achievable (see suggestions in Appendix C The Particle Imaging Unit). Based on the current study, however, a realisation is too expensive and therefore only of limited use.

6. **Could the quality of the condensation process be assessed by alternative and more accurate means?**
   The final size of condensed particles is a function of the saturation ration in the Condensation Nucleus Magnifier (CNM). Each individual droplet can be reconstructed from the recorded hologram. Consequently, a better traceability to the condensation process is achieved because the size, position and trajectory of the droplets is known. The developed PIU, however, has a size resolution of particles of roughly $3 - 4\,\mu m$ which is only slightly smaller than typical droplet sizes in CPCs ($\approx 3 - 7\,\mu m$). This is too poor to allow a meaningful sizing and requires modifications (i.e. as a microscopic setup).
   The intensity of the diffraction pattern is also a function of particle size and may be evaluated as well. Degrading or fluctuating pattern intensities are therefore another indicator of a deteriorating condensation process.

7. **Could particles/droplets be characterized in size, shape or morphology?**
In principle, the same applies as in the previous research question. A microscopic setup modification enables a more reliable sizing and particle characterization. As the morphology of particles or droplets was no topic in this thesis, further studies are necessary.

8. **Is particle/droplet sizing possible without static light scattering procedures and independent from the scattering angle?**
The diffracted light of particles provides all information to reconstruct the original object. Thus, no further viewing angles or moving scanning apparatuses are necessary.

9. **Are applications such as a Dual-Cutoff CPC or a Sizing CPC feasible?**
Because of traceability, a holographic imaging unit is principally capable of discriminating droplets and allocating them to their respective condensation chamber. In case droplets from either chamber are spatially clustered in front of the imaging unit, the simplest form of classification is the division of the detection plane into two sample zones, e.g.: left zone corresponds to channel A, right zone to channel B. Sizing-CPCs could follow the same principle that particles are preselected according to their size prior to the condensation and imaging process. The grown particles, still sorted by its original size, could then pass the detection plane which is divided into multiple size-zones. A droplet recognized in zone A belongs to a particle class of original size A and a droplet in zone B belongs to size class B.

10. **Could a counting unit be operated under harsh conditions, e.g. at hot temperatures?**
Imagers are semi-conductor based elements that allow a working temperature range of typically $0 - 55°C$. Hot environmental applications are therefore impossible. Holography, however, follows the rules of classic geometric optics wherefore Optical Elements (OEs), such as lenses or fibres are applicable to map the sampling volume to a "conditioned" environment for imaging.

8.3. Outlook

The developed Particle Imaging Unit was intentially designed to enable modular optical setups for experiments. Using Thorlabs- or customized mountings, imaging systems based on different light sources, detectors or lens systems can be realized. The sampling cell is closed with insertable window frames in the optical path which can be exchanged by different or heated windows, lenses or optical filters to provide best modurality and cleaning possibilities.

With this modularity, experiments like the following may be of interest in advanced studies:

- Variation of light sources:
    - different Lasers: a larger coherence length improves the contrast of holograms and allow higher quality pattern recognition (particle detection) and wavefront reconstruction (reconstruction of particles); e.g.: HeNe Laser
    - Light Emitting Diodes (LEDs): to check if their coherence length is sufficient to use in low-cost holograhpy imaging
    - LEDs: to determine their coherence lenght since diffration patterns only occur at sufficient light coherence
    - incoherent light: for shadow imaging
    - customized light source designs

- Variations in cell windowing:
    - ITO coated windows: prevent misted windows via heating
    - Lenses: to zoom-in of the sampling volume and improve imaging resolution for particle sizing and characterization (microscopic approach)
    - Lenses: to zoom-out of the sampling volume and increase the detectable particle rates (fringe patterns shrink and occupy less of the detection plane)

- Thermally decouple temperature sensitive elements and prepare for applications at hot temperatures (e.g. HT-CPC)
- Advanced data analyses:

  – at achieve a sophisticated particle characterization (e.g. *z*- position, particle size, particle speed)
  – of motion-blur for better estimations of the aerosol flow speed (e.g. as integrated flow meter)
  – of motion-blur to assess the aerosol flow field (e.g. as flow profiler)

The major drawback of the achieved modularity is the resulting leakage of the sampling cell. All experiments in this work were conducted in pressurized mode which is no option in standard CPCs. They operate in suction mode and therefore require a hermetically sealed counting unit. Hence, and in cooperation with the AVL internal segment MAE, a redesign of the sampling cell has been initiated and already completed in the epilogue of this thesis. The modified PIU will be utilized to support the development of a novel Dual-Cutoff CPC from AVL and will be implemented as an easy-to-replace counting unit. As the results of the thesis showed that the range of measureable particle number concentrations is too low for standard CPCs the PIU will be mainly used as a characterization and assessment tool.

In the future, a holographic counting unit could be used as a reference for the calibration of CPCs due to its traceability and direct measurement of particle concentrations without the need of measureing the flow rate. It may replace Static Light Scattering (SLS) apparatuses or serve as a reference sizing tool. Additionally, it is applicable in various other fields of particle-, droplet-, solid- or cell recognition, counting and characterization.

Appendix

Appendix A.

Digital Holography

A.1. Diffraction by a Particle

The three-dimensional scalar wave equation in Equation (2.6) on page 26 in extended form is:

$$\frac{\partial^2 \psi}{\partial x^2} + \frac{\partial^2 \psi}{\partial y^2} + \frac{\partial^2 \psi}{\partial z^2} = \frac{1}{v^2} \frac{\partial^2 \psi}{\partial t^2} \tag{A.1}$$

To find the field distribution $\psi_{prt}(x, y; z)$, as obtained on page 30, Equation (2.10) on page 28 is substituted into the above three dimensional scalar wave equation in Equation (A.1) to obtain the Helmholtz equation:

$$\frac{\partial^2 \psi_{prt}}{\partial x^2} + \frac{\partial^2 \psi_{prt}}{\partial y^2} + \frac{\partial^2 \psi_{prt}}{\partial z^2} + k_0^2 \psi_{prt} = 0 \tag{A.2}$$

$$\Big\Downarrow \quad \mathcal{F}\left\{ \frac{\partial^2 \psi_{prt}}{\partial x^2} , \frac{\partial^2 \psi_{prt}}{\partial x^2} \right\} \quad \Big\Downarrow$$

$$\frac{d^2 \Psi_{prt}}{dz^2} + k_0^2 \left(1 - \frac{k_x^2}{k_0^2} - \frac{k_y^2}{k_0^2} \right) \Psi_{prt} = 0 \tag{A.3}$$

To obtain the above solution, first the Fourier transform of $\mathcal{F}\left\{\psi_{prt}(x,y;z)\right\} = \Psi_{prt}(k_x,k_y;z)$ has to be made aware of to be:

$$\mathcal{F}\left\{\frac{\partial^2 \psi_{prt}}{\partial x^2}\right\} = (-jk_x)^2 \Psi_{prt}(k_x,k_y;z)$$

$$\mathcal{F}\left\{\frac{\partial^2 \psi_{prt}}{\partial y^2}\right\} = (-jk_y)^2 \Psi_{prt}(k_x,k_y;z) \tag{A.4}$$

where $\{k_x,k_y\}$ are the spatial radian frequencies in Fourier space. In a second step, Equation (A.4) is substituded into Equation (A.2) where the second term is brought to a notation of clearer physical meaning.

Recognizing that the solution of the differential equation of Equation (A.3) is the following:

$$\frac{d^2 y(z)}{dz^2} + a^2 y(z) = 0 \qquad \Rightarrow \qquad y(z) = y(0)e^{-jaz}$$

the final result is:

$$\Psi_{prt}(k_x,k_y;z) = \Psi_{prt0}(k_x,k_y) \cdot e^{-jk_0 z \sqrt{\left(1 - k_x^2/k_0^2 - k_y^2/k_0^2\right)}} \tag{A.5}$$

A.2. Fringe Pattern - The Hologram of a Particle

Derivation of Equation (2.18) on page 33:

$$\Psi(x,y) = |\Psi_r + \Psi_{prt}|^2 = (\Psi_r + \Psi_{prt}) \cdot (\Psi_r + \Psi_{prt})^*$$

$$= \left(A \cdot e^{-jk_0 z_{prt}} + e^{-jk_0 z_{prt}} \frac{jk_0}{2\pi z_{prt}} e^{-j\frac{k_0}{2z_{prt}}(x^2+y^2)} \right) \cdot$$

$$\left(A \cdot e^{jk_0 z_{prt}} + e^{jk_0 z_{prt}} \frac{-jk_0}{2\pi z_{prt}} e^{j\frac{k_0}{2z_{prt}}(x^2+y^2)} \right)$$

$$= A^2 + \left(\frac{k_0}{2\pi z_{prt}} \right)^2 - jA \frac{k_0}{2\pi z_{prt}} e^{j\frac{k_0}{2z_{prt}}(x^2+y^2)} + jA \frac{k_0}{2\pi z_{prt}} e^{-j\frac{k_0}{2z_{prt}}(x^2+y^2)}$$

$$= A^2 + \left(\frac{k_0}{2\pi z_{prt}} \right)^2 + A \frac{k_0}{2\pi z_{prt}} \left[\frac{1}{j} e^{j\frac{k_0}{2z_{prt}}(x^2+y^2)} - \frac{1}{j} e^{-j\frac{k_0}{2z_{prt}}(x^2+y^2)} \right]$$

$$= C_1 + C_2 \cdot sin \left(\frac{k_0}{2z_{prt}}(x^2 + y^2) \right) \tag{A.6}$$

$C_1 = A^2 + \left(\frac{k_0}{2\pi z_{prt}} \right)^2$ ... constant bias

$C_2 = A \frac{k_0}{\pi z_{prt}}$ ... Amplitude of the sine

A.2.1. Fringe Pattern vs. Fresnel Zone Plate

Derivation of Equation (2.24) on page 37 where the width dr_n of the nth zone is the derivative of the zones radius R_n with respect to n:

$$
\begin{aligned}
dr_n = \frac{d}{dn} R_n &= \frac{d}{dn} (n \cdot \lambda \cdot z_{prt})^{1/2} \\
&= \frac{1}{2} (n \cdot \lambda \cdot z_{prt})^{-1/2} \cdot \lambda \cdot z_{prt} \\
&= \frac{1}{2R_n} \lambda \cdot z_{prt} = \frac{1}{2R_n} \cdot \frac{R_n^2}{n} \\
dr_n &= \frac{R_n}{2n}
\end{aligned}
\tag{A.7}
$$

Remember Equation (2.21) on page 35 with $R_n \simeq \sqrt{n \cdot \lambda \cdot z_{prt}}$.

Appendix B.

The Holographic Aerosol Particle Model

In notation of the Matlab based model, the variables are translated as:

Table B.1.: Notation of variables in the model

Desciption	Variable	Model notation
Extend of object plane in:	x	xPlane
Extend of object plane in:	y	yPlane
Extend of object plane in:	z	zPlane
Resolution of object plane in:	$\{x, y\}$	xyRes
Amplitude of reference wave ψ_r	A or I	Intensity
Particle diameter	d_{prt}	d0
Size of detector in x	M	M_det
Size of detector in y	N	N_det
Pixel size in x	Δ_x	mPxlSize
Pixel size in y	Δ_y	nPxlSize
Wavelength of illumination source	λ	lambda
Number of particles	N_{prt}	nrPrtcl
System exposure time	τ	t_exp
Gaussian White noise (mean)	σ_n	noiseMean
Gaussian White noise (variance)	σ_n	noiseStd
Particle's direction of motion	$\phi(t)$	orient
Particle's speed of motion	$v_{prt}(t)$	v
Mode of particle generation/placement	–	typeLoc

Some further desciptions to function blocks (grouped variables in structs):

- `CoordMan`
  is for the manual placement of particles at the detection plane where coordinates are offset values (`xOffsPxl, yOffsPxl, zOffs`), relativ to the origin $\{0,0,0\}$. The origin is considered at the center of the sampling cell (z-axis) and centered at detection plane (x and y).
  The smallest number of elements in `xOffsPxl, yOffsPxl, zOffs` and `orient,v` determine the number manually generated particles.

- `DirMan`
  is for the manual definition of particles' movement with `orient` for the direction of motion and `v` for the speed of motion of every single, manually placed particle.
  The smallest number of elements in `xOffsPxl, yOffsPxl, zOffs` and `orient,v` determine the number of manually generated particles.

- `SizeMan.d0`
  is the diameter of particles. It determines the diameter for all particles when manually generated. An array of elements is not supported.

- `Det.origin`
  is necessary to align the origin of the detection plane (hence the PIU) to the COMSOL imported data coordinates. E.g.: The origin in COMSOL is at the bottom of the geometry. The center of the optical axis is in offset height of $y = 50.25\,mm$. The detection plane is located in a distance of $z = 7.18\,mm$ away from the sampling cell center. The final DoF is ranged between $z = 5.18 \ldots 9.18\,mm$, leading sampling cell depth of $4\,mm$.

- `Cell.Smpl`
  specifies the geometry of the simulated sampling cell. It is relevant when importing smulation data from COMSOL to align the coordinate systems of both the COMSOL environment and the simulated PIU.

- `Cell.Smpl.Geom`
  specifies the dimensions of the whole sampling cell (only cubic volume).

```matlab
%------------------------------------------------------------%
%%                Holographic  Aerosol  Particle  Model
%------------------------------------------------------------%
%
% Company:        AVL  List  GmbH
% Department:     ITS  /  TRN
% Author:         Georg  Brunnhofer ,  Msc
% Contact:        georg.brunnhofer@avl.com
% Date:           28.06.2016
% Last  Update:   10.05.2020
% Revision:       1.0
% -------------------------------------
% Toolbox:        Image  Processing  Toolbox
% -------------------------------------
% Description:  Generates  particle  holograms
%                   > place  multiple  particles:
%                       - manually
%                       - randomly
%                       - COMSOl  based
%------------------------------------------------------------%

%% load  Modules
addpath('HelperFunctions');
addpath('Modules/Objects');
addpath('Modules/WaveOptics');
addpath('Modules/Detector');
UNIT = getUnits();

%% Variables
Comsol.folder    = 'Comsol/ParticleMap/';
Comsol.filename  = 'HoloCell_ParticleMap_C=5000_v3.csv';

RUN_SIMLIST = 0;

%------------------------------------%
%- Reference  Wave                  -%
WaveRef.lambda       = 635 * UNIT.nm;
WaveRef.Intensity    = 1;

%------------------------------------%
%- Object  Plane                    -%
Obj.xyRes            = 1 * UNIT.um;
Obj.xPlane           = 8.473 * UNIT.mm;
Obj.yPlane           = 7.086 * UNIT.mm;
Obj.zPlane           = 4 * UNIT.mm;
```

Listing B.2: Code of HAPM (Page 2 of 3)

```matlab
%-----------------------------------%
%- Particle Dimensions             -%
Obj.typeLoc          = 'simFlow';
Obj.nrPrtcl          = 20;

%-----------------------------------%
%- Manual Particle Coordinates     -%
Obj.CoordMan.xOffsPxl = [0 200 400];
Obj.CoordMan.yOffsPxl = [0 0 0];
Obj.CoordMan.zOffs    = [0 0 0] * UNIT.mm;
Obj.DirMan.orient     = [0 0 0] * UNIT.deg;
Obj.DirMan.v          = [0 0 0] * UNIT.mps;
Obj.SizeMan.d0        = 3.45 * UNIT.um;

%-----------------------------------%
%- Detector                        -%
Det.mPixels          = 2456;
Det.nPixels          = 2054;
Det.mPxlSize         = 3.45 * UNIT.um;
Det.nPxlSize         = 3.45 * UNIT.um;
Det.t_exp            = 56.0 * UNIT.us;
Det.noiseMean        = 0.005;
Det.noiseStd         = 0.005;
Det.origin           = [0 50.25 7.18] *UNIT.mm;

Cell.origin           = [0 0 0] * UNIT.mm;
Cell.Smpl.origin      = [0 50.65 0] * UNIT.mm;
Cell.Smpl.Geom.xdim   = 10 * UNIT.mm;
Cell.Smpl.Geom.ydim   = 24.6 * UNIT.mm;
Cell.Smpl.Geom.zdim   = 4 * UNIT.mm;
Cell.Det              = Det;

Obj.DirMan.mPxlSize  = Det.mPxlSize;
Obj.DirMan.nPxlSize  = Det.nPxlSize;
Obj.DirMan.t_exp     = Det.t_exp;
Obj.DirMan.lambda    = WaveRef.lambda;
Obj.DirMan.zOrigin   = Det.origin(3);

%% Calculations
Obj.CoordMan.xOffs = Obj.CoordMan.xOffsPxl * Det.mPxlSize;
Obj.CoordMan.yOffs = Obj.CoordMan.yOffsPxl * Det.nPxlSize;
Det.origin         = Cell.origin + [0 0 Det.origin(3)];
```

```matlab
%------------------------------------%
%- Import Particles from COMSOL      -%
Comsol.path = [Comsol.folder Comsol.filename];
Obj.Sim     = importObjPlanePrtclMap(Comsol.path , Cell);

%------------------------------------%
%-  Create Holograms                 -%
Obj    = initObj2(Obj);
WaveObj = computeObjectWave2(WaveRef , Obj , Det);
Holo    = computeHologram2(WaveRef , WaveObj);
Holo    = computeCCD(Holo , Det);

%% Plot
figure;
imshow(Holo.trnsfct_n)
view([-90 90]); axis on
formatPlot2pub('title'      , 'Holographic Aerosol Particle
    Model',...
               'name'       , 'HAPM'                 ,...
               'xlabel'     , 'Pixel in y'           ,...
               'ylabel'     , 'Pixel in x'           ,...
               'clabel'     , 'Intensity [a.u.]')
```

Supported simulation modes:

- `manual`
  generation of manually positioned particles according to the function blocks of `CoordMan`, `DirMan` and `SizeMan.d0`. The number of modelled particles is determined by the smallest number of elements in function blocks.

- `normFlow`
  randomly positioned particles with the assumption of a normally distributed aerosol flow. The speed and direction of motion of all particles is random as well (uniformly distributed) and the maximum values are set with the first elements of `DirMan.orient` and `DirMan.v`. The number of modelled particles is determined by `Obj.nrPrtcl`.

- `randPos`
  randomly positioned particles with $z_{offs} = 0$ for all particles (uniformly distributed). The speed and direction of motion of all particles is 0. The number of modelled particles is determined by `Obj.nrPrtcl`.

- `randAll`
  randomly positioned particles $\{x, y, z\}$ with random speed and direction of motion (all uniformly distributed) and the maximum values are set with the first elements of `DirMan.orient` and `DirMan.v`. The number of modelled particles is determined by `Obj.nrPrtcl`.

- `simFlow`
  particles are positioned and characterized according to COMSOL simulations (including particle diameter). The number of modelled particles is determined by `Obj.nrPrtcl`.

- `simFlowRand`
  particles are positioned and characterized according to COMSOL simulations (including particle diameter) and additionally randomized (reasoned in older COMSOL simulations where no random particle generation was possible). The number of modelled particles is determined by `Obj.nrPrtcl`.

Appendix C.

The Particle Imaging Unit

The sampling volume can be reasonably enhanced by increasing the width x_{ch} of the sampling volume. As proposed in Figure C.2, multiple Particle Imaging Units (PIUs) could be stacked horizontally and in alternating order (packaging reasons) to increase the measurement range.
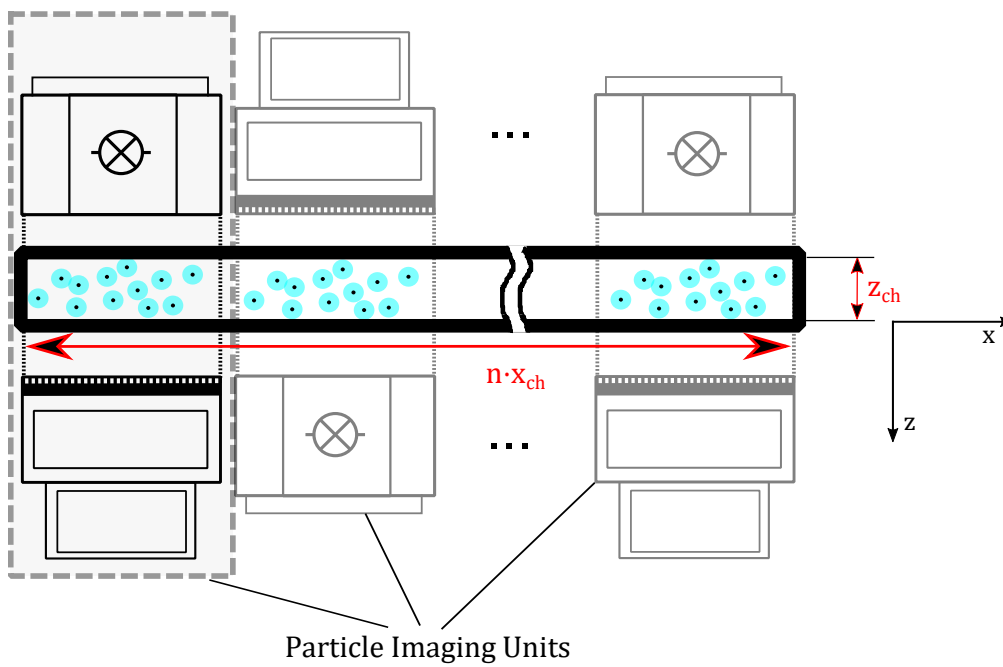

Figure C.1.: Arrangement of multiple horizontally stacked PIUs in alternating order

In addition to horizontal expansions, a Dual-PIU alignment may improve the dynamics of the imaging system. While one imaging pair is capturing a new measurement frame the other may be executing the detection of particles from the previous frame. A combined system may look like in Figure C.2.
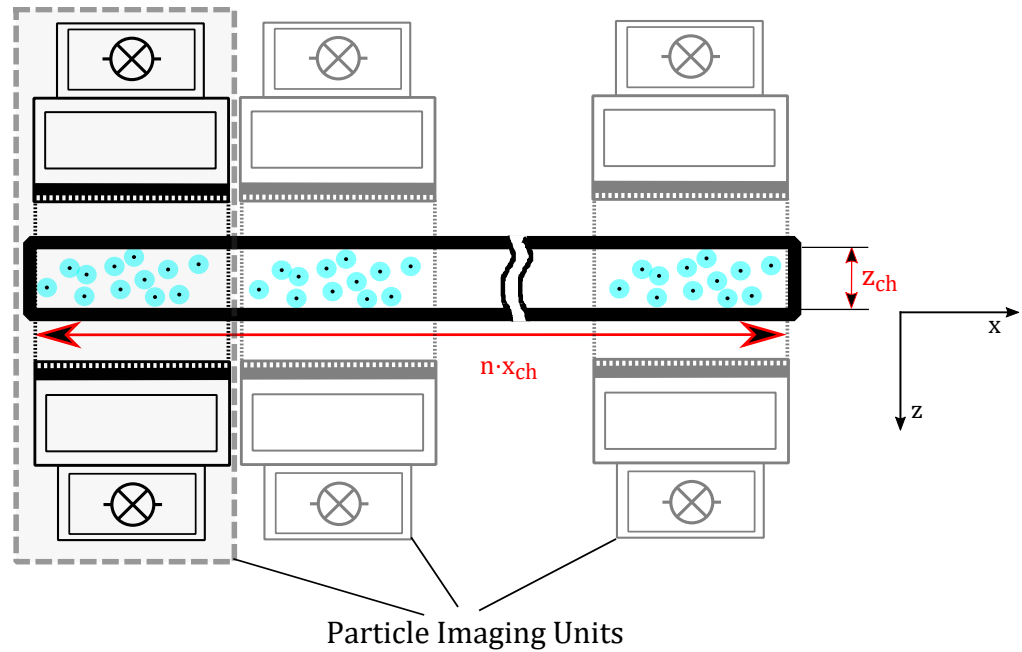

Particle Imaging Units

Figure C.2.: Arrangement of multiple horizontally stacked Dual-PIUs

Appendix D.

Experiments in the Lab

The Graphical User Interface of the MATLAB® App, mentioned in 6.2.1 DAQ of Measurement Samples is depicted below.
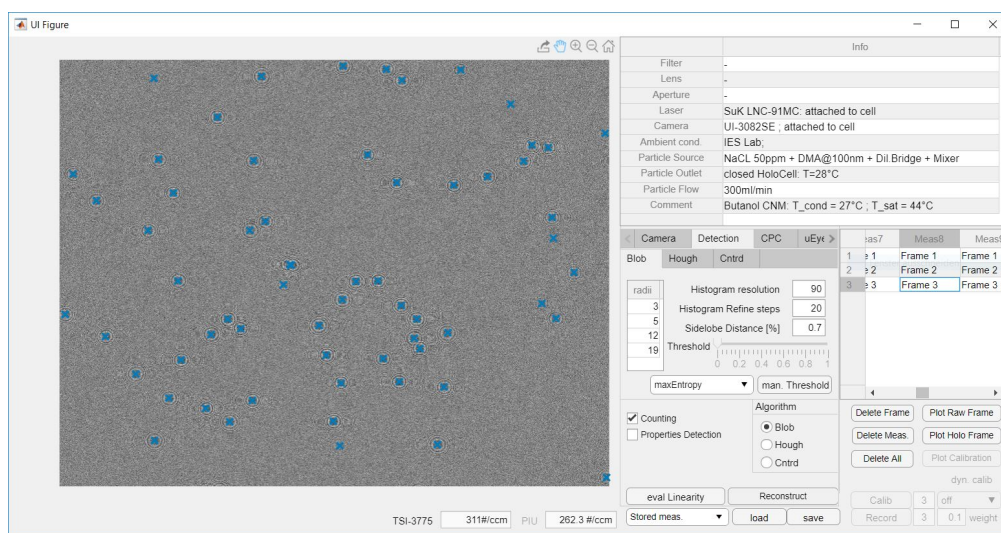

Figure D.1.: MATLAB® App to acquire and manage measurement data

It interfaces and controls the camera as well as a reference CPC - here: a TSI-3775. It stores, manages and displays measurement frames and executes the developed particle detection algorithms. Furthermore, a reconstruction function of particles from 4.2.2 Reconstruction of the Object Plane and a first estimation of 4.2.4 Particle Trajectories is integrated.

Publications

Peer Reviewed Conference Contributions

- Georg Brunnhofer, Alexander Bergmann, and Martin Kraft (2017). "Concept for a holographic particle counter." In: *30th Annual Conference of the IEEE Photonics Society, IPC 2017* 2017-Janua, pp. 581–582. DOI: 10.1109/IPCon.2017.8116233
- Georg Brunnhofer and Alexander Bergmann (2018). "Modelling a Holographic Particle Counter." In: *Proceedings, 2018, Eurosensors 2018* 2.13, p. 967. DOI: 10.3390/proceedings2130967
- Georg Brunnhofer (2018). "Concept for Holographic Particle Detection." In: University of Cambridge. Cambridge, UK: Cambridge Particle Meeting. URL: www.cambridgeparticlemeeting.org

Peer Reviewed Journal Papers

- Georg Brunnhofer, Alexander Bergmann, Andreas Klug, et al. (2019). "Design & Validation of a Holographic Particle Counter." In: *MDPI Sensors* 19.22, p. 19. DOI: 10.3390/s19224899. URL: https://www.mdpi.com/1424-8220/19/22/4899
- G. Brunnhofer et al. (2020). "A Comparison of Different Counting Methods for a Holographic Particle Counter: Designs, Validations and Results." In: *MDPI Sensors* 20.10, p. 19. DOI: 10.3390/s20103006

Issued Patent

- Georg Brunnhofer, Andreas Bergmann, et al. (2019). "Messvorrichtung und Verfahren zur Detektion von flüssigen und/oder festen Teilchen eines Fluidstroms." A 505043/2019

Bibliography

AG, Stemmer Imaging (2016). *CCD or CMOS : can CMOS sensors replace CCDs in all cases ?* Tech. rep. URL: https://www.stemmer-imaging.com/media/uploads/cameras/avt/de/de-Allied-Vision-WhitePaper-CCD-vs-CMOS-0416-KAVTO115-201604.pdf (cit. on pp. 101, 106).

"AlSi10Mg-0403 powder for additive manufacturing" (2015). URL: https://resources.renishaw.com/en/details/data-sheet-alsi10mg-0403-200-w-powder-for-additive-manufacturing--73121 (cit. on p. 95).

Arndt, Last (2016). *www.x-ray-optics.de*. URL: http://www.x-ray-optics.de/index.php/en/types-of-optics/diffracting-optics/fresnel-zone-plates (visited on 12/11/2019) (cit. on pp. 37, 67).

Atherton, T J and D J Kerbyson (1993). "Using phase to represent radius in the coherent circle Hough transform." In: *IEE Colloquium on Hough Transforms* Yuen 1990, pp. 1–4. URL: https://ieeexplore.ieee.org/stamp/stamp.jsp?tp=%7B%5C&%7Darnumber=243198 (cit. on p. 66).

Atherton, T.J. and D.J. Kerbyson (1999). "Size invariant circle detection." In: *Image and Vision Computing* 17.11, pp. 795–803. ISSN: 02628856. DOI: 10.1016/S0262-8856(98)00160-7. URL: http://linkinghub.elsevier.com/retrieve/pii/S0262885698001607 (cit. on p. 66).

Attwood, David and Anne Sakdinawat (2017). *X-Rays and Extreme Ultraviolet Radiation: Principles and Applications*. 2nd ed. Cambridge: Cambridge University Press. ISBN: 9781107062894. DOI: DOI:10.1017/CBO9781107477629. URL: https://www.cambridge.org/core/books/xrays-and-extreme-ultraviolet-radiation/8909199B5EDEDE542FCD1EBDD829D47C (cit. on pp. 34, 35, 37).

Axmann, Harald (2014). "Verfahren zur Bestimmung der Partikelkonzentration in Abgasen von Verbrennungsmotoren." PhD Thesis. Graz University of Technology (cit. on p. 6).

Bainschab, Markus and Alexander Bergmann (2018). "An Intrinsically Pressure Insensitive Low Cost Particle Number Diluter Featuring Flow Monitoring." In: *Proceedings* 2.13, p. 981. ISSN: 2504-3900. DOI: `10.3390/proceedings2130981` (cit. on p. 117).

Baron, P A and K Willeke (2005). *Aerosol Measurement: Principles, Techniques, and Applications*. Wiley. ISBN: 9780471784920 (cit. on pp. 2, 4).

Berg, Matthew J. et al. (2017). "Solving the inverse problem for coarse-mode aerosol particle morphology with digital holography." In: *Scientific Reports* 7.1, pp. 1–9. ISSN: 20452322. DOI: `10.1038/s41598-017-09957-w`. URL: `http://dx.doi.org/10.1038/s41598-017-09957-w` (cit. on pp. 13, 65, 76).

Bohren, Craig F and Donald R Huffman (2008). *Absorption and scattering of light by small particles*. John Wiley & Sons. ISBN: 3527618163 (cit. on p. 32).

Brunnhofer, G. et al. (2020). "A Comparison of Different Counting Methods for a Holographic Particle Counter: Designs, Validations and Results." In: *MDPI Sensors* 20.10, p. 19. DOI: `10.3390/s20103006` (cit. on pp. 65, 125, 173).

Brunnhofer, Georg (Feb. 2017). "Verfahren und Vorrichtung zur Detektion von Signalpulsen." WO2017025619A1 (cit. on p. 6).

Brunnhofer, Georg (2018). "Concept for Holographic Particle Detection." In: University of Cambridge. Cambridge, UK: Cambridge Particle Meeting. URL: `www.cambridgeparticlemeeting.org` (cit. on p. 173).

Brunnhofer, Georg and Alexander Bergmann (2018). "Modelling a Holographic Particle Counter." In: *Proceedings, 2018, Eurosensors 2018* 2.13, p. 967. DOI: `10.3390/proceedings2130967` (cit. on p. 173).

Brunnhofer, Georg, Alexander Bergmann, Andreas Klug, et al. (2019). "Design & Validation of a Holographic Particle Counter." In: *MDPI Sensors* 19.22, p. 19. DOI: `10.3390/s19224899`. URL: `https://www.mdpi.com/1424-8220/19/22/4899` (cit. on pp. 82, 89, 111, 125, 173).

Brunnhofer, Georg, Alexander Bergmann, and Martin Kraft (2017). "Concept for a holographic particle counter." In: *30th Annual Conference of the IEEE Photonics Society, IPC 2017* 2017-Janua, pp. 581–582. DOI: `10.1109/IPCon.2017.8116233` (cit. on p. 173).

Brunnhofer, Georg, Andreas Bergmann, et al. (2019). "Messvorrichtung und Verfahren zur Detektion von flüssigen und/oder festen Teilchen eines Fluidstroms." A 505043/2019 (cit. on p. 174).

Buchberger, Anton (2015). "Statische Lichtstreuung an Aerosolen." Bachelor Thesis. Graz University of Technology (cit. on p. 6).

Center for X-Ray Optics (2014). *Fresnel zone plate theory, generation, tolerancing, fabrication, and applications*. URL: http://zoneplate.lbl.gov/theory (visited on 06/19/2018) (cit. on p. 37).

Collier, Robert, Christoph B. Burckhardt, and Lawrence H. Lin (1971). *Optical holography*. New Jersey: Academic Press. ISBN: 0323144306 (cit. on p. 18).

Collins, Aaron M., William D. Dick, and Francisco J. Romay (2013). "A New Coincidence Correction Method for Condensation Particle Counters." In: *Aerosol Science and Technology* 47, pp. 177–182. DOI: 10.1080/02786826.2012.737049. URL: https://www.tandfonline.com/doi/pdf/10.1080/02786826.2012.737049?needAccess=true (cit. on pp. 7, 82, 84, 144).

Cresnoverh, Martin (2015). "Realisation of a visual based condensation particle counter utilizing bright field technique." Master Thesis. Graz University of Technology (cit. on pp. 3, 6, 12, 13, 89).

David, Grégory et al. (2018). "Digital holography of optically-trapped aerosol particles." In: *Communications Chemistry* 1.1, pp. 1–9. DOI: 10.1038/s42004-018-0047-6 (cit. on p. 13).

Dixon, Lisa, Fook Chiong Cheong, and David G Grier (2011). "Holographic particle-streak velocimetry." In: 19.5, pp. 4393–4398 (cit. on pp. 49, 52, 53).

Duda, Richard O. and Peter E. Hart (1972). "Use of the Hough transformation to detect lines and curves in pictures." In: *Communications of the ACM* 15.1, pp. 11–15. ISSN: 00010782. DOI: 10.1145/361237.361242 (cit. on p. 65).

ELas (2018). *CA-1620 Holography*. Tech. rep. Buggingen: eLas educational Lasers. URL: https://www.e-las.com/de/produkte/optik-grundlagen/ca-1620-holographie/ (cit. on p. 19).

Em Segmentation Challenge (2012). \url{https://imagej.net/2011-10-25_-_-EM_segmentation_challenge_(ISBI_-_2012)} (cit. on p. 74).

Falgout, Zachary, Yi Chen, and Daniel R. Guildenbecher (2019). "Improving the spatial dynamic range of digital inline particle holography." In: *Applied Optics* 58.5, A65. ISSN: 1559-128X. DOI: 10.1364/ao.58.000a65 (cit. on p. 137).

Falk, Patrick (2014). "A visual-based particle counter : simulation and design." Master Thesis. Graz University of Technology (cit. on pp. 11, 89, 97).

Gabor, Dennis (1948). "A new microscopic principle." In: *Nature Publishing Group*. ISSN: 0028-0836 (cit. on p. 15).

Giechaskiel, Barouch et al. (2014). "Review of motor vehicle particulate emissions sampling and measurement: From smoke and filter mass to particle number." In: *Journal of Aerosol Science* 67, pp. 48–86. ISSN: 00218502. DOI: 10.1016/j.jaerosci.2013.09.003. URL: http://dx.doi.org/10.1016/j.jaerosci.2013.09.003 (cit. on p. 2).

Gire, J. et al. (2008). "Digital holography of particles: Benefits of the 'inverse problem' approach." In: *Measurement Science and Technology* 19.7. ISSN: 13616501. DOI: 10.1088/0957-0233/19/7/074005 (cit. on pp. 43, 48, 65, 76).

Girshick, Ross et al. (2012). "Rich feature hierarchies for accurate object detection and semantic segmentation." In: pp. 2–9 (cit. on p. 72).

Gonzalez, C. Rafael (University of Tennessee) and E. Richard (MedData Interactive) Woods (2001). *Digital image processing*. Second Edi. Prentice Hall International, p. 793. ISBN: 0201180758 (cit. on pp. 34, 56, 72, 78).

Haralick, Robert M and Linda G Shapiro (1985). "Image segmentation techniques." In: *Computer Vision, Graphics, and Image Processing* 29.1, pp. 100–132. ISSN: 0734-189X. DOI: https://doi.org/10.1016/S0734-189X(85)90153-7. URL: http://www.sciencedirect.com/science/article/pii/S0734189X85901537 (cit. on pp. 71, 80, 81).

Heim, Michael et al. (2008). "Performance evaluation of three optical particle counters with an efficient "multimodal" calibration method." In: *Journal of Aerosol Science* 39.12, pp. 1019–1031. ISSN: 0021-8502. DOI: https://doi.org/10.1016/j.jaerosci.2008.07.006. URL: http://www.sciencedirect.com/science/article/pii/S0021850208001365 (cit. on p. 2).

Hering, Susanne V. et al. (2005). "A laminar-flow, water-based condensation particle counter (WCPC)." In: *Aerosol Science and Technology* 39.7, pp. 659–672. ISSN: 02786826. DOI: 10.1080/02786820500182123 (cit. on pp. 82, 83, 144).

Hering, Susanne V et al. (2007). "A Laminar-Flow , Water-Based Condensation Particle Counter (WCPC) A Laminar-Flow , Water-Based Condensation Particle Counter (WCPC)." In: 6826. DOI: 10.1080/02786820500182123 (cit. on p. 7).

Hinds, W C (2012). *Aerosol Technology: Properties, Behavior, and Measurement of Airborne Particles*. Wiley. ISBN: 9781118591970. URL: https://books.google.at/books?id=qIkyjPXfWK4C (cit. on p. 2).

Hinsch, K. D. (2002). "Holographic particle image velocimetry." In: *Meas. Sci. Technol. 13* 13, pp. 61–72. ISSN: 0957-0233. DOI: 10.1088/0957-0233/15/4/E01 (cit. on p. 13).

IDS Imaging Development Systems GmbH (2018). *UI-3082SE-M (AB00990)*. Tech. rep. Obersulm: IDS Imaging Development Systems GmbH, p. 2 (cit. on p. 106).

IHMA (2019). *About Holography: History*. URL: https://www.ihma.org/history.aspx (visited on 08/19/2019) (cit. on p. 16).

Jaenicke, R and H J Kanter (1976). *Direct Condensation Nuclei Counter With Automatic Photographic Recording, and General Problems of 'Absolute' Counters*. DOI: 10.1175/1520-0450(1976)015<0620:DCNCWA>2.0.CO;2. URL: Direct%20Condensation%20Nuclei%20Counter%20with%20Automatic%20Photographic%20Recording,%20and%20General%20Problems%20of%20%E2%80%9CAbsolute%E2%80%9D%20Counters (cit. on p. 11).

Jayanthi, N and S Indu (2016). "Comparison of image matching techniques." In: *International Journal of Latest Trends in Engineering and Technology* 7.3, pp. 396–401. DOI: 10.21172/1.73.552 (cit. on p. 69).

Jeong, Tung H (2008). "Basic Principles and Applications of Holography." In: *Fundamentals of Photonics*. Ed. by Handrasekhar Roychoudhuri. Illinois. Chap. Basic Prin, pp. 381–417. ISBN: 9780819471284. DOI: DOI:10.1117/3.784938.ch10. URL: https://spie.org/Documents/Publications/00%20STEP%20Module%2010.pdf (cit. on pp. 17, 19).

Jia, Yangqing et al. (2014). "Caffe: Convolutional architecture for fast feature embedding." In: *MM 2014 - Proceedings of the 2014 ACM Conference on Multimedia* May 2016, pp. 675–678. DOI: 10.1145/2647868.2654889. arXiv: 1408.5093 (cit. on p. 73).

Junge, C (1935). "Neuere Untersuchungen an der Grossen Atmospharischen Kondensationskerne." In: *Meteorol. Z* 52, pp. 467–470 (cit. on p. 11).

Kapur, J N, P K Sahoo, and A K C Wong (1985). "A new method for gray-level picture thresholding using the entropy of the histogram." In: *Computer Vision, Graphics, and Image Processing* 29.3, pp. 273–285. ISSN: 0734-189X. DOI: https://doi.org/10.1016/0734-189X(85)90125-2. URL: http://www.sciencedirect.com/science/article/pii/0734189X85901252 (cit. on pp. 70, 71).

Kaspers, Anna (2009). "Blob Detection." Master Thesis. Utrecht: UMC Utrecht, p. 14. URL: https://dspace.library.uu.nl/handle/1874/204781 (cit. on p. 69).

Kassner Jr, J L et al. (1968). "Expansion cloud chamber technique for absolute Aitken nuclei counting." In: *J. Rech. Atmos* 3, pp. 45–51 (cit. on p. 11).

Kerker, Milton (1997). "Light scattering instrumentation for aerosol studies: An historical overview." In: *Aerosol Science and Technology* 27.4, pp. 522–540. ISSN: 15217388. DOI: 10.1080/02786829708965492. URL: https://www.tandfonline.com/doi/pdf/10.1080/02786829708965492 (cit. on p. 2).

Kittler, J and J Illingworth (1985). "On threshold selection using clustering criteria." In: *IEEE Transactions on Systems, Man, and Cybernetics* SMC-15.5, pp. 652–655. ISSN: VO - SMC-15. DOI: 10.1109/TSMC.1985.6313443. URL: https://ieeexplore.ieee.org/stamp/stamp.jsp?tp=%7B%5C&%7Darnumber=6313443 (cit. on p. 69).

Kong, Hui, Hatice Cinar Akakin, and Sanjay E. Sarma (2013). "A generalized laplacian of gaussian filter for blob detection and its applications." In: *IEEE Transactions on Cybernetics* 43.6, pp. 1719–1733. ISSN: 21682267. DOI: 10.1109/TSMCB.2012.2228639 (cit. on pp. 67, 69).

Krizhevsky, Alex, Ilya Sutskever, and Geoffrey E Hinton (2012). "Imagenet classification with deep convolutional neural networks." In: *Advances in neural information processing systems*, pp. 1097–1105. URL: http://papers.nips.cc/paper/4824-imagenet-classification-with-deep-convolutional-neural-networ (cit. on p. 73).

Kuang, Chongai et al. (2012). "Modification of laminar flow ultrafine condensation particle counters for the enhanced detection of 1 nm condensation nuclei." In: *Aerosol Science and Technology* 46.3, pp. 309–315. ISSN: 02786826. DOI: 10.1080/02786826.2011.626815 (cit. on p. 4).

Kupper, Martin (2019). "Harsh Environment Particle Sensing." PhD Thesis. Graz University of Technology, p. 196 (cit. on pp. 6, 10).

LeCun, Y et al. (Dec. 1989). "Backpropagation Applied to Handwritten Zip Code Recognition." In: *Neural Computation* 1.4, pp. 541–551. ISSN: 0899-7667. DOI: 10.1162/neco.1989.1.4.541. URL: https://doi.org/10.1162/neco.1989.1.4.541 (cit. on p. 72).

Lee, H and R -. Park (1990). "Comments on "An optimal multiple threshold scheme for image segmentation." In: *IEEE Transactions on Systems, Man, and Cybernetics* 20.3, pp. 741–742. ISSN: VO - 20. DOI: 10.1109/21.57290.

URL: https://ieeexplore.ieee.org/stamp/stamp.jsp?tp=%7B%5C&
%7Darnumber=57290 (cit. on p. 69).

Lindeberg, Tony (1993). "Detecting salient blob-like image structures and their scales with a scale-space primal sketch: A method for focus-of-attention." In: *International Journal of Computer Vision* 11.3, pp. 283–318. ISSN: 09205691. DOI: 10.1007/BF01469346 (cit. on p. 69).

Maierhofer, Paul et al. (2019). "On the Inherent Variability of Particulate Matter Concentrations on Small Scales and the Consequences for Miniaturized Particle Sensors." In: *Aerosol and Air Quality Research*, pp. –. DOI: 10.4209/aaqr.2019.01.0048. URL: https://doi.org/10.4209/aaqr.2019.01.0048 (cit. on p. 9).

Malek, M et al. (2004). "Digital in-line holography for three-dimensional–two-components particle tracking velocimetry." In: *Measurement Science and Technology* 15.4, pp. 699–705. ISSN: 0957-0233. DOI: 10.1088/0957-0233/15/4/012. URL: http://dx.doi.org/10.1088/0957-0233/15/4/012 (cit. on pp. 65, 76).

Meng, Hui et al. (1993). "Intrinsic speckle noise in in-line particle holography." In: *Journal of the Optical Society of America A* 10.9, p. 2046. ISSN: 1084-7529. DOI: 10.1364/JOSAA.10.002046 (cit. on p. 40).

Mie, Gustav (1908). "Beiträge zur Optik trüber Medien, speziell kolloidaler Metallösungen." In: *Annalen der physik* 330.3, pp. 377–445. ISSN: 0003-3804 (cit. on p. 2).

Murata, Shigeru and Norifumi Yasuda (2001). "Potential of digital holography in particle measurement." In: 32.2000, pp. 567–574 (cit. on pp. 65, 76, 77).

Official Journal of the European Union, EN (2011). "Uniform Provisions Concerning the Approval of Vehicles with Regard to the Emission of Pollutants According to Engine Fuel Requirements." In: *UN ECE Regulation No 83* E/ECE/324/Rev.1/Add.82/Rev.4, p. 253 (cit. on p. 7).

Øgendal, Lars (2016). "Light Scattering a brief introduction." In: *University of Copenhagen* February, pp. 3–4 (cit. on p. 7).

Olomagic (2017). *How holographic display is used?* URL: https://www.olomagic.com/how-holographic-display-is-used/ (visited on 10/12/2019) (cit. on p. 19).

Pan, G. and Hui Meng (2001). "Digital In-line Holographic PIV for 3D Particulate Flow Diagnostics." In: *DLR-Mitteilung* 3, pp. 611–617. ISSN: 14348462 (cit. on pp. 65, 76).

Poon, Ting-Chung and Jung-Ping Liu (2014). *Introduction to Modern Digital Holography*. Cambridge University Press, p. 223. ISBN: 9781107016705. DOI: 10.1017/CBO9781107415324.004. arXiv: arXiv:1011.1669v3 (cit. on pp. 19, 25, 29, 34, 37, 41, 48, 76).

Potmesil, Michael and Indranil Chakravarty (2005). "Modeling motion blur in computer-generated images." In: *ACM SIGGRAPH Computer Graphics* 17.3, pp. 389–399. ISSN: 00978930. DOI: 10.1145/964967.801169 (cit. on pp. 55, 56).

Ronneberger, O, P Fischer, and TU-net Brox (2015). "Convolutional networks for biomedical image segmentation." In: *International Conference on Medical Image Computing and Computer-Assisted Intervention2015*. Springer, pp. 234–241 (cit. on p. 73).

Schäfter + Kirchhoff GmbH (2014). *Low Noise Laser Diode Modules LNC-Series*. Tech. rep. Hamburg, p. 1. URL: https://www.sukhamburg.com/produkte/LD-KollimatorLNC91CR.html (cit. on p. 98).

Sezgin, Mehmet and Bülent Sankur (Jan. 2004). "Survey over image thresholding techniques and quantitative performance evaluation." In: *Journal of Electronic Imaging* 13.1, pp. 146–165. URL: https://doi.org/10.1117/1.1631315 (cit. on p. 70).

Simonyan, Karen and Andrew Zisserman (2014). "Two-stream convolutional networks for action recognition in videos." In: *Advances in neural information processing systems*. simonyan2014, pp. 568–576. URL: http://papers.nips.cc/paper/5353-two-stream-convolutional (cit. on p. 73).

Song, Jun et al. (2016). "Sparsity-Based Pixel Super Resolution for Lens-Free Digital In-line Holography." In: *Scientific Reports* 6.April, p. 24681. ISSN: 2045-2322. DOI: 10.1038/srep24681. URL: http://www.nature.com/articles/srep24681 (cit. on p. 78).

Sonka, Milan, Vaclav Hlavac, and Roger Boyle (2014). *Image processing, analysis, and machine vision*. Cengage Learning. ISBN: 1133593607 (cit. on pp. 69, 71).

Stemmer Imaging AG (2020). *Cameras*. URL: https://www.stemmer-imaging.com/en-at/knowledge-base/cameras/?choose-site=active (visited on 01/03/2020) (cit. on pp. 100, 101).

Teja, Krishna (2015). *3D Holographic Projection Technology*. URL: https://www.slideshare.net/krishna27694/holography-47756960 (visited on 08/19/2019) (cit. on p. 16).

TSI Incorporated (2007). *Model 3775 Condensation Particle Counter - Operation and Service Manual*. Tech. rep. April. Shoreview, USA: TSI Incorporated, p. 133 (cit. on pp. 6, 117, 131).

Verrier, Nicolas and Corinne Fournier (2015). "Digital holography super-resolution for accurate three-dimensional reconstruction of particle holograms." In: *Optics Letters* 40.2, p. 217. ISSN: 0146-9592. DOI: 10.1364/OL.40.000217. URL: http://ol.osa.org/abstract.cfm?URI=ol-40-2-217 (cit. on p. 78).

Vikram, C S (2005). *Particle Field Holography*. Cambridge Studies in Modern Optics. Cambridge University Press. ISBN: 9780521018302. URL: https://books.google.at/books?id=%7B%5C_%7DWkeDc%7B%5C_%7DR1bIC (cit. on pp. 15, 22, 39, 40, 49).

Wieland, M. (2015). "Holografie : Versuchsanleitung." Hamburg. URL: http://www3.physnet.uni-hamburg.de/ex/html/fprakt/af/holo/anleitung%7B%5C_%7Dholo.pdf (cit. on p. 22).

Willink, R. (2010). "On dead-time corrections for estimating rates." In: *Measurement Science and Technology* 21.1. ISSN: 13616501. DOI: 10.1088/0957-0233/21/1/015101 (cit. on p. 85).

Yu, Xiao et al. (2014). "Review of digital holographic microscopy for three-dimensional profiling and tracking." In: *Optical Engineering* 53.11, p. 112306. ISSN: 0091-3286. DOI: 10.1117/1.OE.53.11.112306. URL: http://opticalengineering.spiedigitallibrary.org/article.aspx?doi=10.1117/1.OE.53.11.112306 (cit. on p. 65).